Integrated Multiple Device CMOS-MEMS IMU Systems and

RF MEMS Applications

Hao Luo

**A dissertation submitted to the graduate school
in partial fulfillment of the requirements of the degree of
Doctor of Philosophy
in
Electrical and Computer Engineering**

**Carnegie Mellon University
Pittsburgh, Pennsylvania 15213**

Committee:
Professor L. Richard Carley (advisor)
Professor Gary K. Fedder (co-advisor)
Dr. Tamal Mukherjiee
Dr. Wilhelm Frey (Robert Bosch Corp.)

December 17, 2002

Report Documentation Page	*Form Approved* *OMB No. 0704-0188*

1. REPORT DATE **17 DEC 2002**	2. REPORT TYPE	3. DATES COVERED **00-00-2002 to 00-00-2002**

4. TITLE AND SUBTITLE **Integrated Multiple Device CMOS-MEMS IMU Systems and RF MEMS Applications**	5a. CONTRACT NUMBER
	5b. GRANT NUMBER
	5c. PROGRAM ELEMENT NUMBER
6. AUTHOR(S)	5d. PROJECT NUMBER
	5e. TASK NUMBER
	5f. WORK UNIT NUMBER

7. PERFORMING ORGANIZATION NAME(S) AND ADDRESS(ES) **Carnegie Mellon University,Department of Electrical and Computer Engineering,Pittsburgh,PA,15213-3890**	8. PERFORMING ORGANIZATION REPORT NUMBER

9. SPONSORING/MONITORING AGENCY NAME(S) AND ADDRESS(ES)	10. SPONSOR/MONITOR'S ACRONYM(S)
	11. SPONSOR/MONITOR'S REPORT NUMBER(S)

12. DISTRIBUTION/AVAILABILITY STATEMENT
Approved for public release; distribution unlimited

13. SUPPLEMENTARY NOTES

14. ABSTRACT
see report

15. SUBJECT TERMS

16. SECURITY CLASSIFICATION OF:			17. LIMITATION OF ABSTRACT	18. NUMBER OF PAGES	19a. NAME OF RESPONSIBLE PERSON
a. REPORT **unclassified**	b. ABSTRACT **unclassified**	c. THIS PAGE **unclassified**	**Same as Report (SAR)**	**187**	

Standard Form 298 (Rev. 8-98)
Prescribed by ANSI Std Z39-18

To my parents
To my wife, Jing

Table of Contents

Abstract

This dissertation describes design, fabrication and test of multiple micro-electro-mechanical system (MEMS) inertial measurement unit (IMU) systems and RF MEMS applications. The multiple degree-of-freedom (DoF) sensing systems have advantages from integration, such as low cost and capabilities for cross device compensation. This work focuses on the CMOS-MEMS thin film lateral accelerometer and vertical gyroscope design and functional test. Structures fabricated by the post CMOS-MEMS surface micromaching process have mass smaller than 10^{-6} g. The mass displacement resulted from external acceleration is in the angstrom to nanometer range. Such small mass and displacement bring challenges to detect the extremely small signals, which are under 1mV/G and only a fraction of femtofarad change for the sensing capacitance. The sensing techniques and system integration issues are addressed. Non-idealities such as cross-axis coupling and acceleration interference are compensated with integration at the system level.

Applications using Q enhanced inductors by MEMS technology are also presented in this thesis. A voltage-controlled-oscillator (VCO) fabricated in a 0.18 μm copper CMOS process has a 2.2GHz oscillation frequency and phase noise of -60dBc/Hz at 100kHz offset. Another VCO fabricated in silicon-germanium (SiGe) BiCMOS process has a 5.1GHz oscillation frequency and phase noise of -73dBc/Hz at 100kHz offset.

Acknowledgments

My past five years at Carnegie Mellon University has been filled with many great memories which I will cherish for the rest of my life. All these experiences would be impossible had Prof. L. Richard Carley not offered me the opportunity to study under his guidance. Throughout the years his profound knowledge in many different fields has been my constant source of inspiration. Without his high level guidance and the free research environment created by him, my work would be impossible.

I would like to thank my co-advisor Prof. Gary K. Fedder, who has always been patient and sourceful in discussion in research. His help in many detail fields helps me overcome the difficulties in my work. His insights in the research created strong images in my mind that I will never forget. I still remember how he wrote the long equations on the white board when we discussed research in his office.

I would also like to thank Prof. Tamal Mukherjee for discussions in many areas, not only in research but also in how to adapt to graduate research life quickly when I just arrived CMU. His knowledge in CAD area helped me in solving many technical problems.

I would like to thank Dr. Wilhelm Frey from Robert Bosch Corporation for discussions which broaden my view in the research. His kindness and suggestions really helped me very much in my thesis work.

I would also like to thank Dr. Xu Zhu and Santhman Suresh for help in performing the device release processes. All the chip release process used in my research is based on their work. Without their help, my research would be impossible.

Thanks also go to my colleagues, Huikai Xie, Hasnain Lakdawala and Wu Jiangfeng. All the discussions and advice we've had together really helped me think better in many occasions.

I would like to thank my family in China for being always patient when I felt alone and called them to tell them the difficulties I met in my research. And finally I would like to thank my wife, and also my colleague, Qi Jing for being always two hundred percent behind me and for being always my source of inspiration for success.

Chapter 1

Introduction

Over the past decade, micro-electro-mechanical-system (MEMS) technology has been established as a solution for inertial sensing problems[1][2][3]. The primary efforts are to lower the cost and to improve the performance of miniaturized systems. The advantages of low cost, low-power, small size and batch fabrication ability makes MEMS-based inertial sensors suitable for applications in automotive, consumer electronic, computer system, and navigation markets. Using IC technology to fabricate devices in large volume can dramatically decrease the cost for each device. However, the device miniaturization has brought many challenges, such as difficulty in detecting extremely small signals, resulting in poor device performance, relative to macro-scale counterparts. Current MEMS inertial sensors can be classified in two main categories: bulk micro-machined devices and thin film micromachined devices. The bulk devices normally have better performance but are much more expensive than thin film devices and are difficult to be integrated. In some cases, multiple axis sensing requires a multi-sensor system, e.g., 6 degree-of-freedom sensing (Figure 1-1). Thus lowering the cost is primarily concerned with low-cost fabrication process and integration. Thin film devices normally have much smaller proof mass and noise perfor-
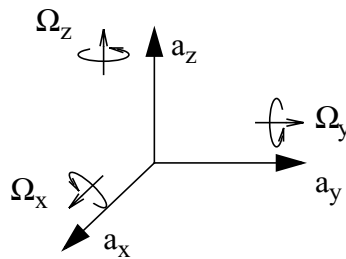
Figure 1-1. Three axis coordinates reference and 6 DoF sensing
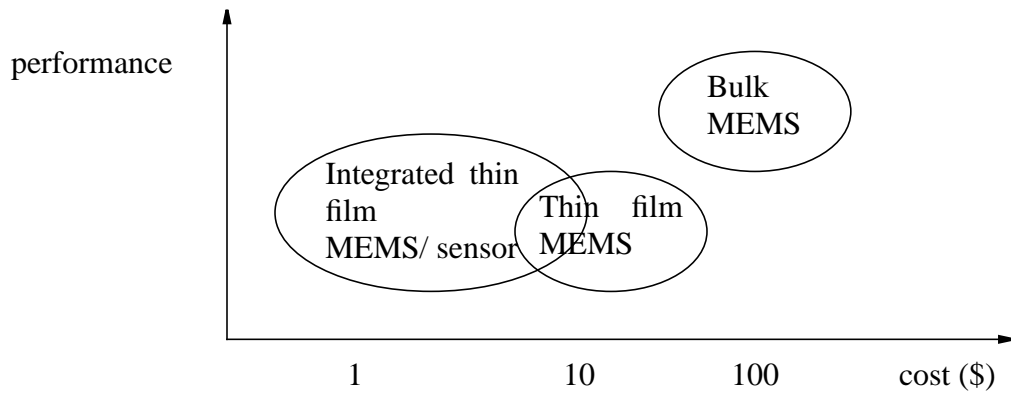
Figure 1-2. Cost and performance of MEMS inertial sensor device.

mance are limited. But it is possible to use IC compatible processes to integrate multiple sensors on a single chip. The integration can greatly decrease the cost of per-axis sensing task (Figure 1-2) and may overcome some drawbacks of single device system.

This chapter begins with a brief summary of inertial sensing systems which have been done prior to the current efforts, and ends with current technology used in Carnegie Mellon University. The subsequent chapters will discuss the approaches for integration in details.

1. 1 History of inertial sensing and MEMS as part of it

Inertial sensing has long been desired in military applications for navigation. Inertial systems were used as early as 1900's as gyrocompass in gyroscopic aircraft instruments, stable platform for gun laying, radar antennas, and flight control [4]. In the 1930's, German engineers developed a rudimentary inertial system for a series rocket programs [4]. The first rocket with inertial guidance, A-2, was launched in 1934. Its successor, the A-4 (later called V-2) was the first rocket ever launched in World War II. In those guidance systems, three gyros were mounted on a three-axes stabilized platform, which weighed 100 pounds.
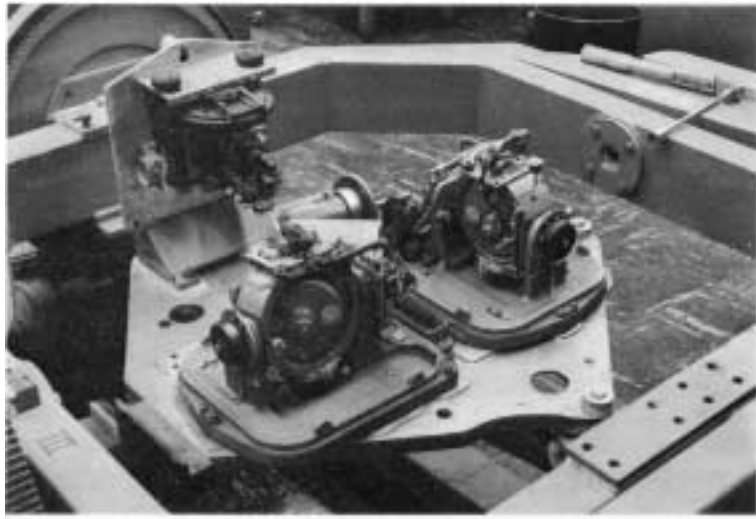
Figure 1-3. Early inertial guidance system made by German engineers. A similar one used on V-2 was 20 inches in diameter and weighed 100 pounds [4].

The modern inertial navigation system (INS) was first demonstrated in 1949 by Charles Stark Draper, and since then has been the preferred method of navigation on military and commercial aircraft whose mission profile excludes dependency on external references or signal sources [4]. During the 1970s, the gimbaled INS gave way to the strap-down INS with the advent of the ring laser gyro and a sufficiently powerful avionics computer that could perform the numerically intensive high rate strap-down navigation computations [4].

Inertial sensing started being widely used in commercial applications in the late 60's. Auto safety requires automobiles to be equipped with air bags to protect passengers during crash. The operation of the air bag relies on the on-vehicle acceleration sensor. In 1971, the Ford company built an experimental air bag fleet [5]. Later, more and more inertial sensors were needed for all kinds of applications such as easy vehicle control, vibration reduction and motion monitoring [6]. Many of those commercial applications require small and low-cost inertial sensors that can be fabricated in large quantities. And this motivation lead to the micromachined sensor playing an

important role in the market. This thesis mainly focuses on the thin film devices due to their ability for integration.

In the early 80's, researchers at UC Berkeley first fabricated polysilicon microstructures [7]~[9]. The success of the surface-micromachined electrostatic micromotor in the late 80's [10] stimulated the industry and government funding for research in the MEMS. Many current micro-mechanical fabrication processes and devices have evolved significantly from their primitive beginnings. In 1993, Analog Device introduced the first integrated surface MEMS based acceler-ometer, the ADXL05 to the market [11]. Many other researchers have reported on a variety of accelerometers and gyroscopes, both single axis and multiple degree-of-freedom (DoF) [12]~[17] (Figure 1-4). A german company Robert Bosch developed two types of MEMS gyroscope for automobile navigation (MM1) and roll-over detection (MM2) [18]. In the year of 2002, Analog Device introduced the world first integrated MEMS gyroscope ADXRS150 to the market [19].

Currently MEMS inertial sensors are widely desired for insertion in auto and consumer elec-tronics. They are used in many applications such as auto safety and stability control, vibration control, computer input interface and virtual reality [20]. Different kinds of applications need dif-ferent kinds of specifications. Typical specifications of accelerometers are given in Figure 1-5.

For those applications which require multi-axis sensing abilities, integration is the most effi-cient way to lower the cost, especially when the packaging accounts for 75% of the sale price of the device [21].

1. 2 Current MEMS technologies

Current MEMS technologies include two main trends, bulk and surface (thin film or thick film) micromachining. The structural material for both technologies can be either metal or silicon based material. Bulk micromachined devices normally have better performance, such as lower

(a)   (b)

(c)

(d)
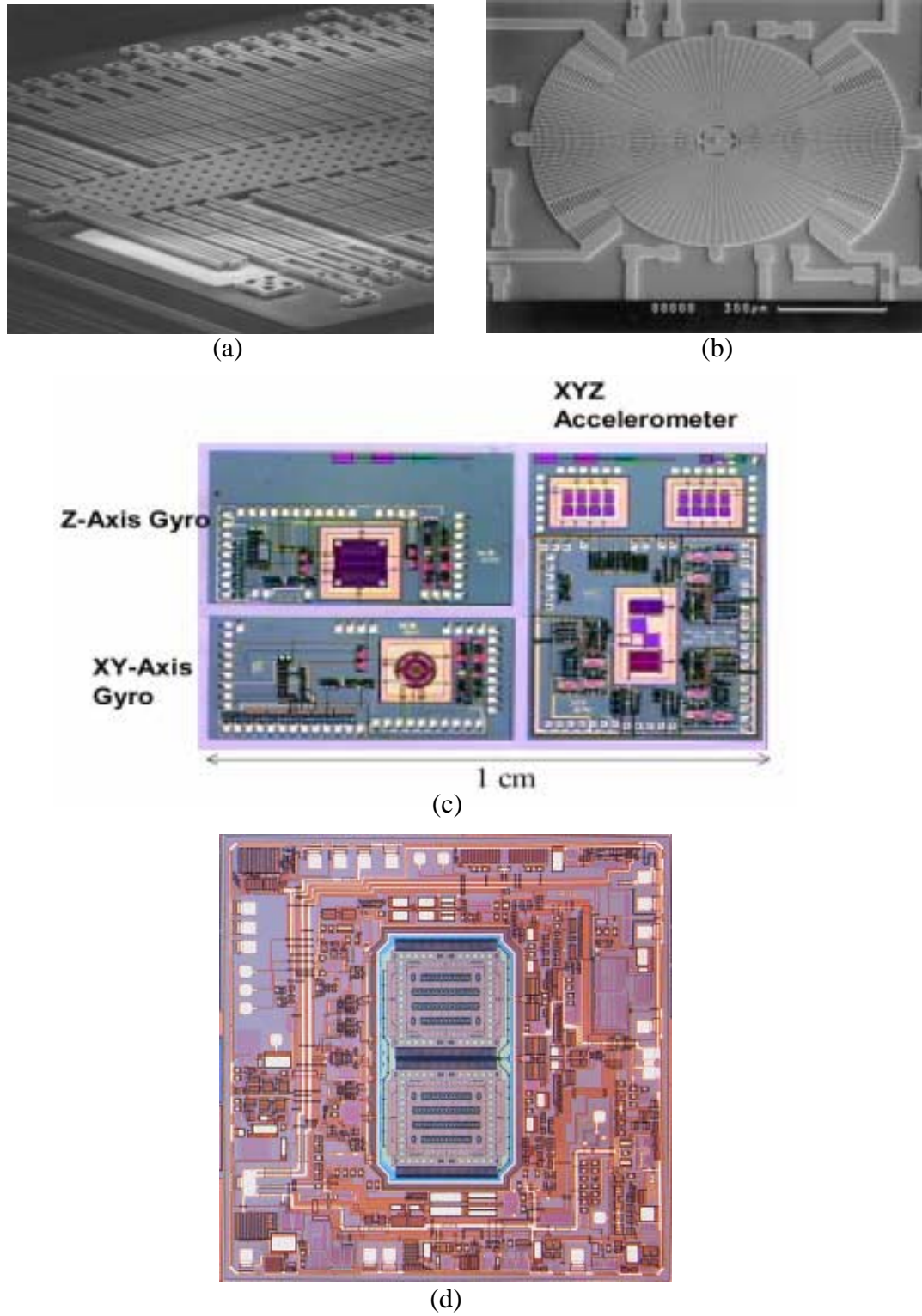
Figure 1-4. (a) SEM of ADXL250 accelerometer [5]. (b) Bosch gyroscope (MM2) [18] (c) 6 DoF IMU chip fabricated in Sandia National Laboratory [18]. (d) Analog Device gyroscope ADXRS150 [19].
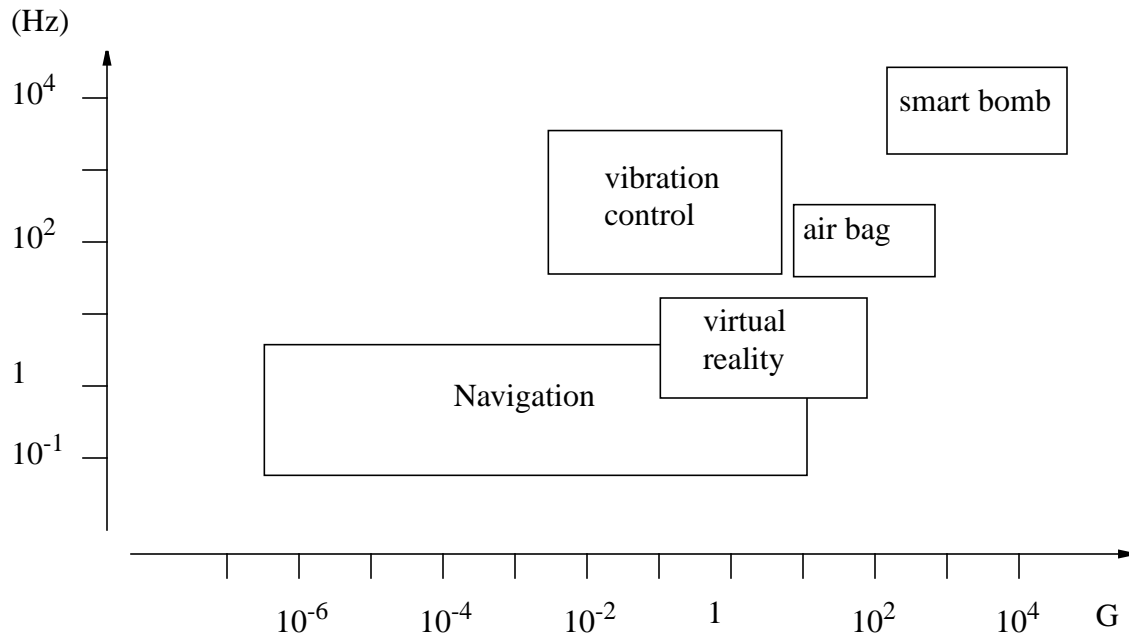
Figure 1-5. Typical application and its specifications of inertial measurement unit [6].

noise, but they are more expensive than the surface micromachined devices and difficult to integrate. Thin film devices are quite competitive for those applications which do not require extremely high resolution, such as airbag accelerometers, tilt sensors, computer input interfaces, and virtual reality tracking systems.

Polysilicon thin film is the most commonly used MEMS structural material for its easy availability and low cost, such as used in MUMPS [22]. Since the polysilicon structure is a uniform conductor, the lack of electrical isolation within a structure constrains design of complicated structures which require multiple electrical signals.

Another drawback of polysilicon process is the difficulty for integration. Because the polysilicon requires high temperature for deposition and annealing, it can not be fabricated after the circuit is made on the same chip. Normally it has to be made on a separate chip, e.g. MUMPS, to build a complete system. Recently, metal induced crystallization (MIC) of amorphous silicon (a-

Si) and amorphous Germanium (a-Ge) have been studied intensively [23][24][25]. The poly-SiGe structural layer is deposited at a lower temperature ($< 400°C$) and a higher rate, and has lower strain and strain gradient than polysilicon. High-temperature annealing is therefore not necessary [26]. But the deposition temperature and doping concentration have a significant influence on the structure internal stress. This process might has the potential to be integrated with circuits.

CMOS-MEMS technology has the capability to integrate sensors and circuits in a single chip. In this technology the micromaching process is combined with the conventional CMOS fabrication steps. The additional MEMS process can be made before (pre-CMOS), after (post-CMOS) or in-between (intermediate-CMOS) the regular CMOS steps [27]. In the pre-CMOS approach, the micromachining structures are formed before the regular CMOS process, e.g., the iMEMS used in Sandia National Laboratory [28]. In the intermediate-CMOS process, the CMOS process is interrupted for additional micromaching steps, e.g., Infineon's pressure sensor [29] and early Analog Devices's accelerometers [30]. In the post-CMOS approach, structures can be made either on top of the finished CMOS chip [31] or using CMOS layers with combined surface or bulk micromachining techniques [27][32]~[34].

Thin film post-CMOS micromachining has many attractive features for the fabrication of integrated inertial sensors [32]. The compatibility of the micromachining process with standard CMOS has the advantages of low cost and compact integration of the micromechanical structures and circuits. The multiple layer routing ability enables design of very complicate structures which are not possible in a uniform conductor structure. The close coupling between the sensing element and signal processing circuits reduces the parasitic capacitance, and noise pick-up. Usually CMOS surface microstructures fit in a small die area with circuits placed close (30~40 μm) to the structures. An array of sensing elements can be integrated to improve the system performance.

1. 3 CMU post-CMOS micromachining process

The high-aspect-ratio post-CMOS micromachining technology [32][35] is utilized to make all the systems described in this dissertation. Designs are fabricated in the Agilent three-metal 0.5 μm n-well CMOS process, the AMS three-metal 0.6 μm n-well CMOS process and the UMC 0.18 μm six layer copper CMOS process. After the foundry fabrication, two dry etch steps, shown in Figure 1-6, are used to define and release the structure. Figure 1-6(a) shows the cross section of the chip after regular CMOS fabrication. In the first step of post processing (Figure 1-6(b)), dielectric layers are removed by an anisotropic CHF_3/O_2 reactive-ion etch (RIE) with the top metal layer acting as an etch resistant mask. After the sidewall of the microstructure is precisely defined, an isotropic SF_6/O_2 RIE is performed to etch away the silicon under the structure to release the composite structure (Figure 1-6(c)). Layout in the metal layers is designed to form beams, plates, and electrostatic comb fingers. Since those metal layers are stable during the two-step release process, they define the geometry of mechanical structures. They keep the structure dimensions stable against some etch variation. Material property values for the composite structures include a density of 2300 kg/m^3 and a Young's modulus of 62 GPa [36].

The availability of CMOS and simple dry-etch micromachining provides a low-cost way to integrate MEMS with electronics. Electrically isolated multi-layer conductors can be routed in the composite structures, enabling more design options (compared to homogeneous conductor structures). For example, electrically decoupled sensing and actuating comb fingers may be built on the same structure, and full-bridge capacitive differential and common-centroid comb-finger designs can be readily implemented.

The undercut of silicon in the release step (Figure 1-6(c)) requires the placement of sensing circuits to at least 15 μm away from the microstructures. Compared to most commercialized poly-

metal-3
overglass
gate
polysilicon
metal-2
metal-1
0.5μm
n-well
CMOS
silicon
substrate

(a)

metal-3
mask

(b)

composite
structures

exposed
silicon

(c)

meander-beam
springs
etched pit
center plate
electrostatic
comb drives
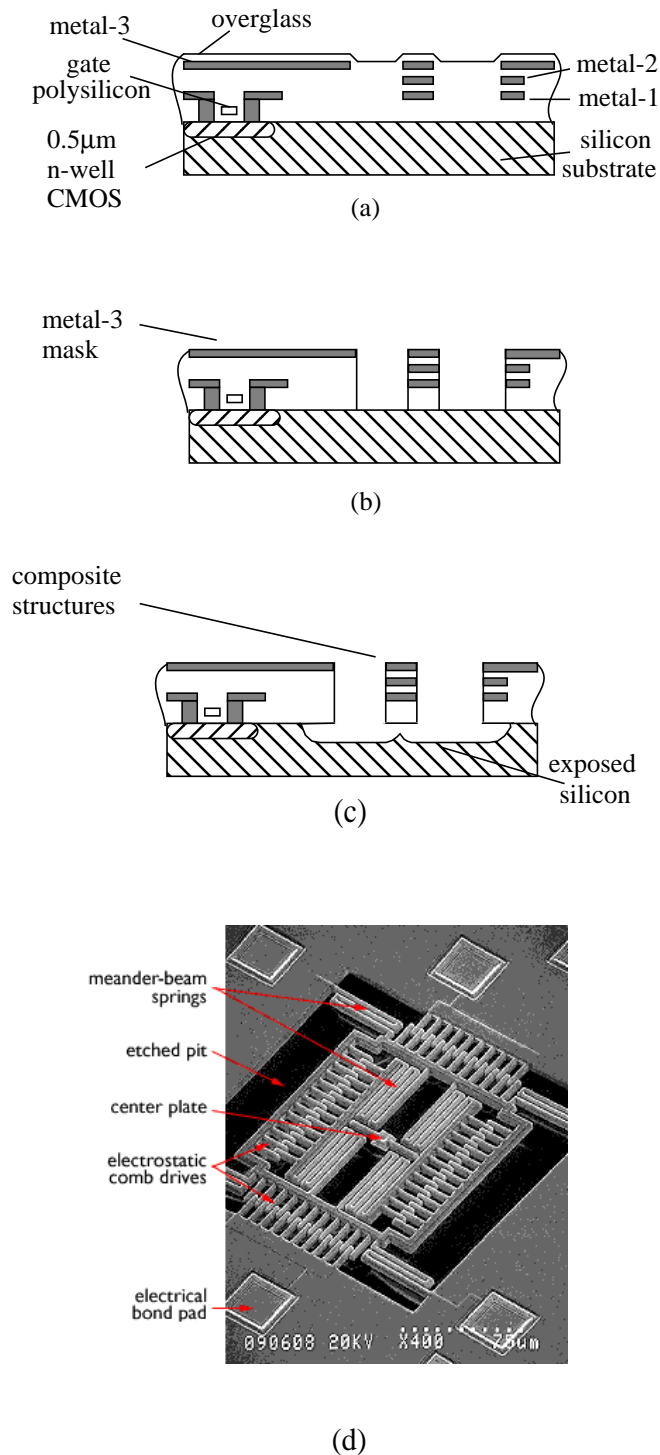electrical
bond pad

090608 20KV X400   25μm

(d)

Figure 1-6. CMOS-MEMS process. (a) CMOS chip after fabrication. (b) Anisotropic RIE removes dielectric. (c) Isotropic RIE undercuts silicon substrate. (d) An example of a released device (x-y stage).
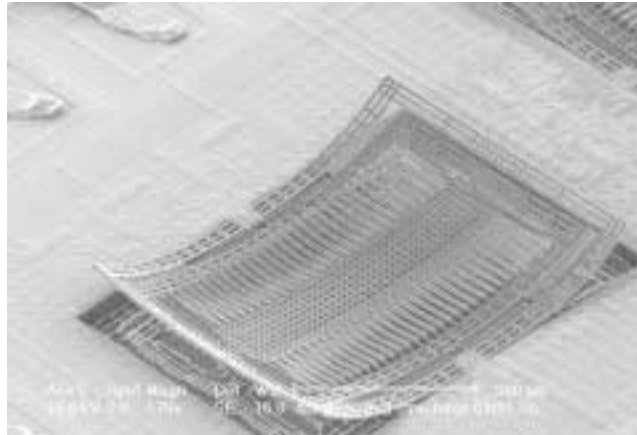
Figure 1-7. CMOS-MEMS structure curl.

silicon micromachining technologies, the MEMS to electronics interconnect in CMOS-MEMS is shorter, and has less parasitic capacitance. Such parasitics on high-impedance wiring can be made small relative to input capacitance of interface circuits, so the transducer sensitivity is increased and signal to noise ration (SNR) is improved.

The main disadvantage of the CMOS-MEMS process is the out-of-plane and in-plane curling of the composite structures. The curling is caused by the stress gradient and different temperature coefficient of expansion (TCE) of the materials in the laminated structure. After the release the stress gradient inside will force the structure to curl up (Figure 1-7). This problem can be mitigated by several ways such as stress optimized design, curl-matching technique [37] and thermal control methods [38].

1. 4 RF CMOS MEMS application

CMOS-MEMS technology can not only be used for IMU applications, it can also be exploited in other areas such as RF applications. One of the difficulties in RF design is that high quality inductors are not available in conventional IC processes. In this work, the post CMOS-
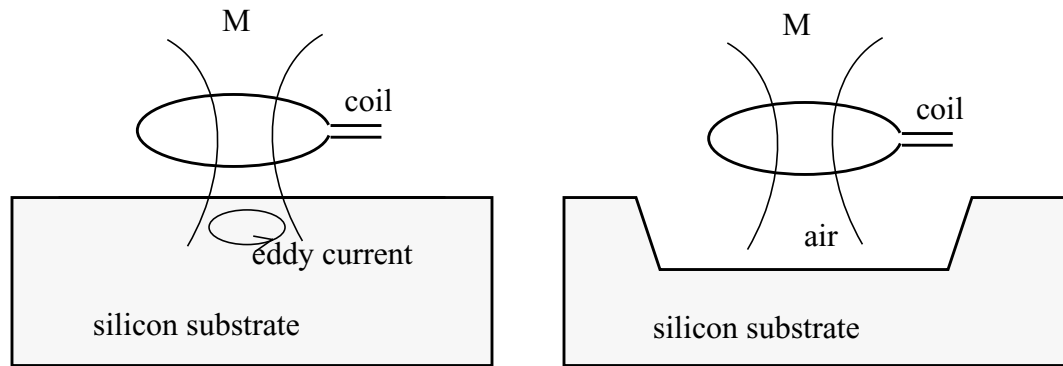
Figure 1-8. Decrease eddy current by removing underneath silicon.

MEMS process is utilized to undercut silicon under the inductor coil to increase the quality factor (Q) at GHz frequencies. The substrate (Si) in conventional IC processes is conductive. The eddy current loss can be decreased by removing the silicon underneath the coil, and hence the Q can be increased (Figure 1-8).

1. 5 Dissertation organization

This dissertation describes the design methodology of integrated multiple device inertial sensor systems. It shows the integration ability and the benefit from this integration by using the post-CMOS MEMS process.

Chapter 2 & Chapter 3 describe the design of single accelerometer and gyroscope. Chapter 4 describes the circuitry used for the capacitive sensing system. Chapter 5 introduces some system level issues for integration. Chapter 6 gives the test results of the inertial measurement systems.

In the last Chapter 7, two types of RF VCOs using MEMS enhanced inductors are discussed and the test results are presented.

Chapter 2

Acceleration sensor design

This chapter talks about the design and operation of post CMOS micromachined accelerometer. An accelerometer fabricated in HP (now Agilent) 0.5 μm 3 metal layer CMOS process will be used as an example. The mechanical design and analysis will be discussed.

2. 1 Mechanical structure design

The core of an accelerometer is a proof-mass with suspending structure. Under an applied acceleration, the proof-mass moves with respect to the substrate. The comb fingers attached to the proof-mass transfer the position change into capacitive variation to detect acceleration.
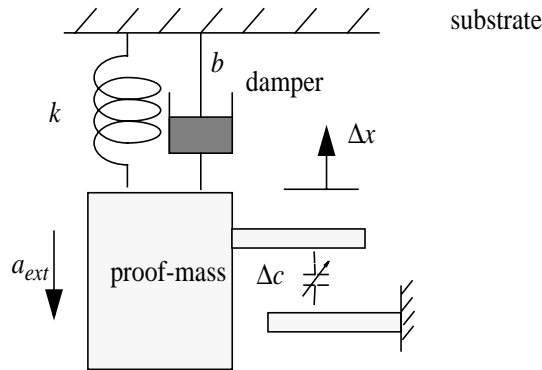
Figure 2-1. Schematic of proof-mass, spring, damper and variable capacitor used for acceleration sensing

Since the capacitance sensing is utilized, the capacitor structure need to be investigated. In this thesis, all the lateral sensing capacitors are composed of side-wall capacitors between the comb fingers (Figure 2-2). The capacitance between comb fingers is simulated using Maxwell ^{TM}. To see whether the capacitance is sensitive to the fringing field, two kinds of comb fingers were

Figure 2-2. Cross section of two comb fingers. Multiple layers in each finger are shorted together by vias.

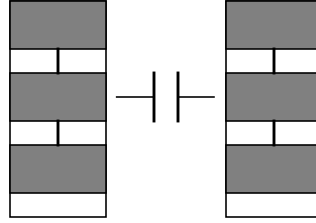simulated (Figure 2-3). The first one is with solid metal finger, and the second one is with multi-metal-layer finger. Both of them have the same size (4 μm by 5 μm with 1.5 μm gap, cross section). As shown in the Figure 2-3, the equipotential contours between the two comb fingers are very similar to each other, which means the fringing field is not very sensitive to the finger structure in these two cases. The capacitance between two comb fingers is 3.389×10^{-11} F/m for solid

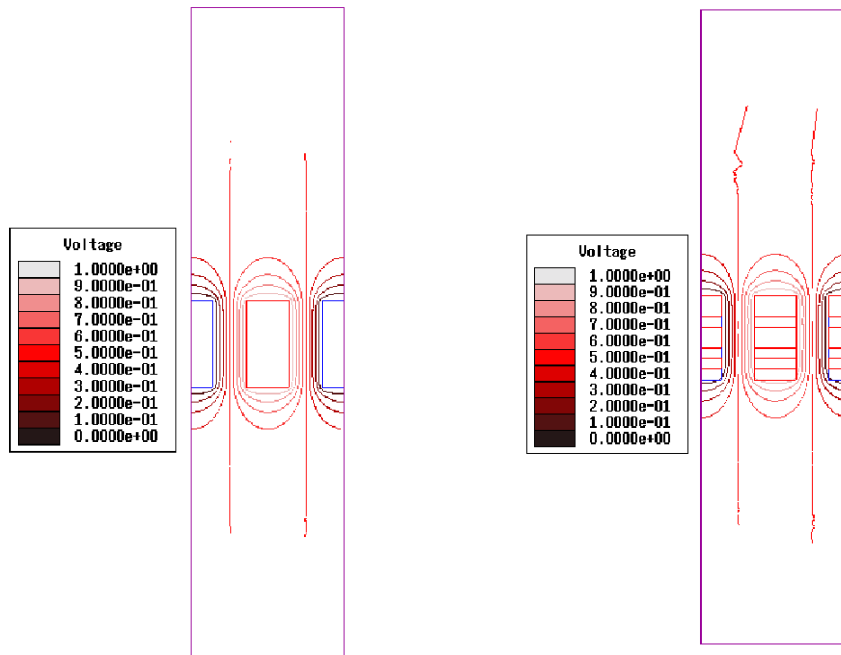Figure 2-3. Equipotential contour distribution between two comb fingers (with 1V bias).

Hao Luo

metal fingers and 3.2238×10^{-11} F/m for the multi-metal-layer fingers. Both values are close to the ideal parallel plate capacitor model with solid metal, which is 2.95×10^{-11} F/m. Thus, in the later design, parallel plate capacitor model will be used to estimate the total sensing capacitance.

The accelerometer is composed of a proof-mass, suspending serpentine springs and comb fingers. By exploiting the multi-layer routing technique, this accelerometer has a fully differential topology [37]. In the layout, each half-capacitive bridge is split into two parts and located at two cross-axis corners Figure 2-4. This differential layout topology cancels common-mode input interference such as substrate coupling, power supply coupling and cross-axis excitation. Since there are multiple sensors and circuitry integrated on the same substrate, coupling through the substrate is preferred to be minimized when high impedance sensing (capacitive sensing) is used. All the signals on the moving part are routed through the multi-layer suspending springs and all the cross links are placed in the proof mass layers. Compared to a polysilicon accelerometer, multi-layer microstructures give more freedom in MEMS design such as creating differential topologies and nested electrostatic driving and sensing [39].

A released accelerometer is shown in Figure 2-4. The total device size is 350 μm by 500 μm and the front-end circuitry takes an area of 220 μm by 200 μm (not shown), which is covered by the top metal layer for protection during the micromachining process steps. The accelerometer has a proof-mass of 160 μm by 350 μm with multiple 6 μm by 6 μm releasing holes (lattice width 3 μm). The 40 sensing fingers and 12 actuating comb fingers are the same size of 55 μm long and 3.9 μm wide. Each serpentine spring has two turns and the beam in each turn is 117 μm long and 2.1 μm wide. The whole released structure is uniformly ~5 μm thick.

The composite structure experiences larger vertical stress gradients than its polysilicon counterpart. Vertical residual stress gradients in the CMOS structures can result in a radius of curvature
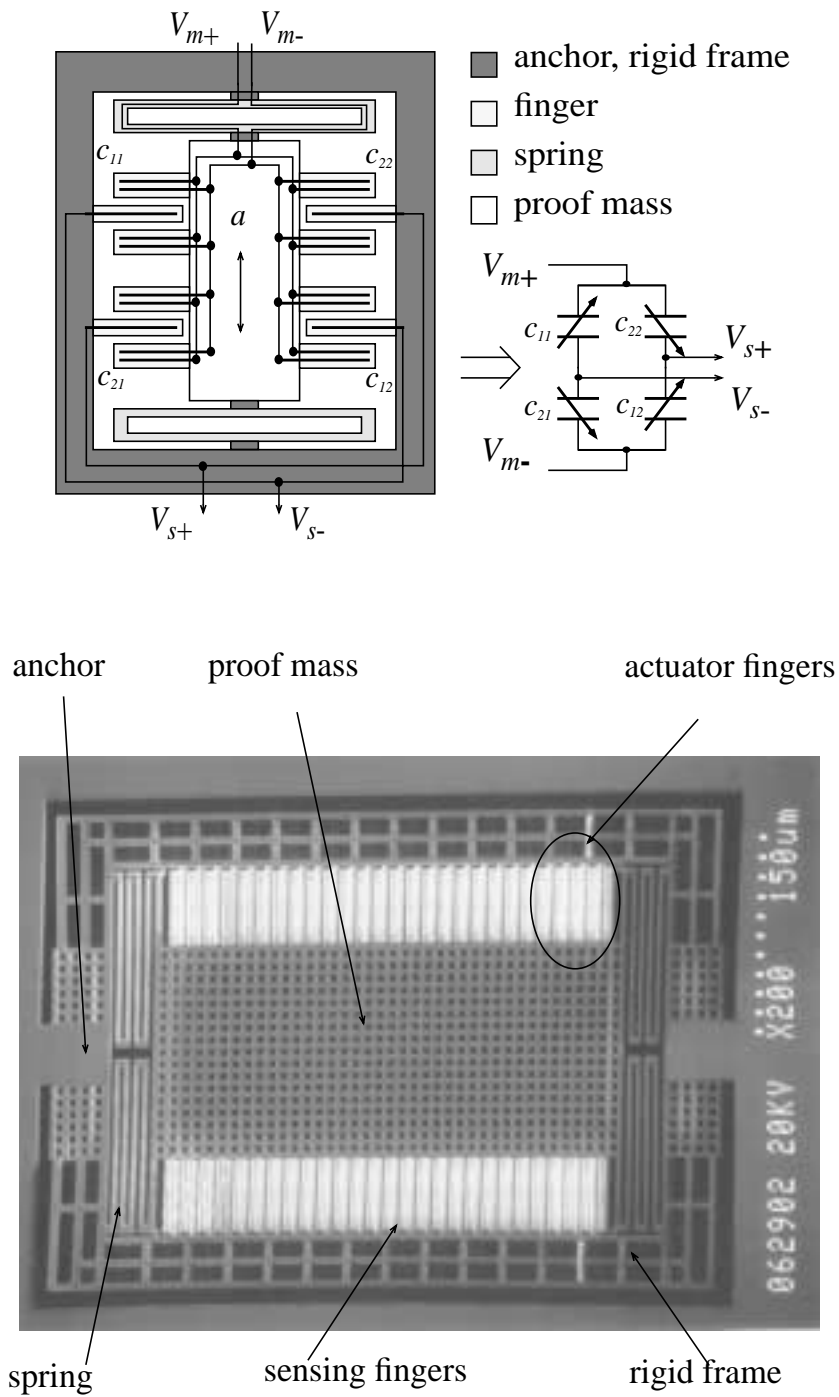
Figure 2-4. (a) Schematic of accelerometer and its equivalent model. (b) SEM of a released accelerometer

of 1 mm to 5 mm [40]. Out-of-plane curling can significantly reduce the comb finger sidewall capacitance which is critical to capacitive sensing. To solve this problem, fingers on the stator side are attached to a rigid frame (Figure 2-1, b) instead of the substrate. The rigid frame is anchored along a common axis with the proof mass, and is subjected to the same stress gradient as the inner structure. Thus, first-order curl matching can be achieved. To get optimal sidewall alignment, a local matching technique has been developed. The middle part of the rigid frame has the same density of holes in its structure as the proof mass. The outer part of the rigid frame is composed of beams that have the same cross section as the fingers. This design eliminates the pattern-sensitive mismatch between the inner and outer structures. Out-of-plane curl measured with a Wyco NT3300 optical profilometer is shown in Figure 2-5. The maximum out-of-plane curl is 6 μm while the mismatch between the rotor and stator fingers is reduced to 0.3 μm (Figure 2-5 d).

The proof mass is suspended by serpentine springs shown in Figure 2-6. The sense-axis spring constant is given by [48]

$$k = \frac{48EI_{zl}[5(\tilde{c} + l) - l)]}{4l^2[5(3\tilde{c}^2 + 4\tilde{c}l + l^2) + 3\tilde{c}^2 - l^2]} \tag{E 2-1}$$

$$I_{zl} = t\,W_l^{\,3}/12 \tag{E 2-2}$$

$$\tilde{c} = dI_{zl}/I_{zd} = d\,W_l^{\,3}/W_d^{\,3} \tag{E 2-3}$$

where t is the beam total thickness of 5 μm, l is the long beam length of 117 μm, d is the short beam length of 5.1 μm, W_l (2.1 μm) and W_d (5.1 μm) is the long beam and short beam width, respectively, and E is the composite structure effective Young's modulus of 62 GPa, which is extracted from measurements of cantilever test structures [40]. The spring constant is 1.77 N/m. The only differences in the composite beam mechanical design, compared to polysilicon or sili-
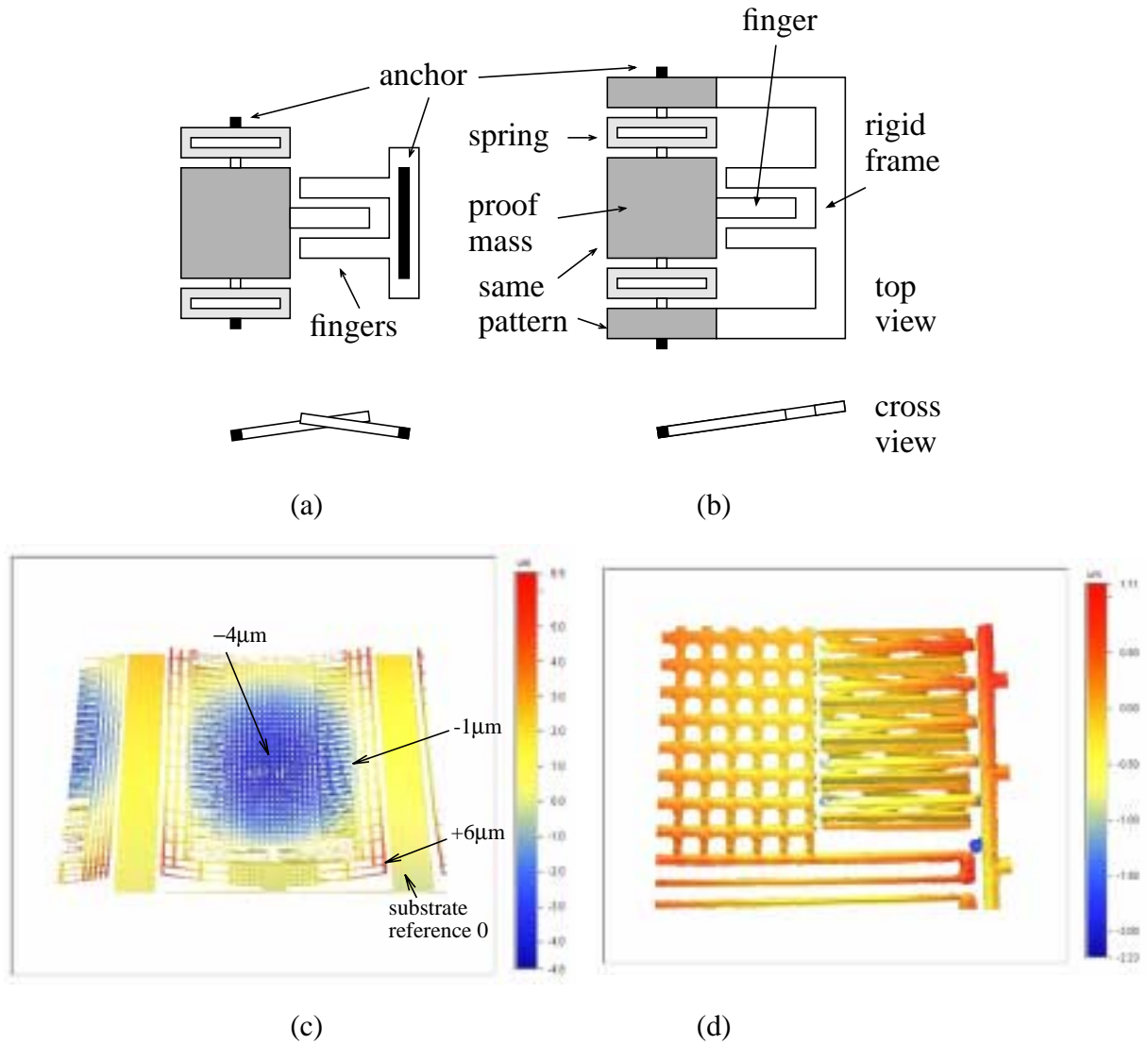
Figure 2-5. Schematic of curl matching and measurement results. (a) Without curl matching. (b) With curl matching. (c) and (d) Optical profilometer measurement showing out-of-plane curl and the curl matching.

con beam design, are the values of effective mass density, effective Young's modulus and cross section geometry.
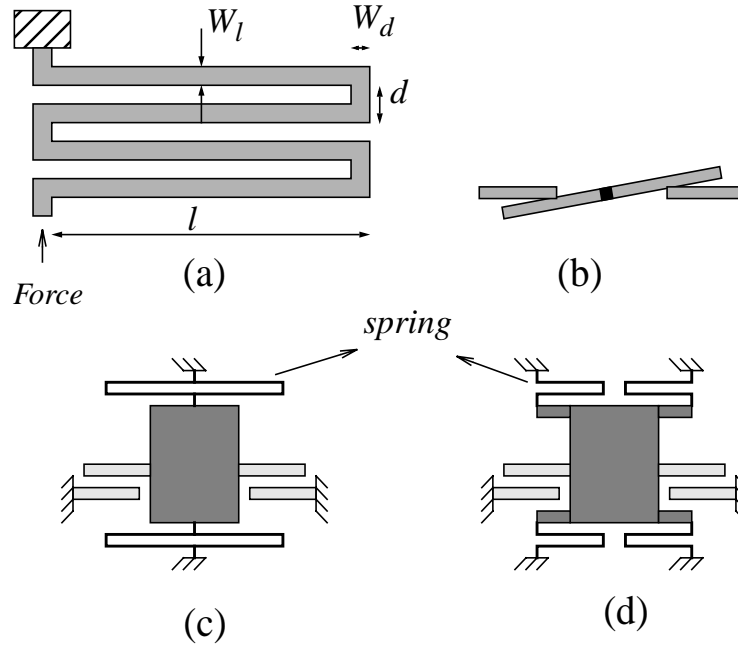
Figure 2-6. Spring design. (a) Serpentine spring. (b) Structure tilt. (c) Center attachment.
(d) Corner attachment.

Springs can be attached to the proof mass at its mid-point (Figure 2-6 (c)) or at the four corners (Figure 2-6 (d)). The mid-point attachment has good linear motion in plane, but the curling makes it sensitive to tilt with respect to the center line (Figure 2-6 (b)). The corner attachment design avoids the problem with tilting and provides better curl matching.

The accelerometer can be simplified as the lumped parameter model shown in Figure 2-1. The differential equation of displacement x as a function of input acceleration a is given by (E 2-4)

$$m\frac{d^2x}{dt^2} + b\frac{dx}{dt} + kx = ma_{ext} \qquad \text{(E 2-4)}$$

Taking the Laplace transformation gives the system transfer function as

$$H(s) = \frac{X(s)}{A(s)} = \frac{1}{s^2 + s\frac{b}{m} + \frac{k}{m}} = \frac{1}{s^2 + s\frac{\omega_r}{Q} + \omega_r^2} \qquad \text{(E 2-5)}$$

where ω_r is the resonant frequency, b is damping coefficient and Q is the quality factor ($Q = \omega_r m/b$). For most applications, the applied acceleration frequency is much less than ω_r, thus the mechanical sensitivity of the device is $1/\omega_r^2$.

By detecting the sidewall capacitance change between the comb fingers attached to the proof mass and anchor, lateral motion and therefore acceleration is measured. Shown as Figure 2-4, the three metal layers in each finger are connected together as one electrode. Forty differential sensing comb fingers have length of 55 µm and gap, $g = 1.5$ µm. Using the simple parallel-plate capacitor model, the capacitance between each pair of fingers is calculated to be about 1.6 fF. The total sensing capacitance, C_s is 64 fF.

Since the resonant frequency of the accelerometer is 8.9 kHz, the displacement sensitivity is only 3.1 nm/G, corresponding to 1.3×10^{-16} F/G change in the capacitance. This extremely small capacitance is challenging to measure, because the incremental capacitance change is much less than the parasitic capacitance C_p, (around 120 fF). To decrease the parasitic capacitance, the high-impedance node fingers are attached at stators instead of rotors to minimize the distance to the circuits. Modeling the sensing capacitor as a parallel-plate capacitor, the electrical signal sensitivity is

$$\frac{V_o}{a} = V_m \cdot \frac{2C_s}{2C_s + C_p} \cdot \frac{1}{g} \frac{1}{\omega_r^2} \qquad \text{(E 2-6)}$$

where V_m is the modulation voltage of 2 V, g is the gap of 1.5 µm and ω_r is the resonant frequency of $2\pi 8.9$ kHz. The calculated sensitivity is about 2.2 mV/G.
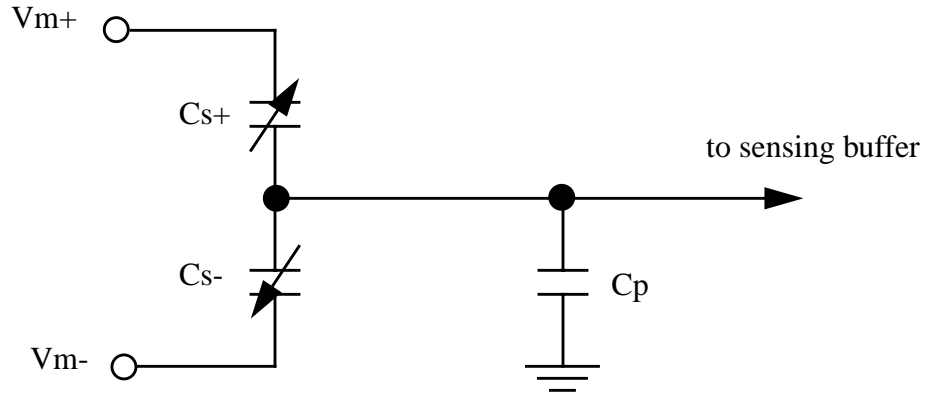
Hao Luo

Figure 2-7. Capacitor bridge interface

A potential limitation for the surface micromachined accelerometer is the Brownian noise associated with damping forces. Because the mass is so small, it will be agitated by the collision with air molecules. According to the Nyquist's relation [42] in thermal equilibrium, the spectral density of fluctuation force acting on the device is

$$\frac{F^2}{\Delta f} = 4k_B Tb \qquad \text{(E 2-7)}$$

where k_B is the Boltzman constant. The device experiences equivalent noise acceleration

$$\frac{a^2}{\Delta f} = \frac{4k_B Tb}{m^2} = \frac{4k_B T\omega_r}{mQ} \qquad \text{(E 2-8)}$$

For this accelerometer prototype, the model values are $m = 0.57$ μg, $\omega_r = 56$ krad/s, Q=24 (measured), giving an equivalent noise acceleration of approximately 6.9 μG/$\sqrt{Hz}$ at room temperature. The noise performance can be improved by increasing the mass, which is limited by the dimensions of the microstructure.
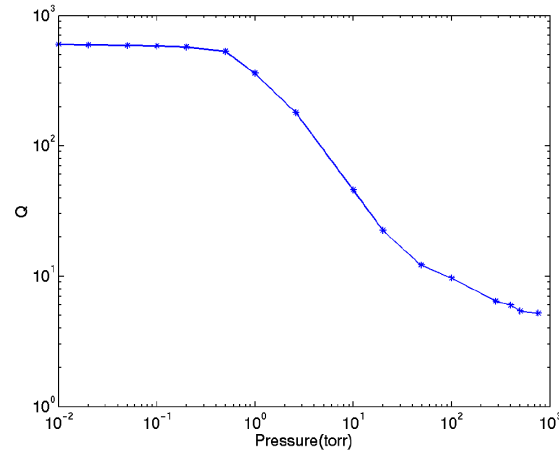
Figure 2-8. Quality factor vs. pressure

Decreasing pressure will significantly boost the quality factor. However the mechanical internal damping will limit this improvement. This damping is related to energy loss from material deformation and internal stress. Measured quality factor with pressure for a similar but smaller (400 μm by 330 μm) CMOS micromachined structure is shown in Figure 2-8. The quality factor is extracted from the peak in the electrostatically actuated mechanical frequency response as $Q=\omega_r/\Delta\omega$, where $\Delta\omega$ is the -3 dB bandwidth of the peak. The internal damping dominates at low pressure which causes the Q to saturate at around 600. The quality factor at low pressure is much less than that of polysilicon and silicon microstructures which have been reported Q of over 80000 [45].

In the resonant frequency test of the accelerometer, a driving voltage of 3 V_{dc} plus 3 V_{ac} was applied to the self-test actuator finger on the accelerometer and the motion was measured with the MIT Microvision™ system. The experimental goal is to verify the structure is fully released and can move freely without being hampered by sidewall polymer which is a by-product of the releas-

ing process. Figure 2-9 shows the measured displacement versus frequency. The measured reso-
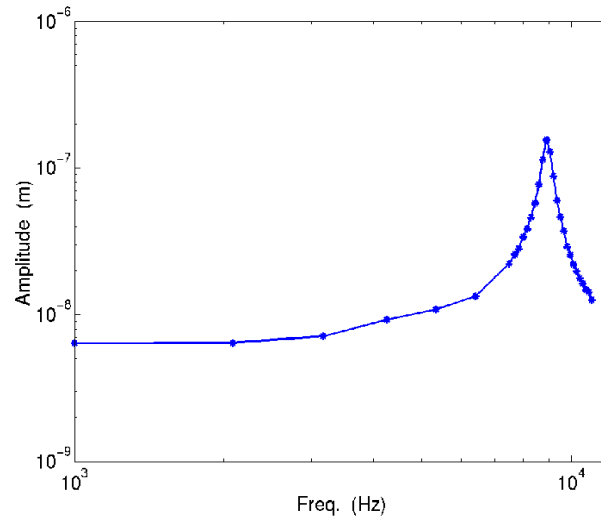
nant frequency is 2π8.9 kHz.

Figure 2-9. Accelerometer displacement vs. frequency during self-test.

The accelerometer only has the sensor and buffer integrated on chip. The rest of the signal

channel was implemented on a test board. In the dynamic test, the accelerometer test board was

excited by a 50 Hz 14 G (p-p) sinusoidal acceleration on a Brüel and Kjær vibration table. The

waveforms of the output from a reference accelerometer and the output from the CMOS-MEMS

accelerometer are compared in Figure 2-10. Figure 2-10 also shows the spectrum of the output

from the accelerometer when excited by an 100 mG acceleration at 80 Hz. The measured noise

floor was 1 mG/$\sqrt{Hz}$, which is much larger than predicted. Further experimental results show that

the electrical noise of the read-out circuits dominates the system noise performance (see Chapter

4&6).

Linearity of the accelerometer was measured by applying sinusoidal acceleration at 200 Hz.

The measured dynamic range of ±13 g was limited by the maximum output acceleration of the

test equipment. Even when the accelerometer experienced a large acceleration shock (> 30 G)
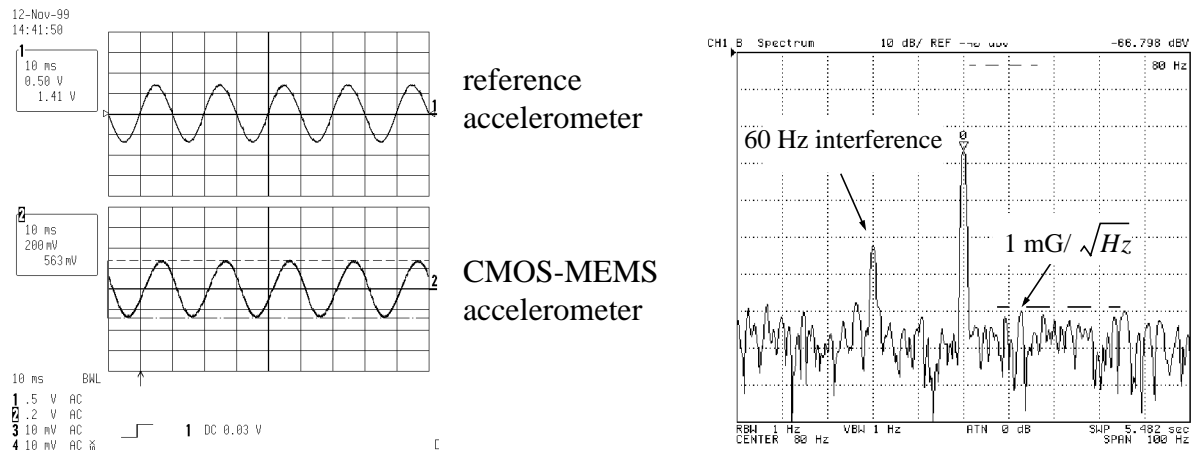
Figure 2-10. Accelerometer output waveform and spectrum (100 mG 80Hz input).

during a crash test, saturation has not been observed. In the cross-axis sensitivity test, the accelerometer showed a -40dB attenuation compared to the sensing axis sensitivity.

The accelerometer has been working for over three years and has experienced more than 200 acceleration shock events (> 30G) in demonstrations. No degradation in performance has been observed.

2. 2 Summary

This chapter uses an accelerometer fabricated in Agilent process as an example to explain the design methodology of the CMOS-MEMS accelerometer. In the later chapters, the design techniques are transferred to other processes and other IMU devices.

Chapter 3

Rotation Rate Sensor Design

The operation of vibratory gyroscopes relies on the Coriolis force in a non-inertial rotating system. When rotation Ω is applied, a moving object with mass *m* and velocity *v* experiences a Coriolis force *2mΩ×v* (see appendix). Thus by detecting this Coriolis force, the rotation is measured. This chapter uses a vertical-axis gyroscope (Z-axis) fabricated in the Agilent 0.5 µm 3 metal layer CMOS process as an example to describe the gyroscope design methodology.

3. 1 Z-axis gyroscope design

The vertical (Z-axis) gyroscope is composed of an accelerometer nested in a movable rigid frame (Figure 3-1). An outer actuator drives the rigid frame in one lateral direction (X-axis) to generates velocity, and the inner accelerometer measures the orthogonal deflection due to the Coriolis force (Y-axis) resulting from external rotation in the Z-axis.

The elastically gimbaled structure completely decouples the Coriolis sense mode from the vibration drive mode [14]. The modulation clock and sensing signals of the inner accelerometer are routed through the multi-layer springs. The top set of comb fingers on the outer rigid frame generates the electrostatic force for vibration, while the comb fingers on the bottom can sense the movement of the vibrating frame to sustain the oscillation by feedback. This oscillation provides the velocity to the nested accelerometer.

The nested accelerometer uses the same topology described in previous chapter. It is a fully differential common-centroid accelerometer with sensing fingers attached at the inner rigid frame. In the layout, each half-capacitive bridge is split into two parts and located at two cross-axis cor-
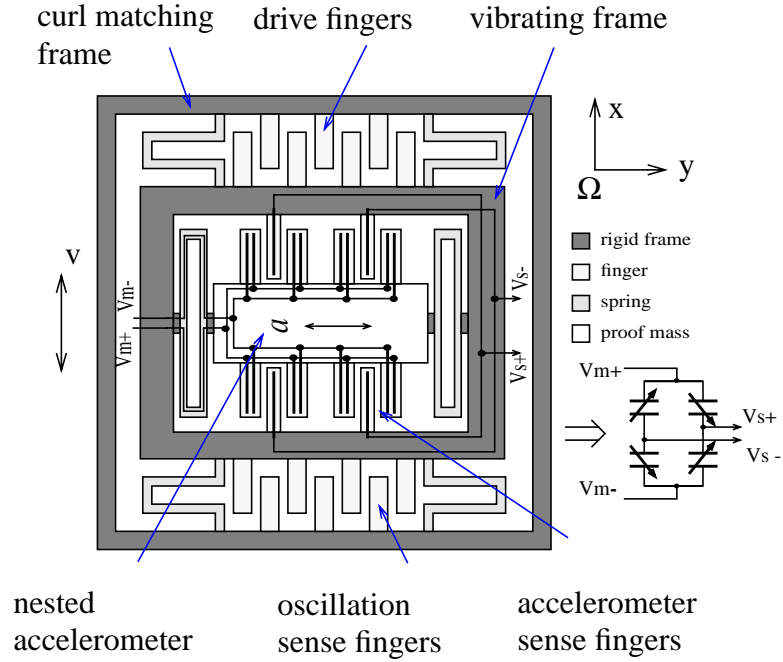
Figure 3-1. Schematic of gyroscope and inner sensing equivalent model.

ners. This common-centroid layout topology cancels common-mode input noise such as substrate coupling, power supply coupling and cross-axis vibration.

By taking advantage of multi-layer routing, a set of actuators is incorporated on the accelerometer to cancel the offset caused by fabrication variation. To avoid cross-axis actuation, the actuator is partitioned into four parts and symmetrically located at each corner of the gyroscope (Figure 3-2). Differential force fingers are biased with the highest voltage in the system (power supply voltages, V_{dd} & V_{ss}).

The gyroscope design was completed in Agilent process and simulated in Cadence SPECTRE™ using NODAS [41]. The simulation schematic is given in Figure 3-3. Some key parameters are given in Table 3-1.
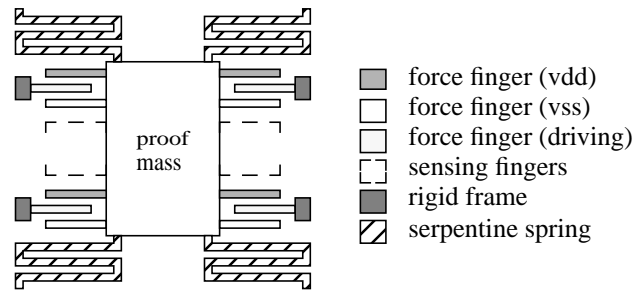
Figure 3-2. Offset cancellation actuator

Table 3-1: Layout parameters of the gyroscope

device size	$360 \, \mu m \times 500 \, \mu m$
proof mass size	$116 \, \mu m \times 372 \, \mu m$
Coriolis sense comb finger	$61.5 \, \mu m \times 3.9 \, \mu m$
drive comb finger	$11.4 \, \mu m \times 2.7 \, \mu m$
Coriolis sense finger gap	$1.8 \, \mu m$
Coriolis sense finger number	44
drive finger number	23
outer spring beams (1 turn)	$1.8 \mu m \times 105 \, \mu m$
inner spring beams (1 turn)	$1.8 \mu m \times 128 \, \mu m$

The asymmetric design between the X and Y axis results in driving and sensing modes with unmatched resonant frequencies. In contrast to matched-mode vibratory-rate gyroscopes [15] [16], the nested-accelerometer gyroscope has an advantage that it is insensitive to the drift in the resonant frequencies. The simulation (Figure 3-4) shows that the driving mode resonant frequency (9.5kHz) is lower than the sensing mode resonant frequency (11.3kHz). The lower sensing mode Q is due to large number of sensing comb fingers and relative large squeeze damping in the narrow gap. Thus, even with fabrication variation, the sensitivity of the inner accelerometer will not be significantly attenuated by the second-order slope at frequencies higher than its peak. Since the unmatched mode design does not rely on the gain of quality factor Q and its narrow bandwidth, the sensitivity variation due to frequency drift is decreased.
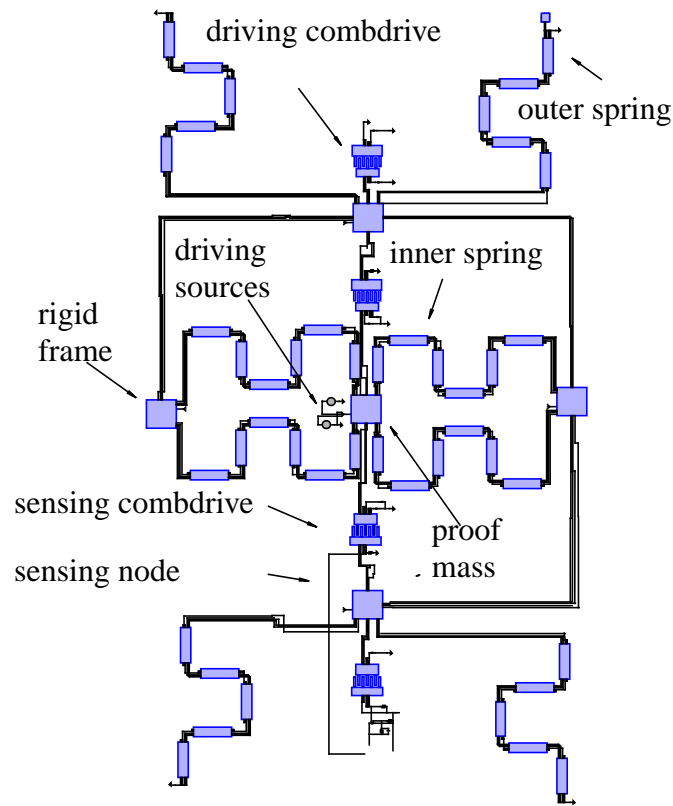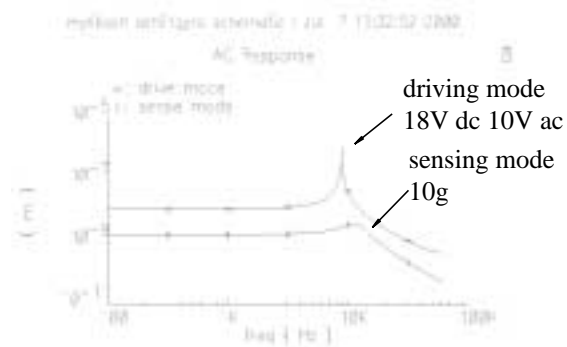
Figure 3-3. Sensor simulation schematic

Figure 3-4. Two modes of gyroscope

Figure 3-5 shows a block diagram of the complete rotation sensing system and the signals

captured at the numbered nodes. Due to the CMOS foundry process limitation, high voltage cir-

cuits are not available in the 5 V CMOS process. An off-chip high voltage (15 V) amplifier drives the top combdrive to sustain the vibration. The amplitude is set by the saturation of the driving amplifier. Once the oscillation has been built up, the applied rotation will cause a Coriolis force to act on the sensing axis of the inner accelerometer. Thus the rotation information can be recovered by demodulating the Coriolis acceleration signal. This gyroscope has a sensitivity of 0.9 µV/°/sec and noise floor of $0.03°/\text{sec}/\sqrt{Hz}$.

Figure 3-6 shows the SEM of a released gyroscope. The structure suffers out-of-plane curl of 12 µm (highest). This curl may cause coupling motion in unwanted direction, Z-axis. In a dynamic test, the outer rigid frame is applied with driving signal and the three axis motions are monitored under an optical measurement system (Microvision $^{\text{TM}}$). Figure 3-7 (b) shows that there is no significant coupling between the driving mode (X-axis) and the sensing mode (Y-axis). But as can be seen, the X-axis motion has been coupled into the Z-axis. This coupling is caused by the different vertical curl between the inner and outer structures (Figure 3-7 (a)). Since the rotor finger and stator finger are not on the same plane, there is a net upward force which drives the rotor to move vertically along with its movement in plane. It may cause coupled sensitivity in the orthogonal direction to the sensing axis.
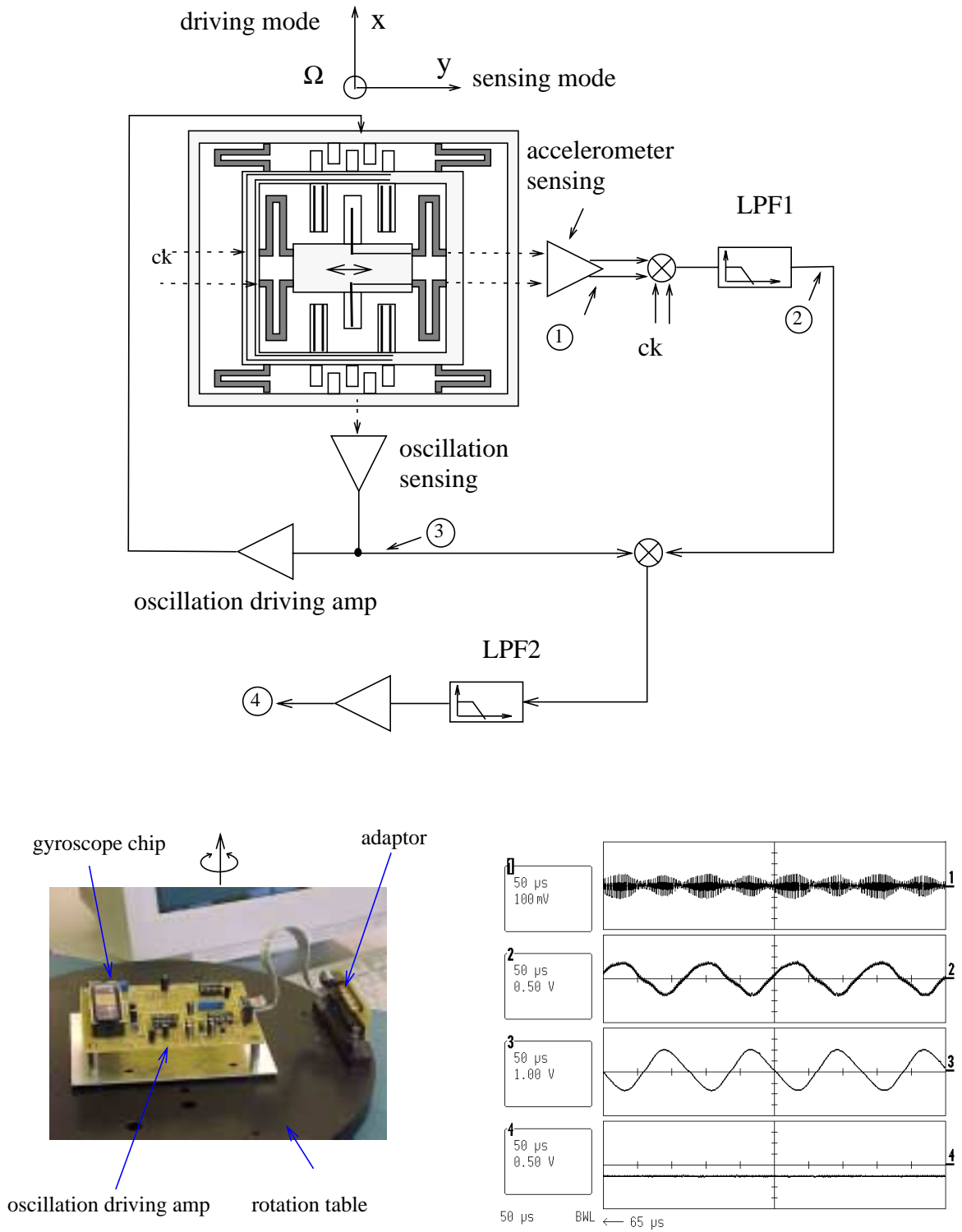
driving mode   x

Ω   y   sensing mode

accelerometer sensing

LPF1

ck⁻

①

ck

②

oscillation sensing

③

oscillation driving amp

LPF2

④

gyroscope chip   adaptor

oscillation driving amp   rotation table

1
50 µs
100 mV

2
50 µs
0.50 V

3
50 µs
1.00 V

4
50 µs
0.50 V

50 µs   BWL ← 65 µs

Figure 3-5. (a) Block diagram of gyroscope system. (b) Test set-up. (c) Signals captured at numbered nodes.
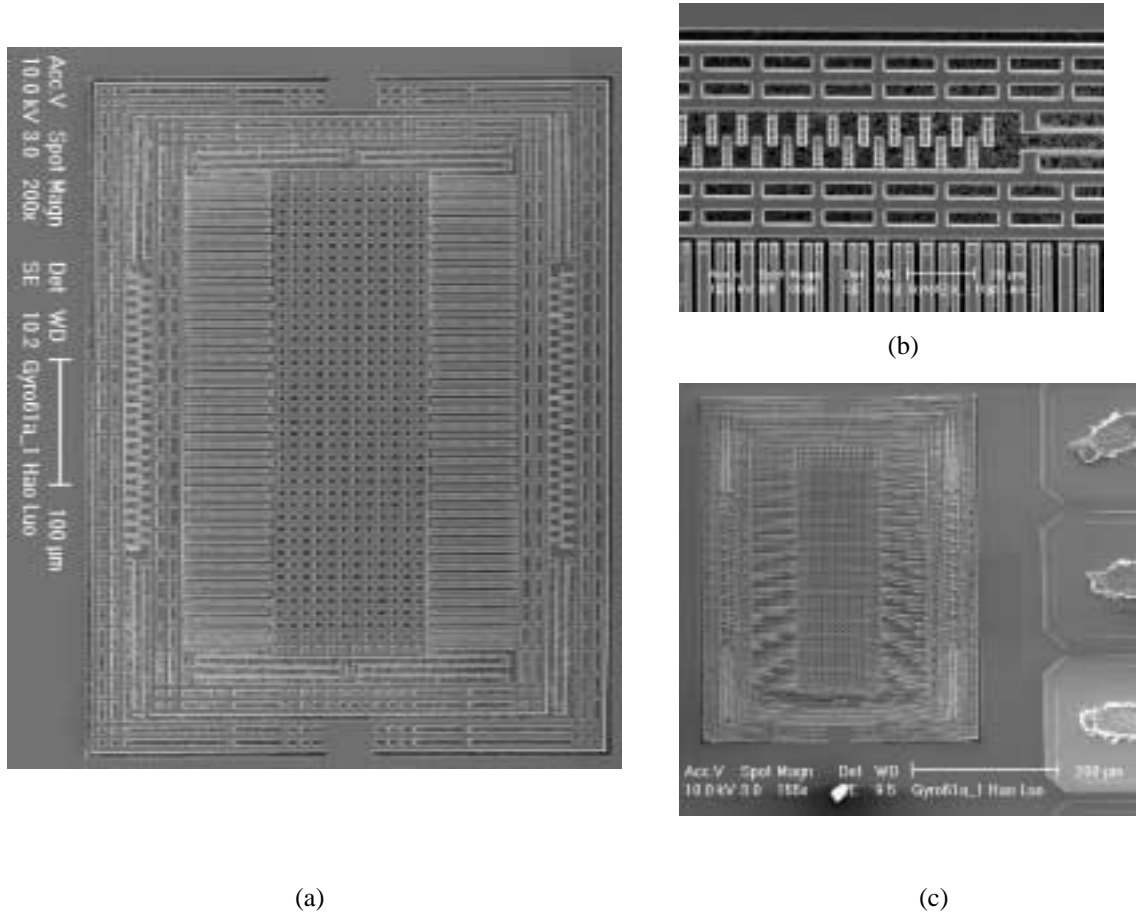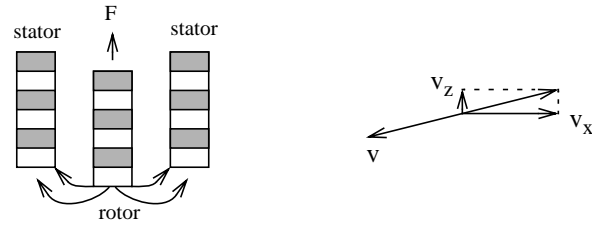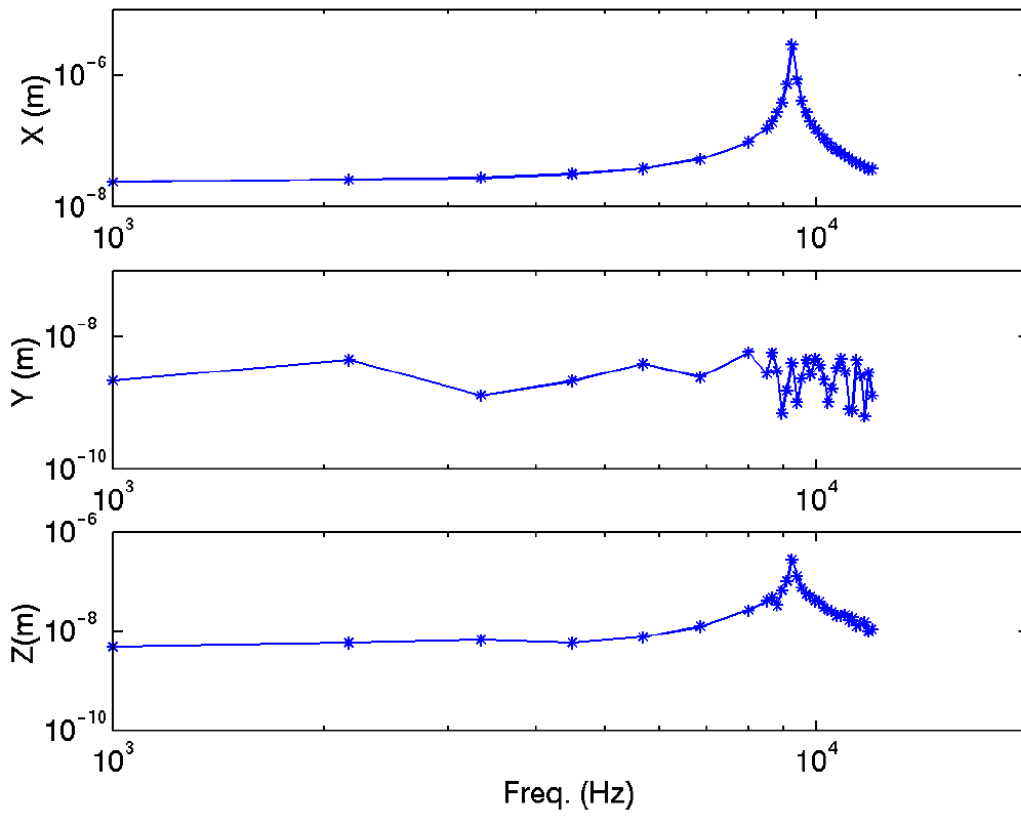
(a)

(b)

(c)

Figure 3-6. (a) SEM of the gyroscope. (b) Comb fingers and rigid frame. (c) Out-of-plane curl.

(a)

(c)

Figure 3-7. (a) Mode coupling mechanism. (c) Gyroscope three axis motion coupling.

3. 2 Optimization of curl matching

The previous described accelerometer and gyroscope was designed and fabricated in Agilent process. After the layout was transferred into AMS process, it was found out that the same layout could not achieve the same good result of curl matching. This is because the AMS process material has higher stress than the Agilent process. As a result, the structure curling causes the comb finger to be completely mismatched (Figure 3-8). Thus the curl matching technique or the device shape has to be redesigned.

The previous curl matching technique neglects the two-dimensional nature of the curl. The structure not only curls along the anchored axis, it also curls across that axis. Actually it curls along all the directions centered at the free body -- it always tends to curl like a piece of coconut shell.

In the low stress process, the outer frame curl along the long axis is restrained by the two anchor points. The curl along the short axis is not that severe because of the short dimension. Thus the curling matching between inner structure and outer structure is acceptable. But in the
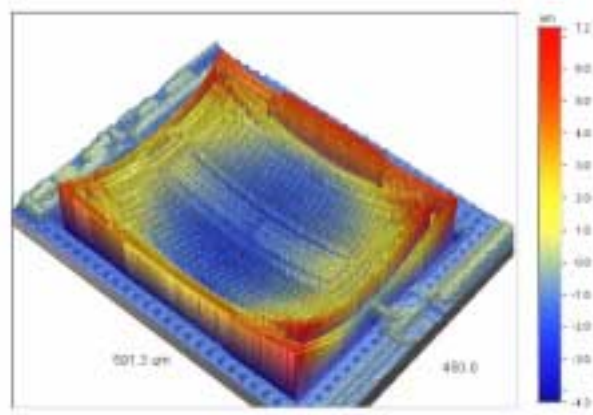

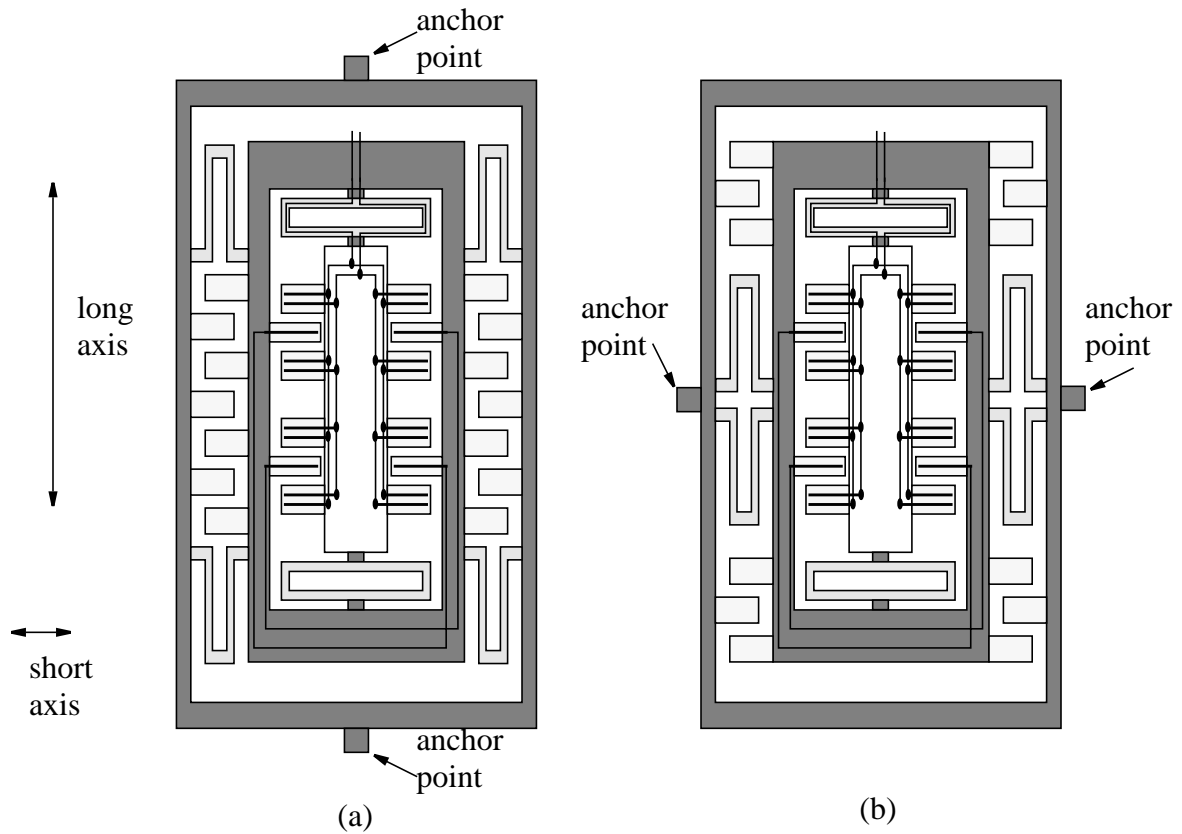Figure 3-8. Curl measurement of a gyroscope fabricated in AMS process.

Figure 3-9. Two gyroscope design topologies.

high stress process, those assumptions can no longer stand--the good matching result can not be repeated.

Based upon the analyses above, an improved design topology is developed. First let's look at two gyro design examples (Figure 3-9). These two designs have the same dimensions and similar structures except the difference in the position of the springs and anchor points. Figure 3-9 (a) is the old design which is anchored at the two ends of the long axis while Figure 3-9 (b) is anchored at the two ends of short axis and the springs are relocated to the center. The curling effect of these two designs were simulated by Coventorware™ (MEMCD).
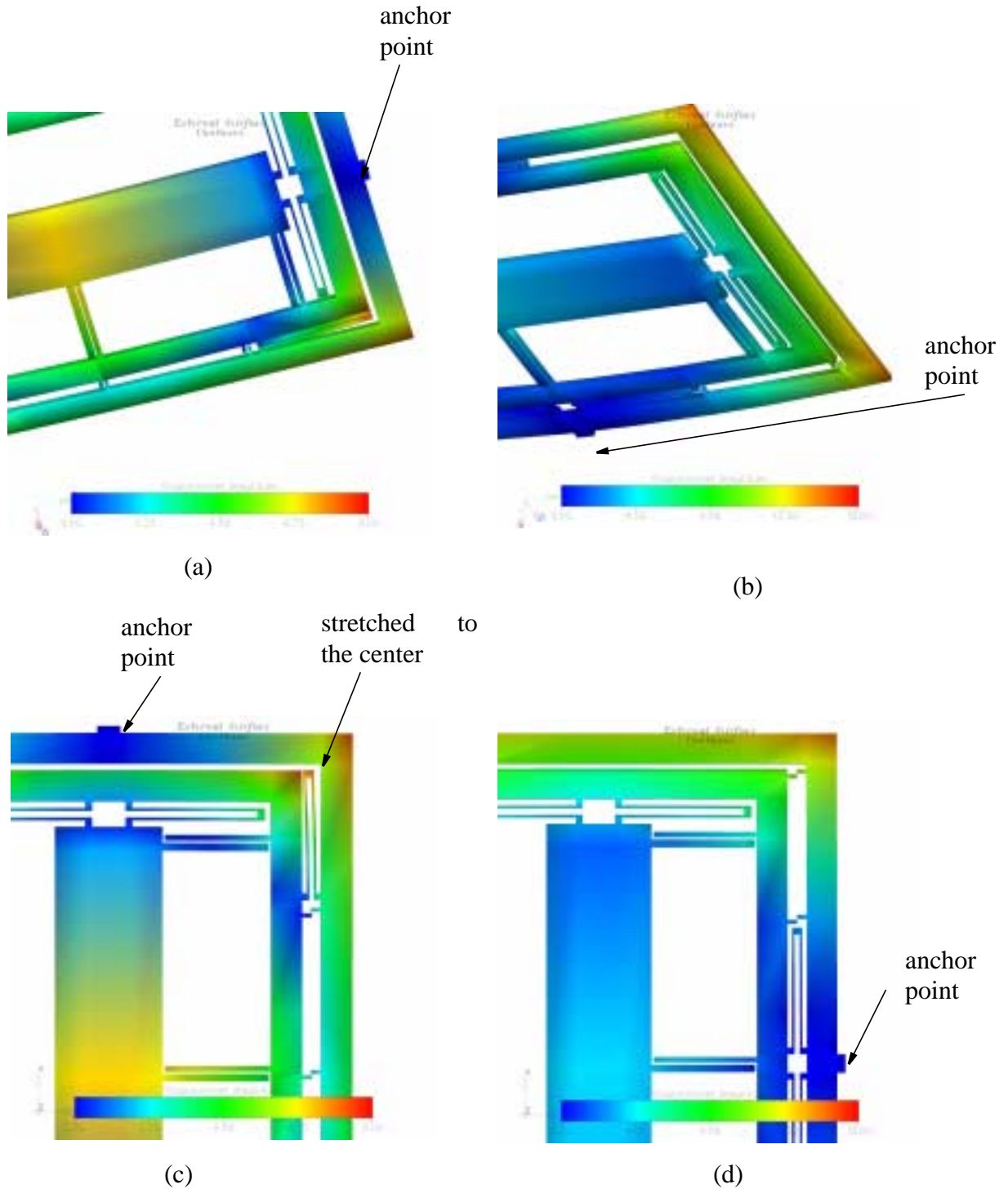
(a)

(b)

(c)

(d)

Figure 3-10. Curl simulation of two gyroscope design. (a) Vertical curl of gyro anchored along the long axis. (b) Curl in plane of gyro anchored along the long axis. (c) Vertical curl of gyro anchored along the short axis   (d) Curl in plane of gyro anchored along the short axis.

As can be seen from Figure 3-10 (a), the inner accelerometer has good vertical curl matching but the outer drive fingers miss each other. The new design (Figure 3-10 (b)), has good vertical curl matching on both inner and outer structure, even though the outer frame has larger absolute curl displacement. The picture of in-plane displacement (Figure 3-10 (c) & (d)) shows that the spring of the old design (Figure 3-9, a) curls towards the center while the lateral curl of the new design (Figure 3-10, b) is much less.

The spring is a soft stress release structure. Since the inner accelerometer (including the frame) is suspended by four springs, it tends to curl and contract. If the two outer springs are located far away to each other (old design), the contraction effect is significant and thus the spring is dragged towards the center (Figure 3-10 (c)). The outer springs of the new design are close to each other. Thus the contraction effect is not significant and the springs can still keep their original shape.

The inner accelerometer is suspended by four outer springs, and its stress is partly released. For a structure with stress released, the adjacent points have similar curl height-- that is why the suspended accelerometer has good curl matching. The simulation and explanation above are verified by the FEM simulation and measurement results (Figure 3-11).

As a summary the techniques to improve the curl matching are listed below:

- Use small stress gradient process and structure. In the layout design, use as much metal layers as possible, because the multi combined layer has smaller stress gradient. It was found that designing an active field layer underneath the structure can significantly decrease the stress gradient. It is because the active layer removes the field oxide which is compressive when grown by wet oxidation in CMOS steps.

inner and outer structures are
completely mismatched.

inner and outer structures
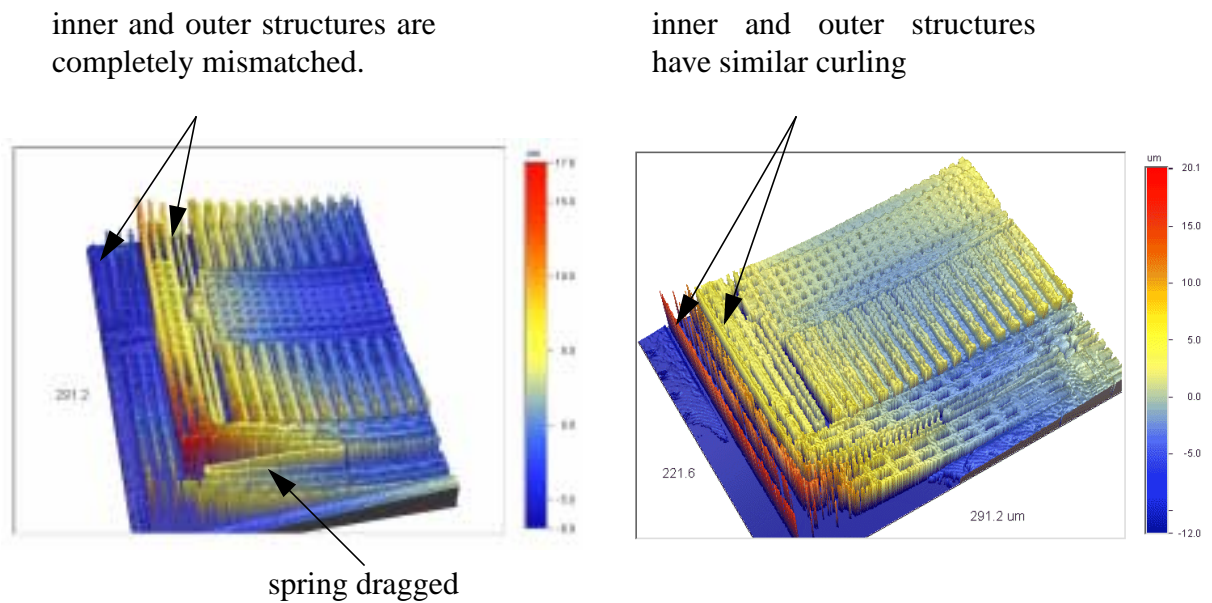have similar curling

spring dragged

Figure 3-11. Curl measurement comparison of two designs. (a) Anchored at two long-ends. (b) Anchored at short-ends.

- If possible, choose a design with small dimensions. Smaller structures always have smaller curl effect. Of course, small designs sacrifice the sensor performance.

- Use suspended curl matched stator structure. Suspension enables the internal stress to be released. As a result, the suspended structures have better curl matching than those with stators anchored directly on the rigid substrate.

- If the structure has to be anchored at multiple points, anchor at the shortest axis and put the suspension springs close to each other.

After taking all of the above curling improvement steps, the structure curling can reach a very satisfactory flatness in some cases (Figure 3-11).
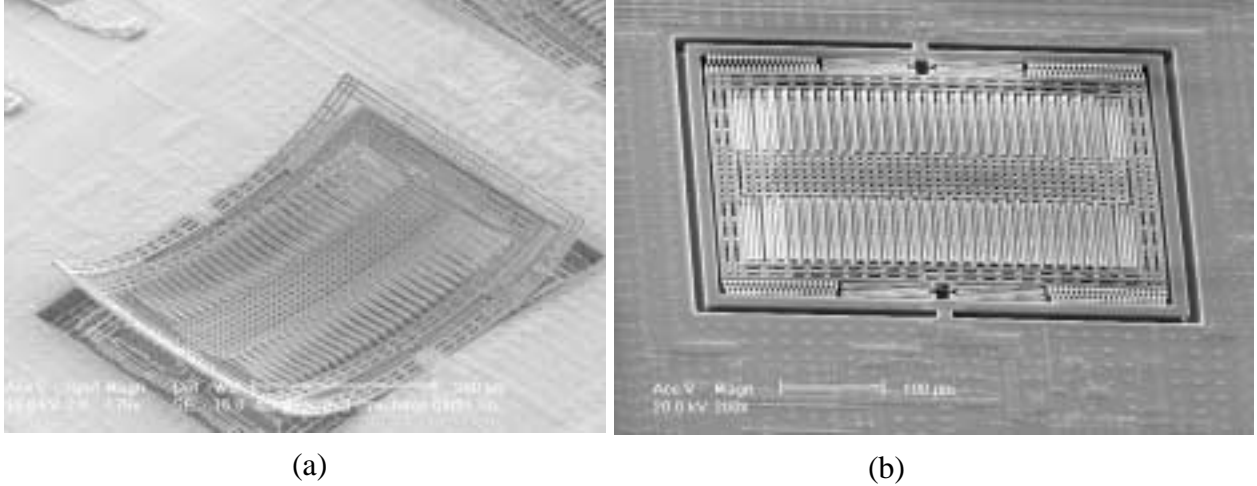
(a)   (b)

Figure 3-12. Two gyroscopes fabricated in AMS process with similar size. (a) Gyroscope without curl matching improvement. (b)Similar gyroscope with curl matching improvement (with N active layer, all metal layers).

3. 3 Copper CMOS-MEMS gyroscope

As described previously, the main limitation of the CMOS-MEMS process used in this project is the structural curling. Due to relatively high residual stress (compared to uniform material process), normally the device dimension is limited under 700 μm. To exploit the CMOS-MEMS technology into other process, a gyroscope was fabricated in the UMC 0.18 μm six copper layer low-k CMOS digital process. The reason to choose the copper process includes a) the copper layer is electrically plated at low temperature with Dual Damascene process and it has lower stress, b) six combined copper and dielectric layers provide thick structures (8 μm Cu vs. 5 μm Al). Compared to three layers in the aluminum version, the CMP copper process is more

uniform and is expected to have less curl. Other benefits from the copper process include higher mass density (8.96 g/cm^3 Cu vs. 2.7 g/cm^3 Al) and low-k oxide. The mass is critical for inertial sensing as it sets the fundamental noise floor. The low-k process results in lower parasitic capacitance which is preferred when on-chip capacitance sensing technology is employed.

The layout of circuits with microstructure patterning in the metal layers is first sent out for copper chip fabrication. After the foundry fabrication, two dry etch steps, similar to the aluminum CMOS-MEMS process, are performed to define and release the mechanical structure. Due to different properties of the copper chip, the releasing process is tuned to fit the copper version (Plasma Therm 790 chamber, 80 W, CHF$_3$ 25sccm, O$_2$ 22.5 sccm, 60 mtorr, DC bias 350 V, etching time 350 mins). The released copper structures show some different properties from Al structures. First, the copper will suffer corrosion when exposed to moisture in the air. Secondly, the structures are easy to stick together and difficult to pull them apart electrostatically. So large contact area must be avoided by stops.

Since the copper gyroscope is expected to have much lower curl, the outer curl matching frame is no longer necessary. The outer driving comb fingers are directly anchored on the substrate. One more benefit of this change is that it decreases the routing path from the sensor to the circuits and thus parasitic capacitance is decreased. Table 3-2 summarizes some design parameters and comparison between the copper and aluminum gyroscope.

3. 4 Copper CMOS interface design

The utilized copper CMOS process is a low voltage (1.8 V~3 V) digital CMOS process. To avoid offset saturating the circuit, a low gain front-end interface is desired. An on-chip unity gain sensing buffer is designed to detect the capacitance change due to deflection of comb fingers (Fig-

Table 3-2: Design parameter comparison between copper and aluminum gyros

|	Copper (UMC)	Aluminum (Agilent)
transducer size	330 μm × 410 μm	360 μm × 500 μm
layer used	6 layer of copper	3 layer of aluminum
structure thickness	7.5 μm	5 μm
sense comb fingers	85 μm× 4 μm × 40	61.5 μm× 3.9 μm × 40
drive comb fingers	7.8 μm× 2.4 μm × 27	11.4 μm× 2.7 μm × 23
driving mode spring	88 μm× 1.8 μm × 1 turn	105 μm× 1.8 μm × 1 turn
sensing mode spring	102 μm× 1.8 μm × 1 turn	128 μm× 1.8 μm × 1 turn
driving mode resonant frequency	8.8 kHz	9.02 kHz
sensing mode resonant frequency	9.0 kHz	11.0 kHz
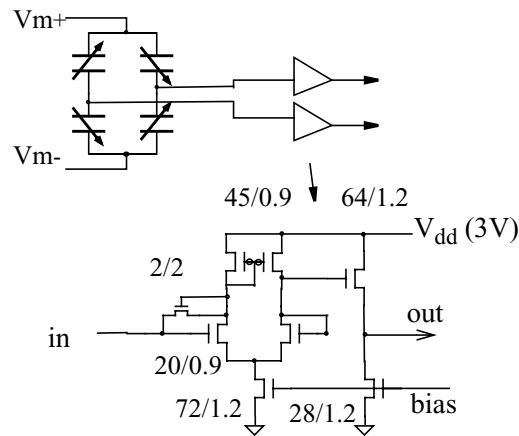
Figure 3-13. Capacitive sensing interface

ure 3-13). The biasing problem of the capacitive sensing interface is solved by using a small transistor (W/L=2μm/2μm) working in the subthreshold range with diode connection between the gate and drain of the input transistor. The rest of the gyroscope system is implemented off-chip.

Figure 3-5 shows the SEM of the released gyroscope. Optical profilometer measurements of
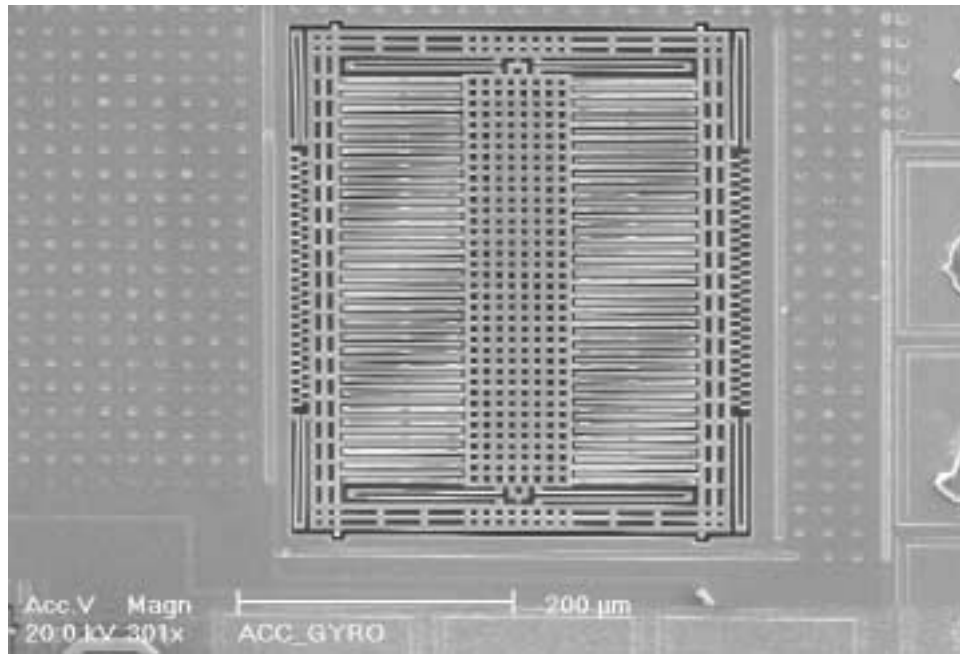

Figure 3-14. SEM of a copper gyroscope.

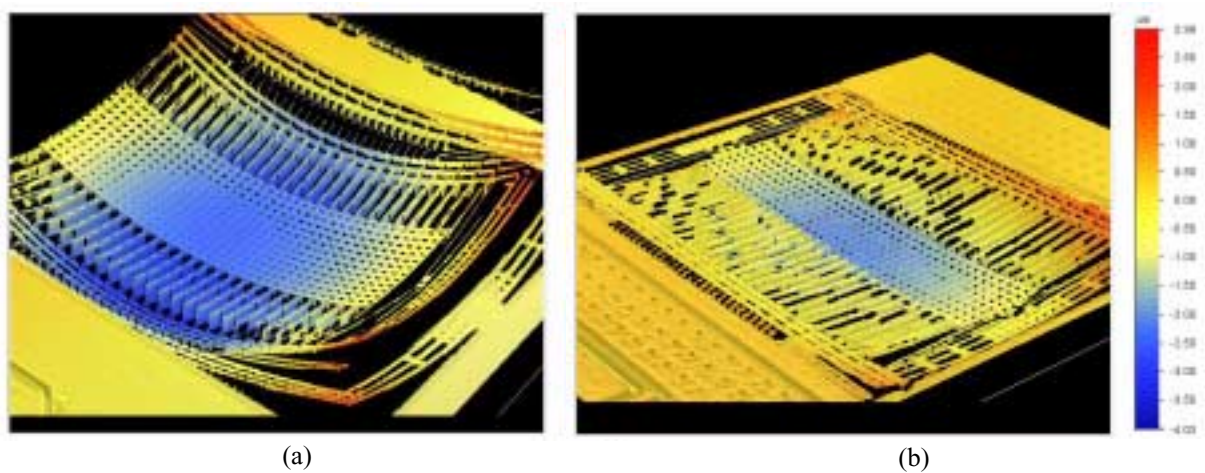the copper gyroscope and its aluminum counterpart are shown in Figure 3-15. As expected, the

Figure 3-15. Curl comparison. (a) Aluminum gyroscope. (b) Copper gyroscope.

copper structure has much less curl than the aluminum version (maximum vertical curl: Cu 2 μm vs. Al 12 μm).

In the dynamic test, the three-axis motion of the dithered proof mass in driving mode (Figure 3-16) is measured by sweeping the frequency response with an applied voltage on the actuator (5 V_{DC} + 5 V_{AC}). As can be seen, there is no substantial coupling between the driving mode (X-axis)
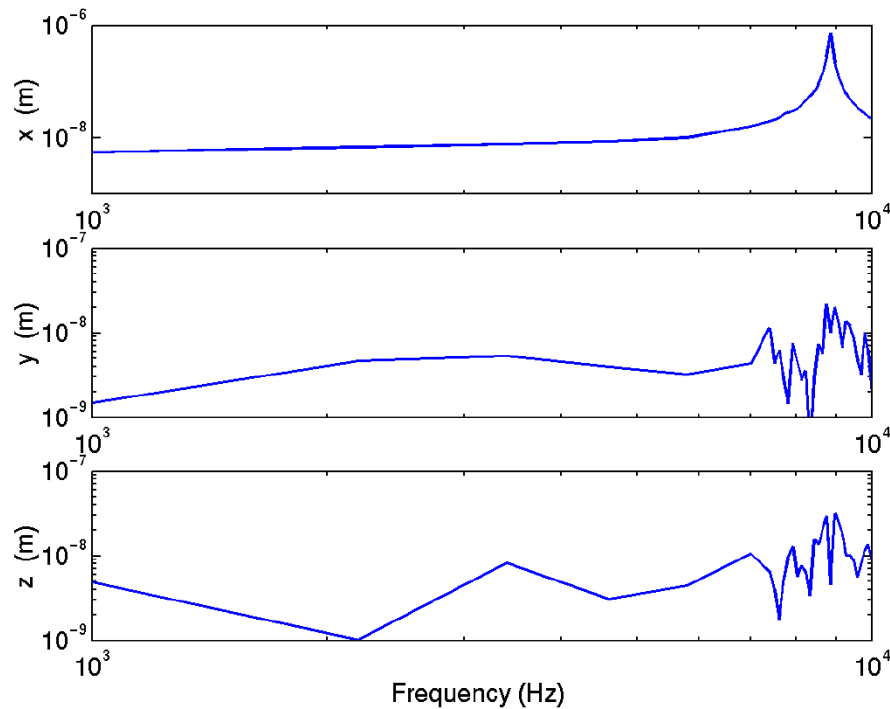

Figure 3-16. Copper gyro proof-mass three axis motion in driving mode.

and sensing mode (Y-axis). The out-of-plane motion (Z-axis) is also significantly reduced compared to Figure 3-7. Figure 3-17 shows the inner accelerometer sensing mode response to an applied 1G 100 Hz acceleration in the sensing axis (Y-axis). The rotation test on a rate table shows that the sensor has a sensitivity of 0.8 μV/°/sec and noise floor of 0.5°/sec/$\sqrt{Hz}$. This number is not an improvement from its aluminum counterpart. The reason includes a) even though the copper is heavier than the aluminum, as can be seen from the Table 3-2, the copper gyroscope is

smaller than the aluminum one and the copper structure has higher effective Young's modulus. The two gyroscopes have similar resonant frequency which means they have similar physical sensitivity. b) the copper version uses a unity gain buffer as sensing interface while putting higher gain at the front stage (Al version) is helpful to decrease the whole system noise.
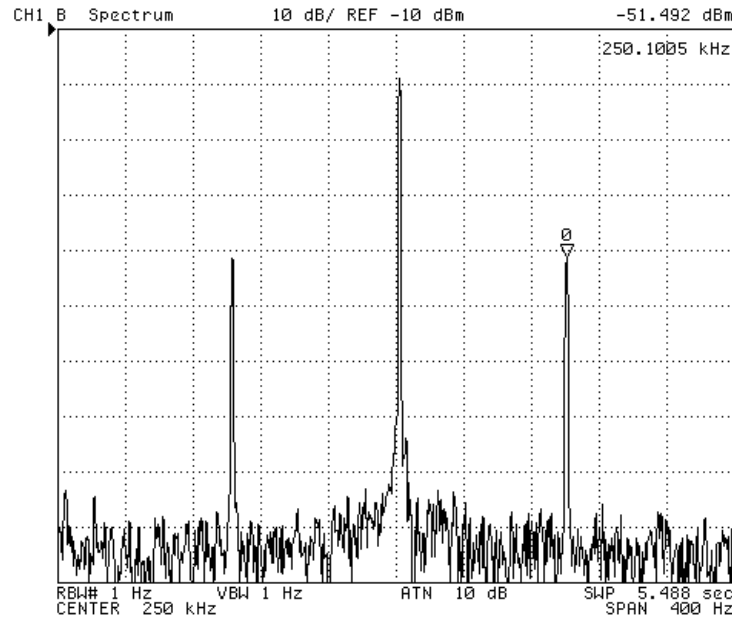

Figure 3-17. Sensing mode response to 1G 100Hz acceleration.

3. 5 Summary

In this chapter, the CMOS-MEMS gyroscope structure is described. Several gyroscope designs are introduced. The technique for improving curl matching is also investigated. The gyroscope and accelerometer (Chapter 2) are basic IMU devices which will be used in an integrated inertial measurement chip. The next chapter will talk about the supporting electronics for those IMU sensors.

Hao Luo

Chapter 4

Electrical Design and Analysis

This chapter describes the electrical design for the accelerometers and gyroscopes. As a fully functional integrated system described in previous chapters, the integrated IMU includes sensing units and necessary supporting circuit blocks. Those supporting circuits are composed of a sensing buffer, demodulator and bias (Figure 4-1). Each of those function blocks will be discussed in details in this chapter.

4. 1 System description

In the accelerometer system, modulation signal is sent into the sensor and the output from the sensor is modulated by the applied acceleration. This sensing signal is amplified by the capacitive sensing amplifier and demodulated by the demodulator. Then it is filtered by the low-pass-filter (LPF) to remove the high frequency part.

In the gyroscope system, an oscillation sensing buffer senses the motion of the gyroscope driving mode. The driving mode signal is amplified by the driving amplifier and fed back to the gyroscope driving actuator stator comb fingers. The rotor comb fingers are biased at high dc voltage (10~30 V, the electrostatic force is proportional to $V_{dc} \bullet V_{ac}$). This feedback loop drives the inner accelerometer frame into oscillation to generate the velocity. The capacitive sensing amplifier boosts the sensing mode signal amplitude and feeds to the first demodulator. The Coriolis signal is recovered after the first time demodulation. It needs the second time demodulation to recover the rotation signal. If the gyroscope driving mode quality factor Q is not high enough (it may also caused by the demodulator output LPF), there might be a small phase error between the

Coriolis signal and the oscillation signal. Then an additional small phase tuning is needed before

the oscillation signal being sent to the second demodulator. It can be done by simple RC network.

All the on-chip circuits is biased by the on-chip constant-g_m bias circuit
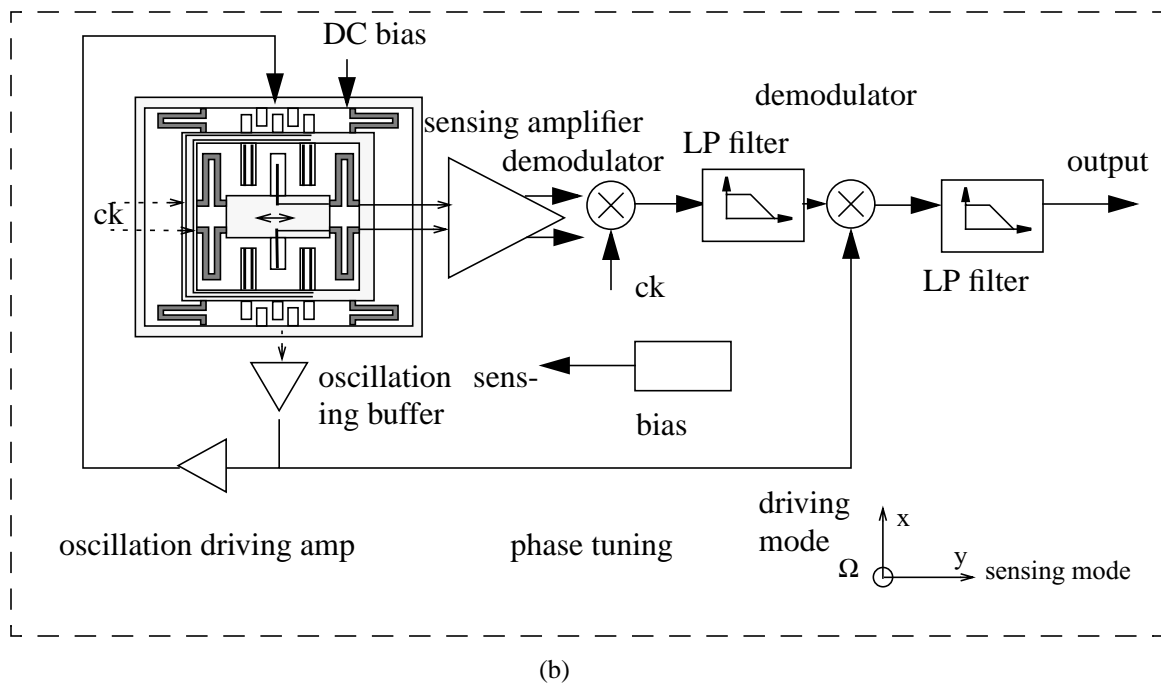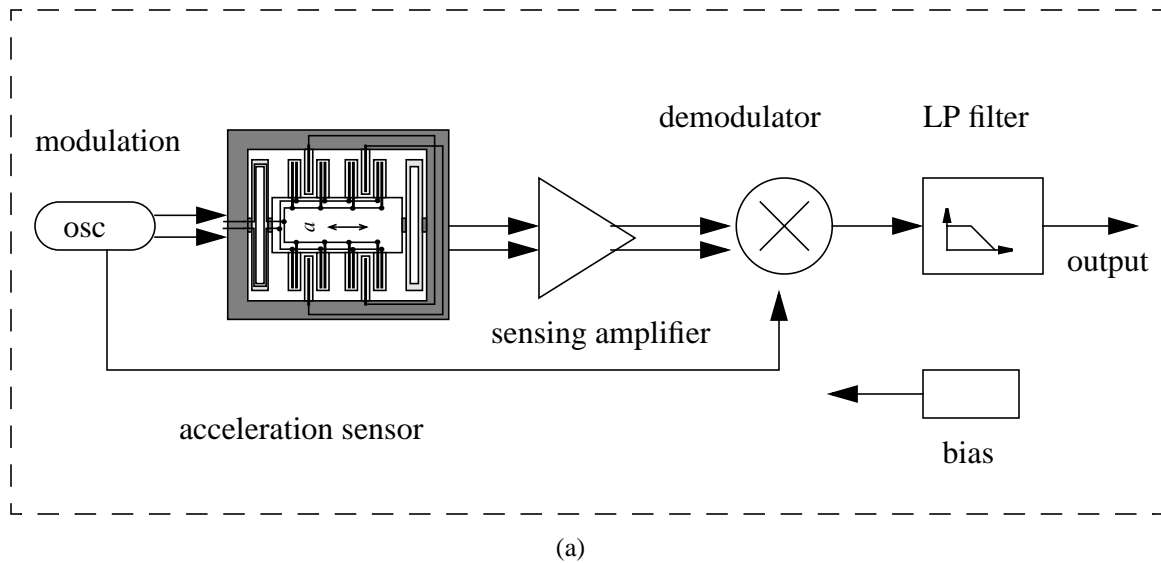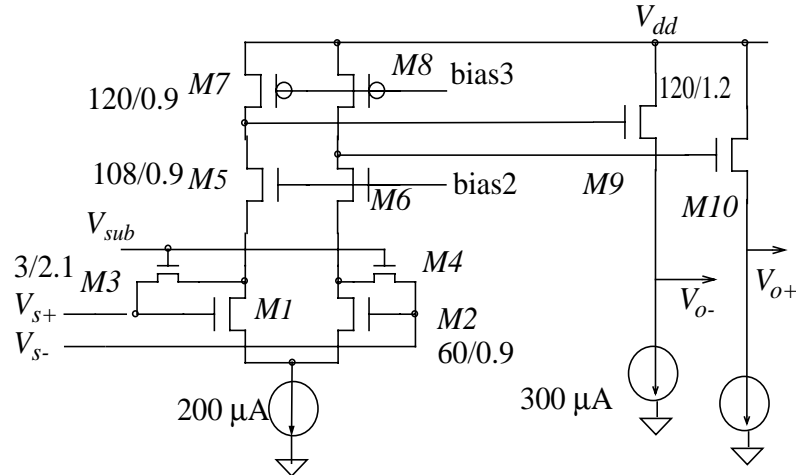

(a)

(b)

Figure 4-1. (a) Accelerometer block diagram. (b) Gyroscope block diagram.

Figure 4-2. Differential capacitive sensing amplifier designed in Agilent 0.5 μm process

4. 2 Capacitive sensing amplifier

The primary challenge in the design of the interface circuits is to detect extremely small capacitance. An interface preamplifier designed in Agilent 0.5 μm process is chosen as an example (Figure 4-2). The capacitive bridge d.c. bias problem is set by two small transistors (*M3* and *M4*) working in the subthreshold region. They exhibit large resistance with negligible source to drain capacitance. The cascode topology has low input capacitance due to small Miller effect. The input terminal dc bias voltage is set by the transistors' transconductance g_m. Using dc common mode feedback can set this bias voltage to a more accurate value, but the feedback will inevitably introduce more noise. Thus the open-loop topology is chosen. The common dc voltage needs to be cancelled by later stage (see section 4.3)

Since the system noise level is dominated by the first stage, an input stage with large gain is essential to the system performance. Simulation shows the input sensing amplifier has a gain of 80 and bandwidth of 5 MHz with 10 pF capacitance load.

Since the input signal is modulated at a relatively high frequency of 2 MHz, assuming the electronic flicker noise is out of the bandwidth of interest, the thermal noise of the transistors becomes the dominant source of electronic noise and its spectral density is given by (E 4-1)

$$\frac{v^2}{\Delta f} = 4k_B T \left(\frac{2}{3}\right) \frac{1}{g_m} \tag{E 4-1}$$

The sensing buffer has a referred input noise of

$$\frac{v^2}{\Delta f} = 4k_B T \left(\frac{2}{3}\right) \frac{1}{g_{m1}^2} [2g_{m1} + 2g_{m7}] + 2\frac{I_{n3}^2}{g_{m1}^2} \tag{E 4-2}$$

where the times of *2* arises from the symmetry of the differential pair and the I_{n3} has been derived in [46]

$$I_{n3}^2 = 4k_B T \left(\frac{k_B T}{q}\right) \frac{W_3}{L_3} \mu C_d exp\left(\frac{1}{n} \frac{q}{k_B T}(V_{th0} - V_g') - \frac{1}{2} \frac{q}{k_B T} \Psi_F\right) \tag{E 4-3}$$

and where Ψ_F is the Fermi level, μ is the low-field mobility, V_{th0} is the transistor threshold voltage, n is a process dependent factor, and C_d and V'_g are the depletion capacitance and gate voltage, respectively, when the surface potential is equal to 1.5 Ψ_F. Practically, it is difficult to extract the noise of the I_{n3}. HSPICE simulation shows that noise contribution of I_{n3}^2 is 1000 times smaller than other transistor noise and can be neglected (however, an accurate SPICE noise model for subthreshold transistor is not available). The sensing preamplifier is simulated to have a referred input noise of 12 nV/$\sqrt{Hz}$. If the sensitivity of the sensor is 1 mV/G, the equivalent circuit noise is 12 μG/$\sqrt{Hz}$.

4. 3 On-chip switched-capacitor demodulator

Demodulator transfers the modulated sensing signal back to its baseband. It may or may not have extra gain. There are several considerations for the on-chip demodulator. First, due to limited bonding pads, it is on-chip directly coupled from the front-end sensing amplifier, which easily shows a large DC offset. Thus the demodulator has to have the capability to cancel the DC offset in the input signal. MOS differential pair transistors normally have large offset than bipolar input pairs. This offset is in the range of tens of millivolts even with careful layout design. In the MEMS sensing case, due to the limitation on the size of the input transistors (normally around 60 μm wide), the differential pair have even larger offset in the range of 20~80mV. This offset is amplified by the gain of front-end sensing amplifier to several hundred millivolts or even over one volt. This offset can easily saturate the demodulator input transistor of a mixer using Gilbert cell. Secondly, the sensor unit inevitably has an AC modulation offset due to process variation (Figure 4-3). The sensor unit exhibits a constant AC output signal even without any applied acceleration. It is impossible to distinguish this AC offset from the real physical agitation signal, e.g., a constant gravitation acceleration input. It will be demodulated and show as a constant DC signal in the final output. Thus the demodulator needs an offset adjustment terminal to compensate the sensor AC offset. Thirdly, the demodulator is preferred to have a fixed gain.

The demodulator used for the IMU system is shown in the Figure 4-4. It is a switched-capacitor demodulator. Its operation is time multiplexed into five phases: a) signal sampling (ck1 & ck2), b) charge transferring to cancel input DC offset (ck3), c) output sampling and holding (ck5), d) AC offset adjustment (ck1 & ck3), and e) reset (ck4). The clocks' phases are key to the proper function of this demodulator. First, all the clocks are non-overlapped which will prevent the capacitors from being improperly discharged during clock switching periods. Secondly, the main

clock 'ck' has double the frequency of the input sensing signals, V_{in+} and V_{in-}. During each sensing signal cycle T, the signals will be sampled by C1 twice but with inverse polarity on the second sample. Sampled charges of each time is transferred and accumulated on the same capacitor C2, thus the DC offset of the input signals is canceled while the AC signal is kept. The AC offset adjustment is done by a separate branch of C_ofs. One benefit of this AC offset adjustment scheme is that when the adjustment is performed it does not effect the demodulation gain. As with other switched-capacitor circuits, the demodulation gain is set by the ratio of two capacitors, C2/C1. If two identical capacitors are used, the gain is simply determined by the cycle number N, which can be easily controlled by a digital circuit. This fixed gain has some advantages such as insensitivity to most variations. To remove the flicker noise and offset of the op-amp, correlated-double-sampling (CDS) can be applied [47].
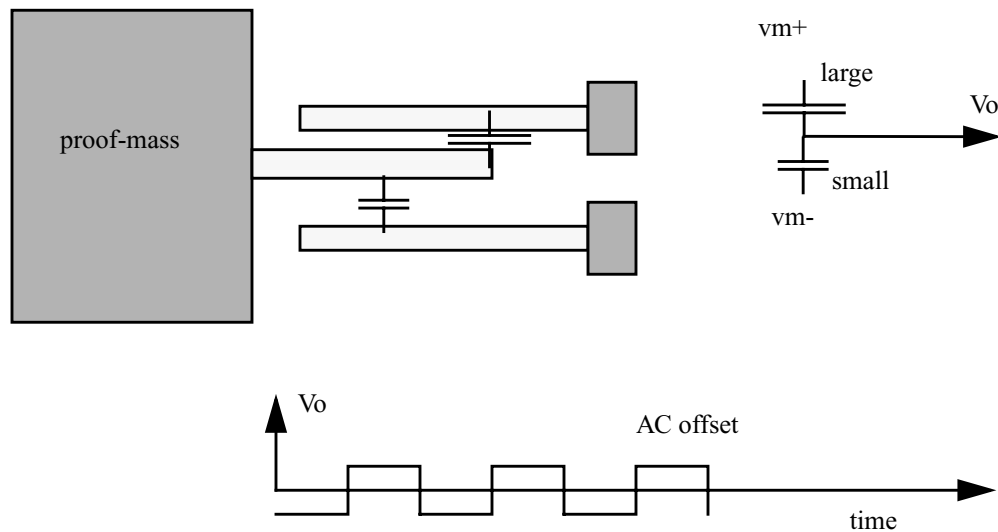
Figure 4-3. Due to fabrication variation, sensor unit is not centered and shows an AC offset
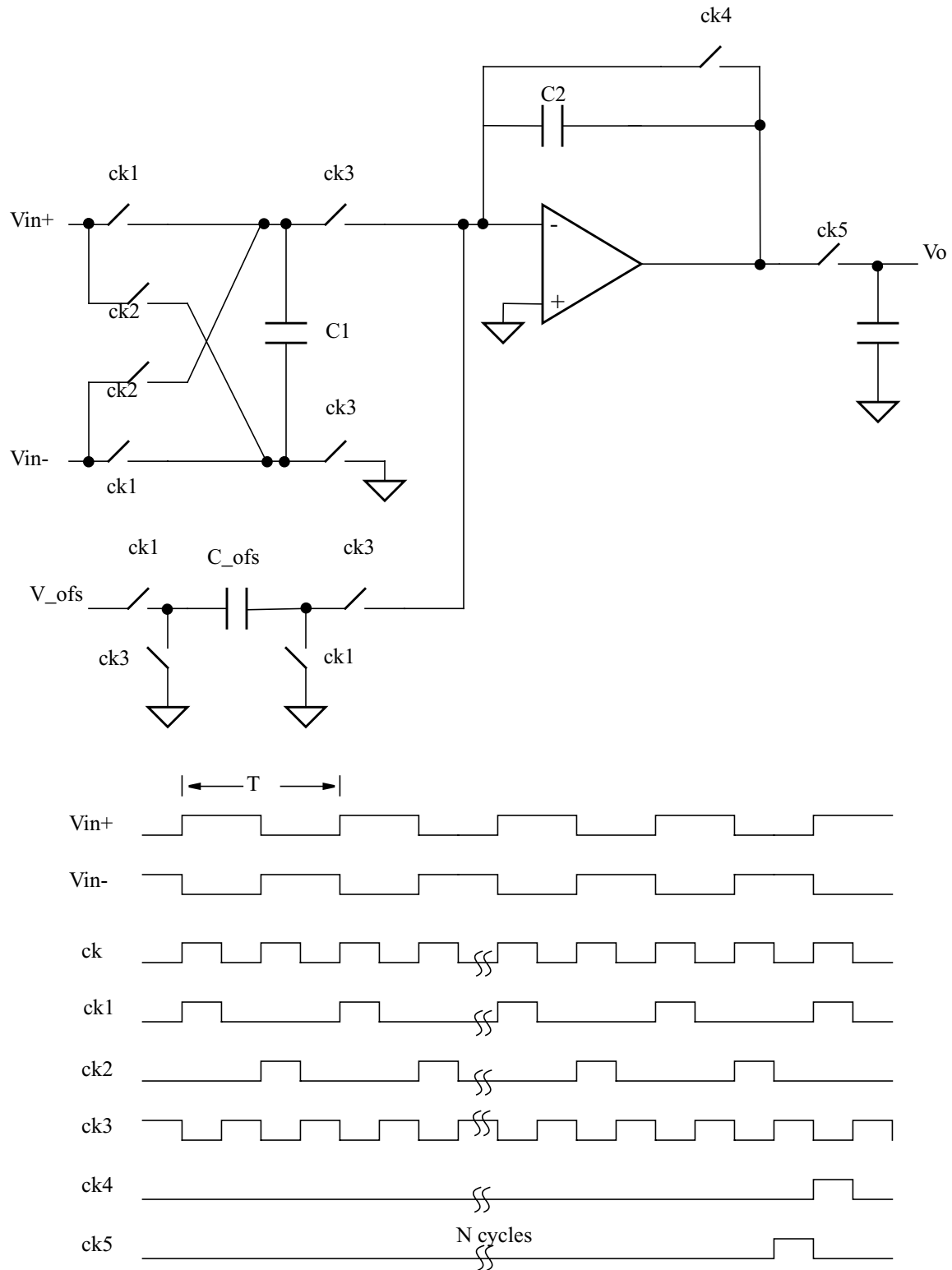
Figure 4-4. Schematic of switched-capacitor demodulator and its control clocks
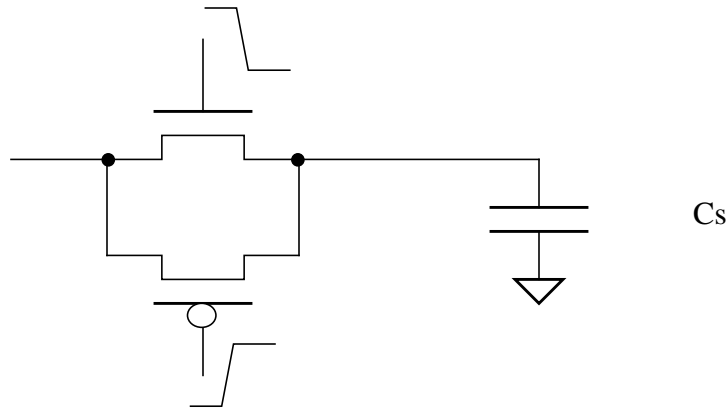
Figure 4-5. Complementary switch

The are two inherent challenges, charge injection and higher noise, in the switched-capacitor circuits if not designed correctly. Charge injection error is directly related to the switching signal's amplitude and the capacitance. To decrease the charge injection error, a complementary switch is used. The charges stored in two different transistors have inverse polarity and thus they will cancel each other to the first order [47]. Large capacitance can also decrease the error voltage. In this work the capacitor is about 16pF. It is relatively large so the charge injection error is negligible. Another potential negative effect of switched-capacitor circuit is the noise. The main source of the output noise is the flicker noise of op-amp itself and the input signal noise fold-back phenomenon. Large p type input transistors were chosen to decrease the flicker noise. The input signal noise fold-back relies on the bandwidth. To minimize the noise fold-back effect, the input signal bandwidth must be limited which means a filter is needed. But actually, a hidden filter is embedded in the system. The capacitor C1 is chosen with a suitable capacitance so that it works with the front stage and they behave as a low-pass filter (LPF) with the desired bandwidth. As shown in the Figure 4-6, the signal bandwidth is limited at 4~5 MHz, while the switch clock frequency is around 2 MHz. The noise higher than the third harmonic is flittered out.
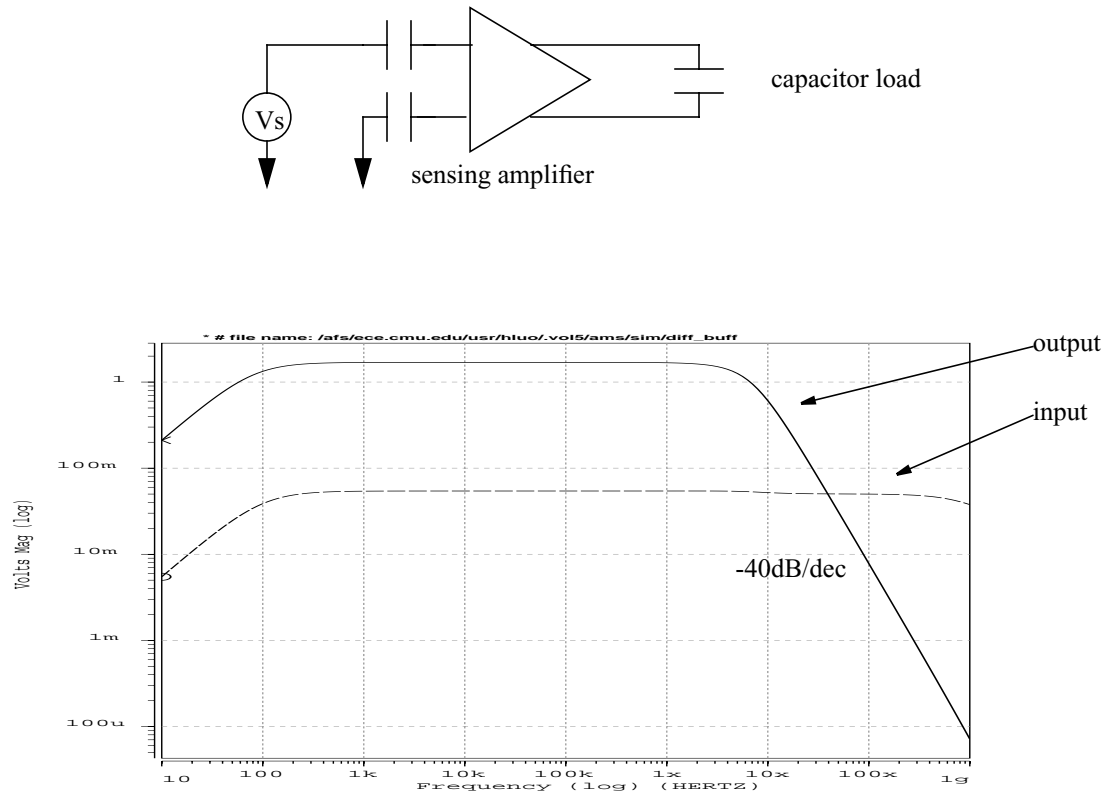
Figure 4-6. AC response of front-end sensing buffer with load of SC circuit.

The digital control unit (DCU) is also integrated on the chip. The DCU, shown in Figure 4-7, generates all the non-overlapped switching signals with correct phases. Note that this DCU is a 'negative' logic circuit which means that '0' is for switch 'on' and '1' is for switch 'off'. The non-overlapped clocks have a 8 ns gap between adjacent clock edges. This gap prevent the capacitor from being incorrectly deischarged. The waveforms of the combined DCU and SC demodulator are shown in Figure 4-8.
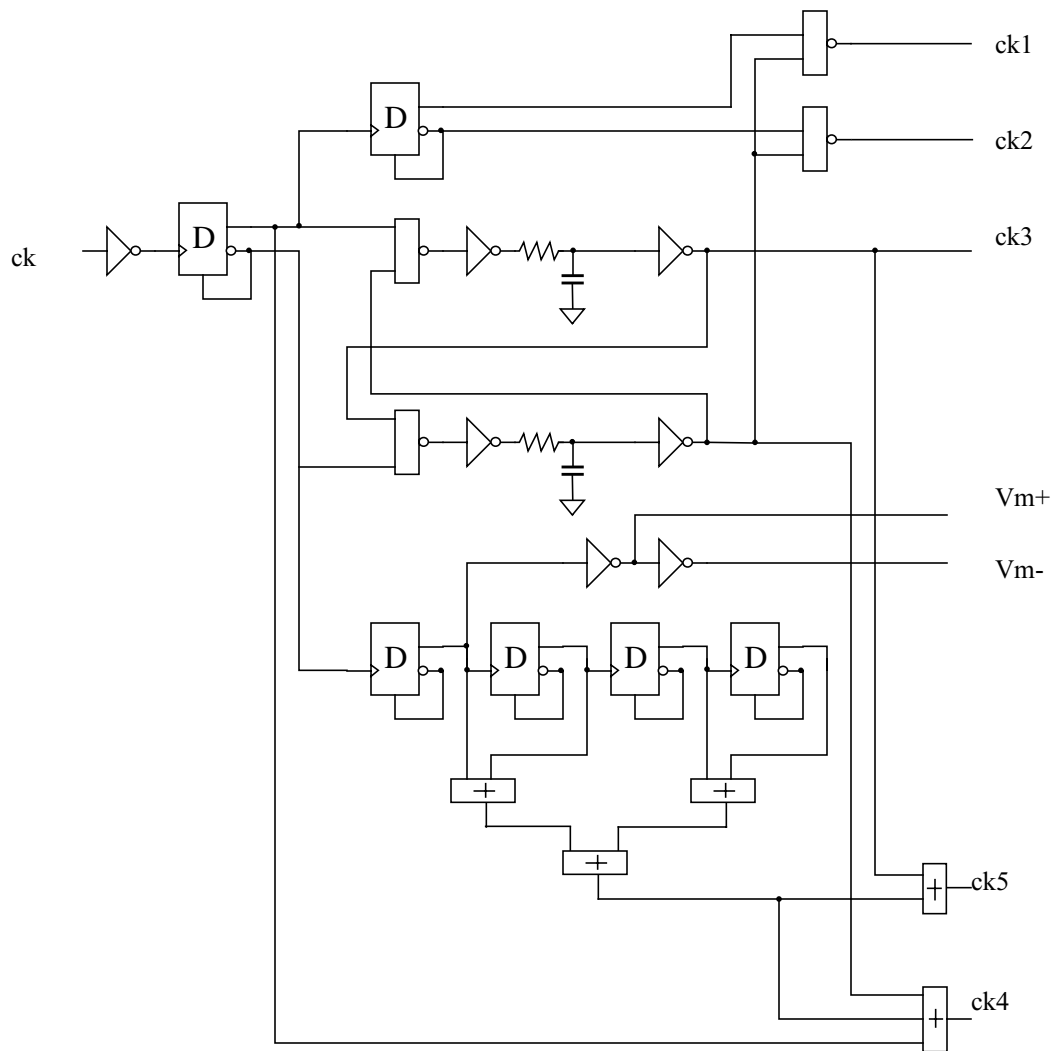
Figure 4-7. Schematic of DCU
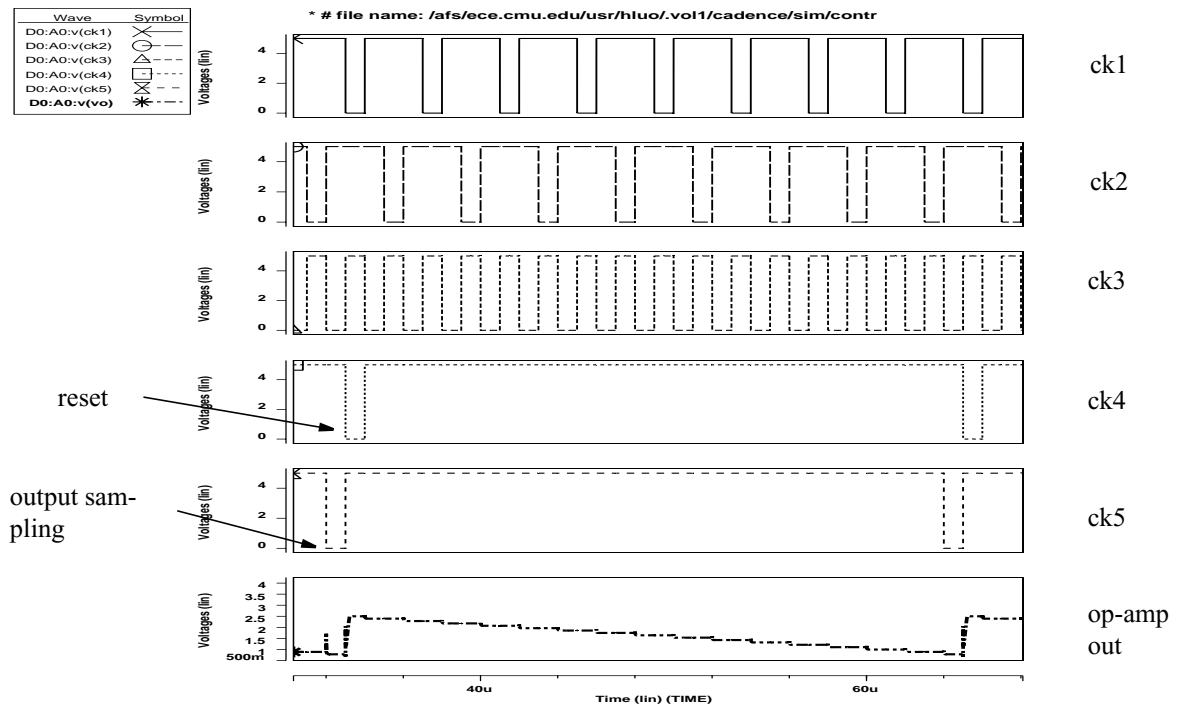
(a)
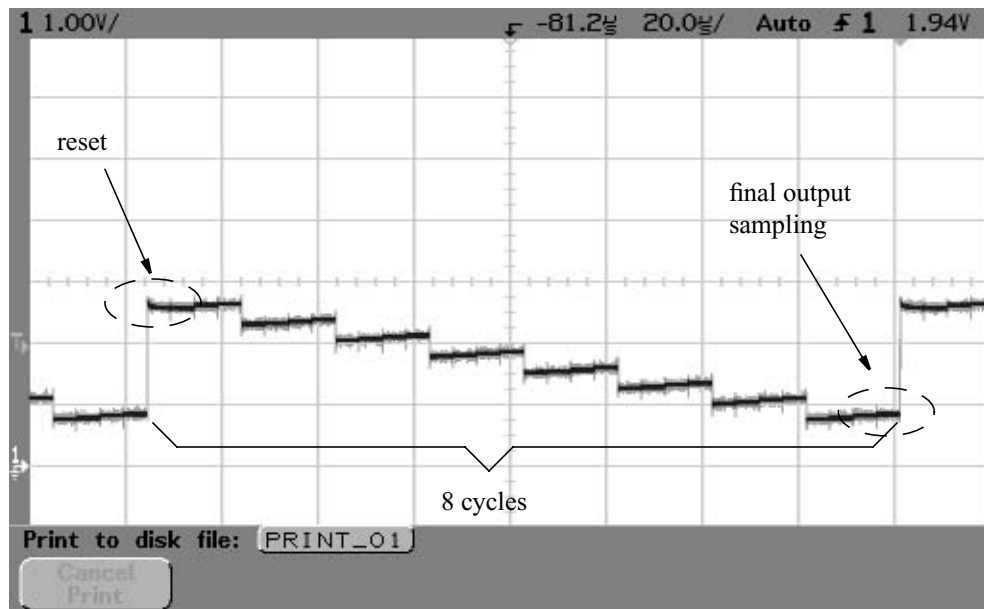
(b)

Figure 4-8. (a) HSPICE simulated waveforms of control clocks and output
of op-amp. (b) Op-amp output waveform captured by oscilloscope.

4. 4 Op-amp used in SC-demodulator

The op-amp used in the SC demodulator requires enough gain and speed to settle the final output. Normally a gain higher than 70 dB is enough for SC circuit. Since it is connected in reverse gain topology, it does not require large common mode input range. Thus there is no need to design a complementary input stage to have a rail-to-rail input range although the rail-to-rail output is still preferred. Because the final demodulated signal comes from the op-amp, it is preferred to have a PMOS input stage to minimize the flicker noise. The SC circuit requires the op-amp to have enough unity-gain-frequency (UGF) and slew rate (SR). In the IMU system, the circuit operates under clock of 1.4 MHz. The UGF higher than 10MHz and SR larger than 10 V/μs is enough. Figure 4-9 shows the schematic of the op-amp. It is a P-type input folded cascade two stage op-amp with rail-to-rail output capability. It is composed of bias stage, folded input first stage, common mode feedback block (CMFB), the frequency compensation circuit and the output stage. It is simulated with HSPICE to have a gain of 110 dB and UGF of 20 MHz with load of 30pF. The slew rate is 14 V/μs (positive)~17 V/μs (negative).

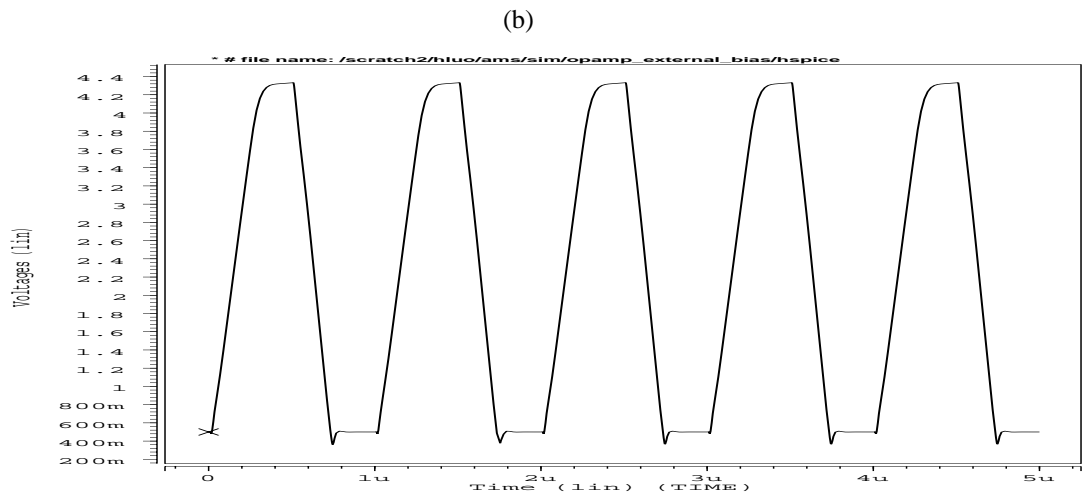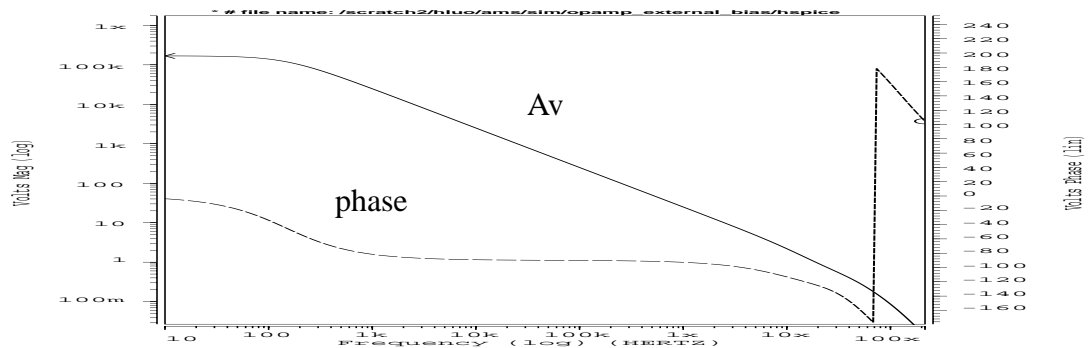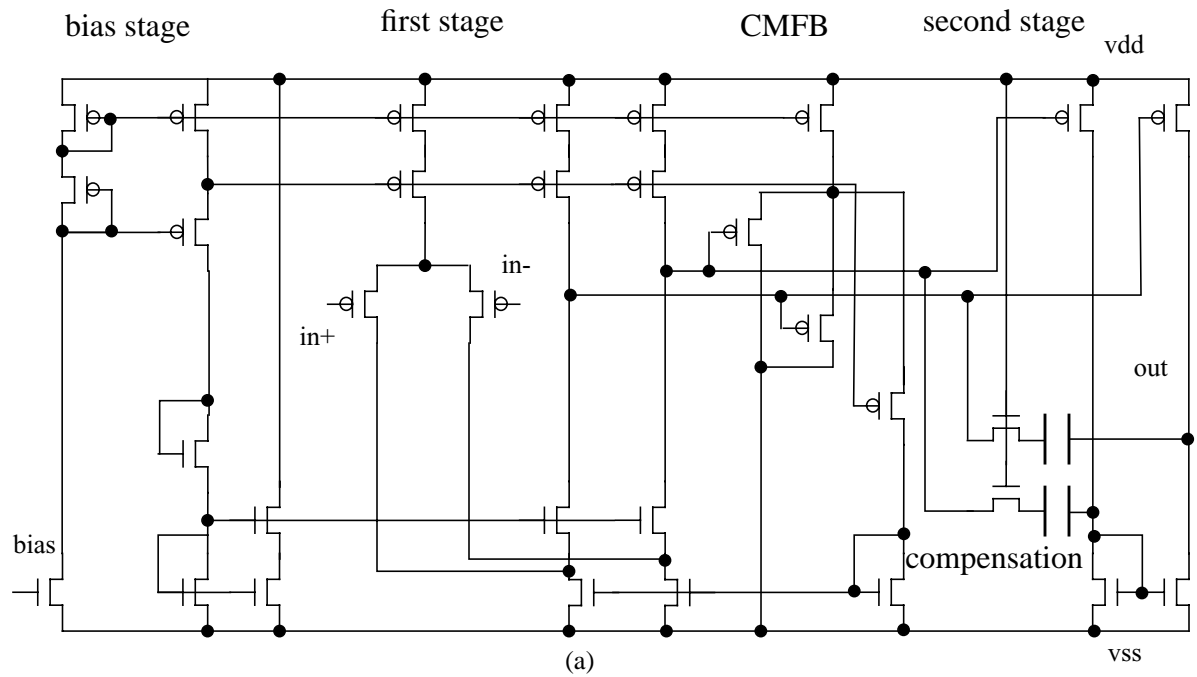bias stage   first stage   CMFB   second stage

in-

in+

bias

out

compensation

(a)

* # file name: /scratch2/hluo/ams/sim/opamp_external_bias/hspice

Av

phase

Frequency (log) (HERTZ)

Volts Mag (Log)

Volts Phase (lin)

(b)

* # file name: /scratch2/hluo/ams/sim/opamp_external_bias/hspice

Voltages (lin)

Time (lin) (TIME)

(c)

Figure 4-9. (a) Op-amp schematic. (b) Op-amp AC analyses. (c) Large signal transient analysis

4. 5 Gyroscope driving mode vibration sensing buffer

A sensing buffer is required to sense the vibration of the outer frame of gyroscope (Figure 4-1 b). The sensed driving mode signal is amplified by an off-chip high voltage amplifier and fed back to the driving actuator comb fingers. Because the driving mode is a high Q system (close to 100), the feedback loop can easily build up oscillation at the driving mode resonant frequency and it tracks any drift of the resonant frequency, e.g., temperature drift. This technique eliminates the mismatch of the external driving signal and the driving mode resonant frequency. Since the outer frame has very large vibration amplitude (several microns), the vibration signal is very strong. Thus the sensing buffer does not need gain to boost the signal amplitude. It is composed of a unity-gain buffer and an output stage. The input is also biased by a small transistor. Once the oscillation has been built up, the signal at the output has an amplitude of several hundred milli-volts.

The oscillation loop is shown in Figure 4-10. Due to the CMOS foundry process limit (5 V process), the high voltage amplifier can not be integrated into the same chip. An off-chip 15 V op-amp driver is used to drive the outer oscillation frame with 15 V DC bias on rotor (or on-chip circuit driver and higher DC bias voltage on rotor fingers, e.g., 5 V on-chip driver with 30 V DC bias on rotor). Note that the on-chip sensing buffer works at 5 V while the off-chip high voltage amplifier works under 15 V, a coupling capacitor must be put between these two stages. There is another benefit for the output DC de-coupling capacitor. It enables use of the power supply for DC bias on the rotor fingers (power supply DC plus AC, *Force*$\propto V_{dc}V_{ac}$). After the oscillation is built up, the driver op-amp output saturates (square wave) to stabilize the oscillation amplitude.
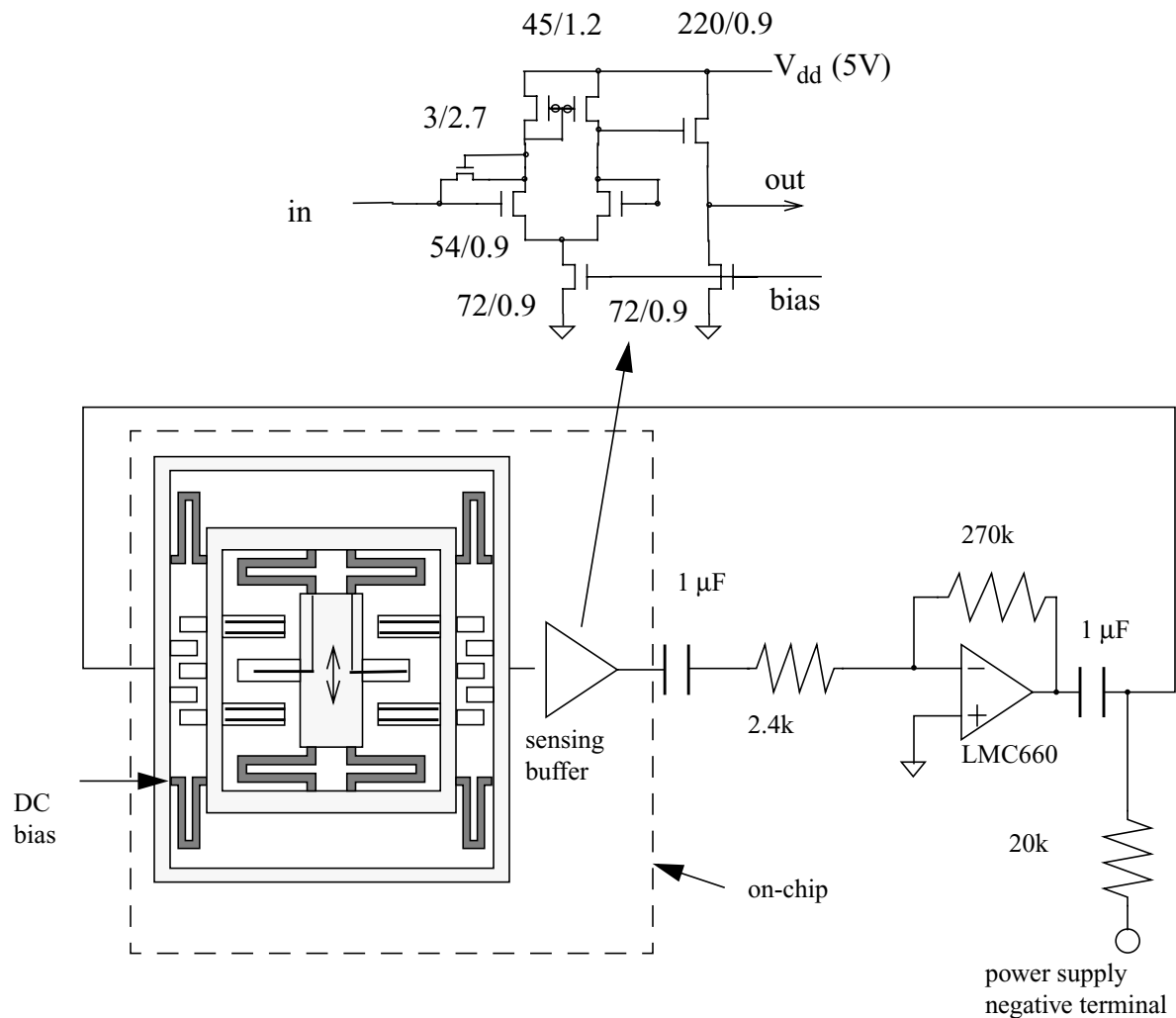
Figure 4-10. Gyroscope driving mode sensing buffer and oscillation loop.

4. 6 Frequency doubler for gyroscope

As described in section 4. 3, the main clock of the SC demodulator has twice the frequency as the sensing signals. For example, if the gyroscope oscillates at 15 kHz, this clock is required to be 30 kHz in phase. The vibration sensing signal is sinusoidal while the clock needs to be square wave, thus a waveform shaper and frequency doubler are needed. Although a phase-locked-loop (PLL) is capable of doubling the frequency, it needs an extra voltage-controlled-oscillator (VCO)

and a phase-detector (PD). A simpler circuit can complete the job using an integrator and digital logic circuitry. As shown in the Figure 4-12, the integrator shifts the input sinusoidal signal phase by 90 degree. Both the input signal and the phase shifted signal are converted into squarewave by two comparators. Then the two square waves are compared in an "xor" gate. Since these two signals are 90 degree out of phase, the "xor" gate will generate two "1" pulses in each signal cycle. Thus, compared to the input signal, the output squarewave has a doubled frequency. The input sinusoidal signal can be directly derived from the driving mode sensing signal. The integrator is composed of an op-amp and the off-chip integration capacitor. The op-amp is same as the circuit in Figure 4-9 (a). The DC feedback resistor 100k is implemented by on-chip poly resistor while the integration capacitor (1800p) has to be off-chip. The comparator schematic is shown in Figure 4-11. It is composed of Schmitt trigger with pre-amplifier. The Schmitt trigger can prevent incorrect switching at the input signal cross axis point due to noise.
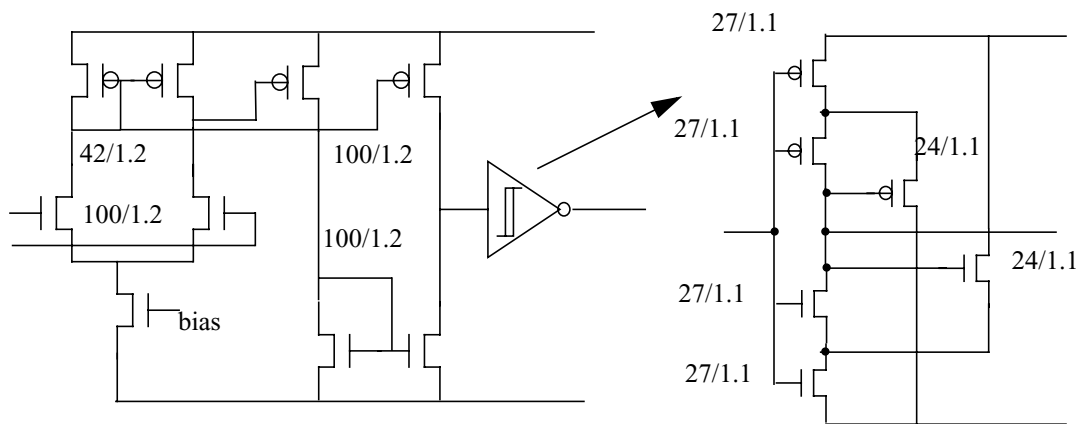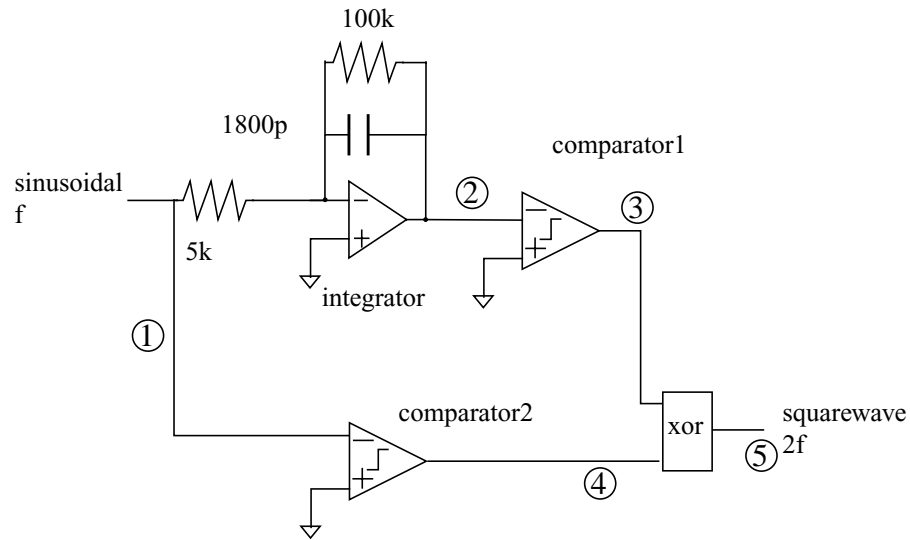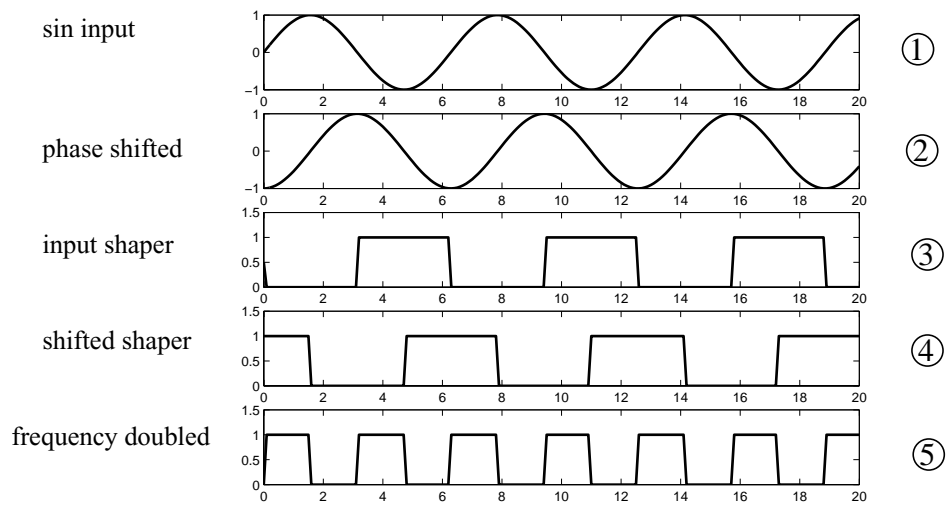

Figure 4-11. Comparator schematic.

(a)

(b)

Figure 4-12. (a) Frequency doubler. (b) Waveforms at points labeled in (a).

4. 7 Constant-g_m bias circuit

The on-chip circuits are biased internally with a constant-g_m circuit [50] shown in Figure 4-13. The transistors M1~M6 consist a current source while the Ms1, Ms2 and R2 is the start-up. The output bias current is mirrored by M7 and M8. The current is given by (E 4-4)

$$I_{bias} = \frac{(1 - \sqrt{k_2/k_1})^2}{k_2} \cdot \frac{1}{R_s^2} \tag{E 4-4}$$

where $k_i = \mu C_{ox} (W_i / L_i) / 2$.

As can be seen, this current is insensitive to the power supply voltage. Thus by using a small value resistor (Rs), an equivalent very large impedance (current source) can be achieved, which is simulated and shown in Figure 4-13. All the resistors are implemented on-chip, but it is convenient to adjust the current by reserving one pad connected to the Rs.

4. 8 Some other simple circuits used in system

There are also some basic circuit blocks for the proper function of whole system and they are briefly described below.

4-8-1 Input protection

Since the chips will be fabricated in CMOS process, the gate of each transistor that can be accessed by external pad needs to be protected. The protection circuit consists of diodes (40μm×15μm) and resistor (200 Ohm). These two protecting diodes are reverse biased to the chip power supply terminal and the current limit resistor is implemented with polysilicon.
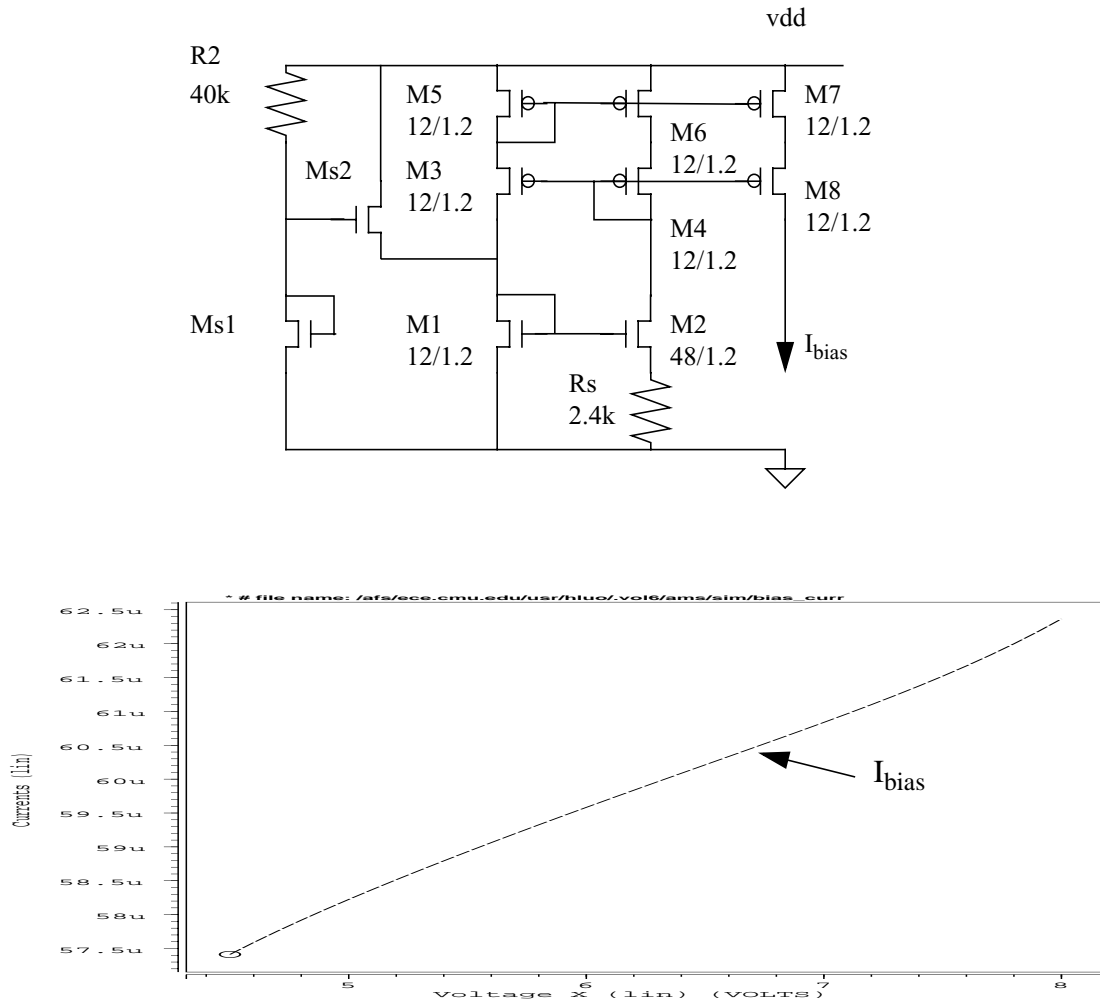
Figure 4-13.   (a) On-chip bias circuit. (b) I bias vs. power supply voltage.
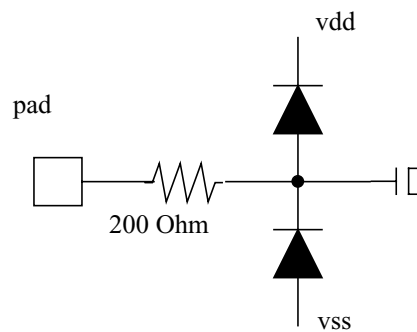

Figure 4-14. Input protection diodes.

4-8-2 Clock generator

The main clock in the system is generated by an on-chip Schmitt trigger oscillator (Figure 4-15). There is no specific requirement for the clock frequency. But the bandwidth of the sensing pre-amplifier (~4 MHz) should be at least 2~3 times higher than the modulation clock. Too low frequency introduces more flick noise and takes too large area in the layout, thus 1.4MHz is chosen as the clock frequency.
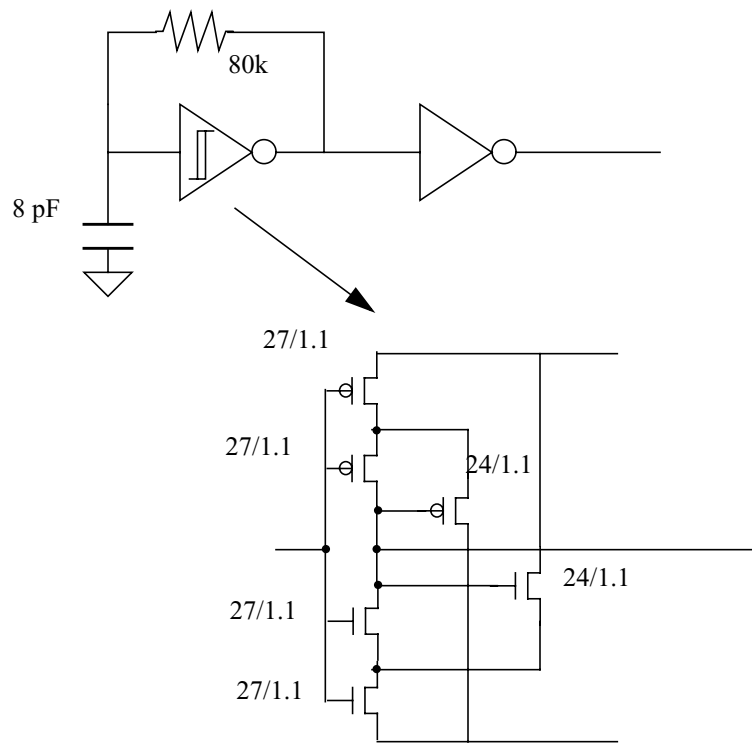
Figure 4-15. Schmitt oscillator.

Chapter 5

System Compensation

Integrated multiple device IMU system (Figure 5-1) has multiple degree-of-freedom acceleration and rotation sensing abilities. Multiple sensor outputs can be used to compensate each other, e.g. by using digital processor, to improve the system performance. This chapter will present some methods using multiple devices to improve the system performance.

5. 1 Strategy of compensation for unwanted sensitivities

Sensors often have unwanted sensitivities to many excitations, such as cross-axis sensing and temperature drift. Some of them can be canceled at the device level while others are easier to be improved at system level. There are also some dummy outputs which can not be distinguished
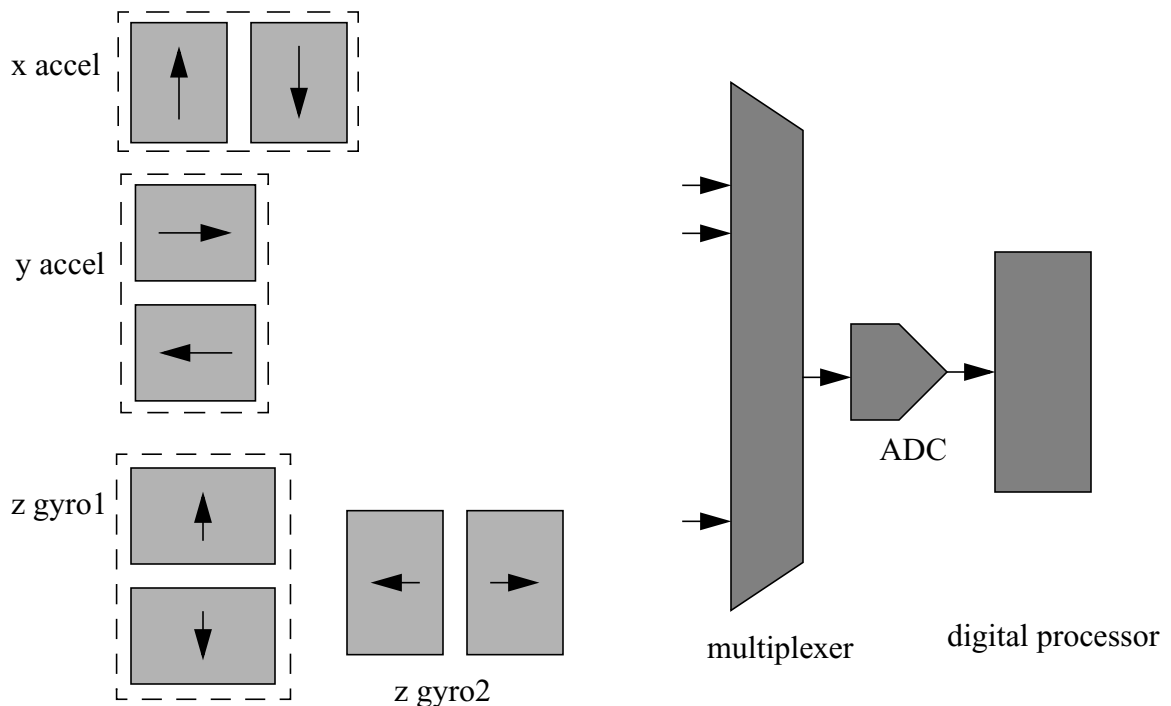
Figure 5-1. Block diagram of integrated IMU system

from the real signals, such as the offset. The strategy to compensate these unwanted signals will be discussed below.

- Common mode noise. This category includes the substrate coupling and power-supply coupling. Taking the advantage of multi-layer routing, common-centroid layout (Figure 5-2) splits the sensor into four parts and the cross-axis arrangement rejects the common mode noise.
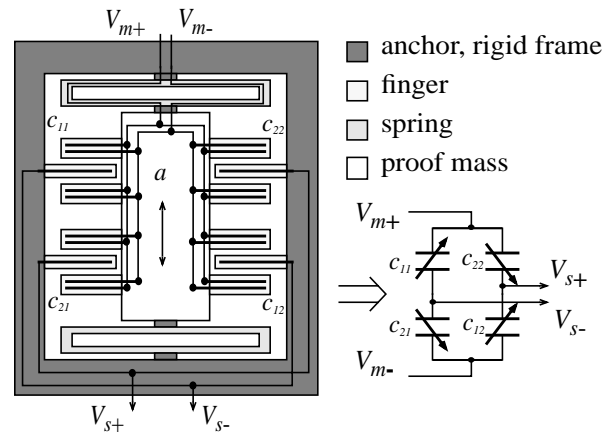

Figure 5-2. Common-centroid topology

- Cross-axis acceleration.

  Cross-axis acceleration can not be avoided in the real world. Thus high aspect ratio structures are preferred to lower the cross-axis sensitivities.

- Temperature drift.

  Due to different coefficient of thermal expansion (CTE), CMOS microstructure curling is sensitive to temperature variation. It may cause resonant frequency drift or sensitivity variation. To improve the device stability, one can incorporate a polysilicon microheater into CMOS structure [38] to keep the device at a constant temperature.

- Offset

Offset comes from many sources such as process variation or mismatch. A device with offset will show a constant output even without any physical excitation. It is not possible to distinguish the offset from the applied constant input. Common-centroid layout can decrease the mismatch due to processing gradients, but extra steps are often needed. Normally, factory calibration is the only choice. It is done by adjusting a digital trim cell or the voltage applied to the compensating actuator.

- Mixed misaligned acceleration and rotation interference.

This issue is more difficult to solve than the other problems discussed above. The presence of other inertial force, for example - a static gravitational field, may cause the device to have indistinguishable multi-axis sensitivities. The system is modeled as a sensitivity matrix (E 5-1) in which each line corresponds to a sensor.

$$
\underbrace{\begin{bmatrix} O_1 \\ O_2 \\ \dots \\ O_n \end{bmatrix}}_{output} = \underbrace{\begin{bmatrix} S_{11} & S_{12} & \dots & \dots \\ S_{21} & S_{22} & \dots & \dots \\ \dots & \dots & \dots & \dots \\ \dots & \dots & \dots & S_{nn} \end{bmatrix}}_{sensitivity} \underbrace{\begin{bmatrix} v_1 \\ v_2 \\ \dots \\ v_n \end{bmatrix}}_{input} \qquad \text{(E 5-1)}
$$

An ideal IMU system satisfies the criteria that all the non-diagonal elements are zero($s_{ij} = 0 \quad i \neq j$). In practice, those cross sensing elements (non-diagonal) should be kept as small as possible, otherwise system shows a poor singularity. The system singularity relies on the sensors' ability to reject the non-sensing axis input. And this ability is determined by the physical part aspect ratio, which is mainly limited by the release process as well as other issues, such as curling. Thus device level and system level compensation is required. We can design a system with multiple sensors with different orientation. By the communication

between different devices, for example, a gyroscope compensated by an accelerometer, it is possible to cancel some non-diagonal terms in the sensitivity matrix.

5. 2 Multiple device compensation

5-2-1 Accelerometer compensation

As mentioned previously, a single sensor usually has nonideal multiple axis sensitivity. By collecting information from the sensor array, it is possible to cancel out the unwanted signals. The easiest way is using two identical accelerometers laid orthogonal to each other (Figure 5-4). The accelerometer 1 output is O_1 and the second accelerometer output is O_2. Assume the accelerometer has sensing axis sensitivity of k_s and cross-axis sensitivity of k_x, by subtracting k_x/k_s times of O_2 from O_1, the lateral cross-axis sensitivity can be canceled.
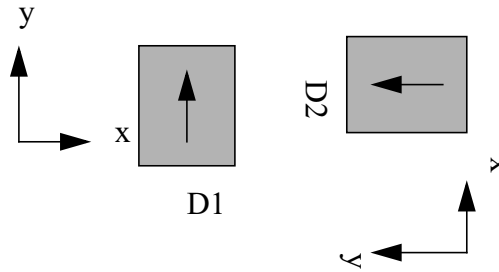
Figure 5-3. Two orthogonal identical accelerometers

Another example canceling cross axis sensitivity is given in Figure 5-4. Assume two lateral sensors D1 and D2 are identical but with 180 degree difference in orientation (Figure 5-4). Each
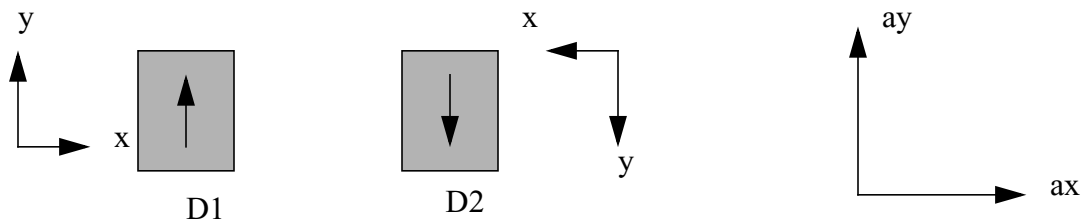
Figure 5-4. Two identical accelerometers with 180 degree orientation difference

sensor has sensitivities s1, s2 and s3 with the input acceleration ax, ay and az, respectively. The output can be written as

$$O= \begin{bmatrix} s1 & s2 & s3 \end{bmatrix} \bullet \begin{bmatrix} ax \\ ay \\ az \end{bmatrix} \tag{E 5-2}$$

Given the acceleration orientation shown as in Figure 5-4, each accelerometer has output

$$O1= \begin{bmatrix} s1 & s2 & s3 \end{bmatrix} \bullet \begin{bmatrix} ax \\ ay \\ az \end{bmatrix} \qquad O2= \begin{bmatrix} s1 & s2 & s3 \end{bmatrix} \bullet \begin{bmatrix} -ax \\ -ay \\ az \end{bmatrix} \tag{E 5-3}$$

Combining these two output, we have

$$O1-O2= \begin{bmatrix} 2s1 & 2s2 & 0 \end{bmatrix} \bullet \begin{bmatrix} ax \\ ay \\ az \end{bmatrix} \tag{E 5-4}$$

The equation (E 5-4) shows that it has decoupled the effect of Z-axis input.

Putting another same combined sensor with rotating of 90 degree (Figure 5-5), we have

$$O1*= \begin{bmatrix} s1* & s2* & 0 \end{bmatrix} \bullet \begin{bmatrix} ax \\ ay \\ az \end{bmatrix} \qquad O2*= \begin{bmatrix} s2* & s1* & 0 \end{bmatrix} \bullet \begin{bmatrix} ax \\ ay \\ az \end{bmatrix} \tag{E 5-5}$$

Assume s2*=k s1*, where k is unknown constant to be defined, then

$$p* = O1* - kO2*= \begin{bmatrix} (1-k^2)s1* & 0 & 0 \end{bmatrix} \bullet \begin{bmatrix} ax \\ ay \\ az \end{bmatrix} \tag{E 5-6}$$
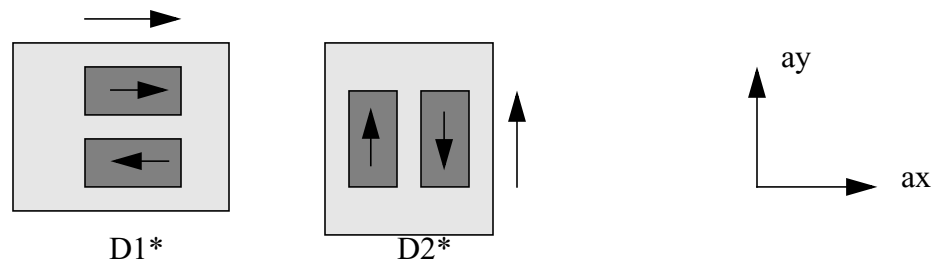

Figure 5-5. Two identical orthogonal accelerometers

As shown in the equation above ((E 5-6)), the final output $p*$ is independent with ay and az. Using the same technique we can have the output which only responds to ay.

$$q* = kO1* - O2* = \begin{bmatrix} 0 & (k^2 - 1)s1* & 0 \end{bmatrix} \bullet \begin{bmatrix} ax \\ ay \\ az \end{bmatrix} \tag{E 5-7}$$

5-2-2 Gyroscope compensation

The idea of using multiple devices to cancel out unwanted signals can also be applied to the gyroscopes.

• Accelerometer compensates gyroscope

Usually, gyroscope experiences the rotation as well as the linear acceleration, such as the centrifugal acceleration. We can put an accelerometer with the same orientation as the gyro sensing direction to sense the same acceleration, and use the accelerometer output to cancel the acceleration sensing part in the gyroscope output.
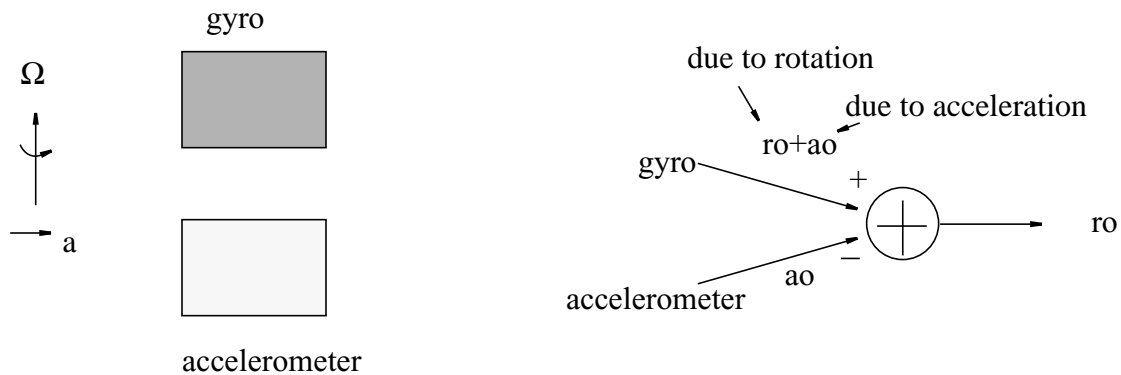
Figure 5-6. Using accelerometer to compensate gyroscope

• Two gyroscopes compensate each other

Assume two identical gyroscopes are in parallel but driven in opposite directions (Figure 5-7).

Since one of the gyroscope has opposite velocity, the output of these two gyroscopes due to
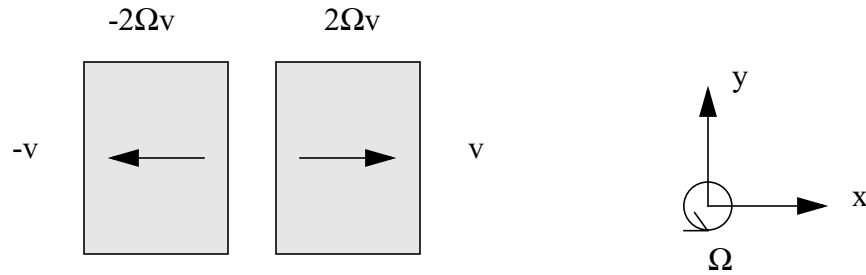
Figure 5-7. Two identical parallel gyroscopes

Coriolis force are differential while the response to other excitation remains as common mode. Thus a simple subtraction will only keep the rotation signal.

Figure 5-8 is a simulation schematic of two identical gyroscopes driven in opposite directions. Both of them experience the same rotation as well as linear acceleration at the same time. As shown in Figure 5-8, the output of each gyroscope is mixed with linear acceleration signal. The acceleration parts are common mode while the Coriolis parts are differential. The upper trace is the difference between the output of two gyroscope, and it clearly shows that the acceleration has been canceled out.

5. 3 Summary

This chapter talks about several potential techniques to compensate the non-idealities in a single device. Those methods rely on the communication between multiple devices. Thus integration of multiple devices on a single chip is an efficient way to improve the system performance.
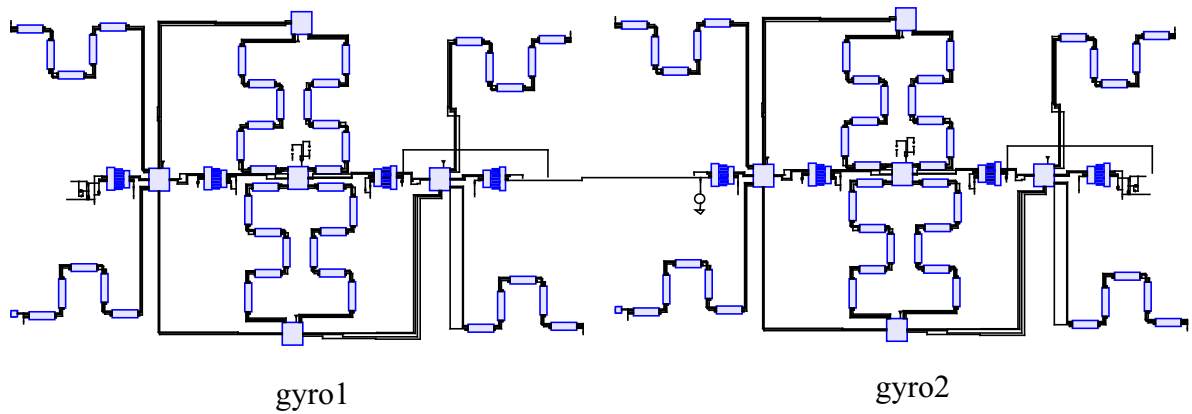
gyro1   gyro2

canceled out

with linear
acceleration

gyro1 output

gyro2 output
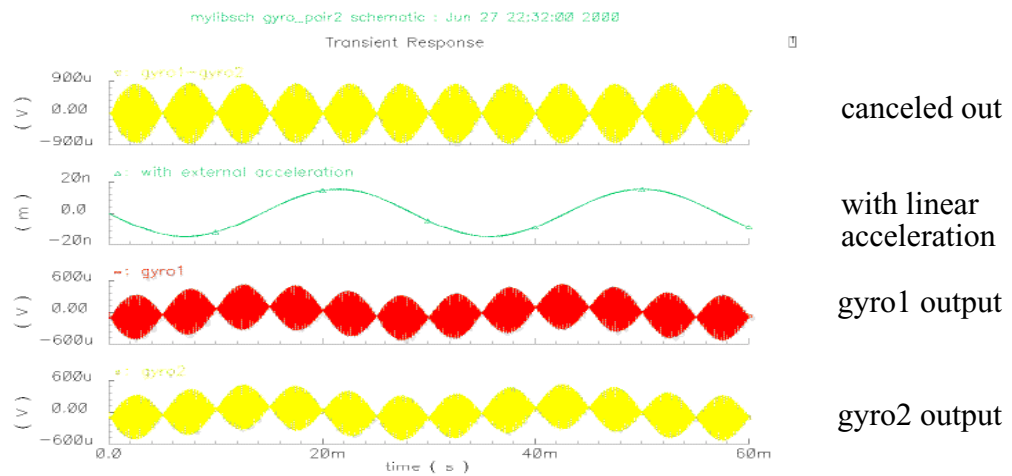
Figure 5-8. Simulation of two identical parallel gyroscopes driving in opposite
directions

Chapter 6

Measurement Results

After foundry fabrication, chips are released by an oxide RIE process in PlasmaTherm 790 chamber and a silicon DRIE process in an STS machine. Chips were bonded and tested at CMU. Note that some results in this chapter may not come from the same chip, but all of them are designed with the same methodology as described in previous chapters.

The test chip has a single +5V power supply (The gyroscope needs higher driving voltage). All the acceleration related tests are performed on the Brüel & Kjær 4808 vibration exciter, while rotation measurement are tested on the IDEAL Aerosmith 1270VS-488 rate table. Signal observing equipment includes an HP4395A spectrum analyzer and a LeCroy 9354L oscilloscope. To emulate the real application environment, if not specified, these measurements were performed under room temperature and in the open air.
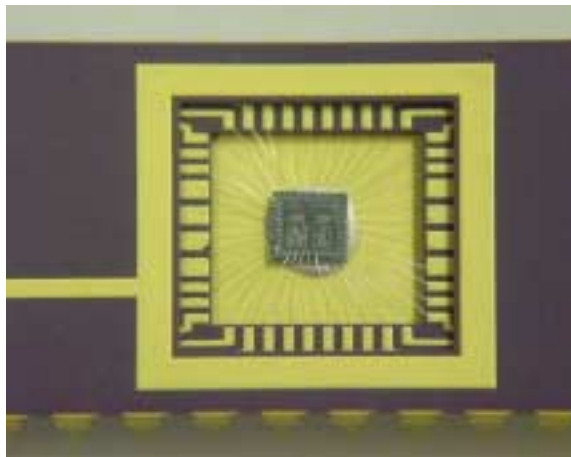
Figure 6-1. An example of bonded CMOS-MEMS chip.

6. 1 Circuits calibration

Because the IMU chip is integrated, it is impossible to measure the mid-stage signals. A dummy circuit test chip (named hh_AMS17_circuits) was designed without releasing. This chip enables the testing and calibration of each circuit block.

The bias circuit block was tested first (section 4.6). It is found the bias voltage is slightly higher (measured 1.1 V vs. simulation 0.96 V) but the output current is 64.5 uA which matches the simulation very well.

In the next test, the sensing pre-amplifier (Figure 6-2) is tested. The input terminal DC bias is found around 1.8V. The DC output offset is about 1~1.5 V corresponding to the input offset about 70 mV. This large offset is due to small transistor size and fabrication variation. The AC transfer function is shown in Figure 6-2. Note that the network analyzer and active probe has a -7.2 dB attenuation. The pre-amplifier with input coupling capacitor of 700 fF has a gain of 22.8 dB which is smaller than the simulated 28 dB. The lower frequency -3 dB corner is less than 10 Hz and the higher corner is at 3.7 MHz. The input sub-threshold transistor behaves as a high imped-ance resistor larger than 20 G Ohm. The circuit noise is measured with spectrum analyzer (with 10:1 active probe) and shown in Figure 6-3. The input referred noise is 115 nV/$\sqrt{Hz}$ at 600 kHz which is much larger than the simulated 18nV/$\sqrt{Hz}$. Even without considering the rest part of the system, we may conclude here that the system noise will be dominated by the electronic noise. As an example, if an accelerometer has a sensitivity of 1 mV/G, this electronic noise is equivalent to 115 μG/$\sqrt{Hz}$ which is larger than the normal Brownian noise around 20 μG/$\sqrt{Hz}$.
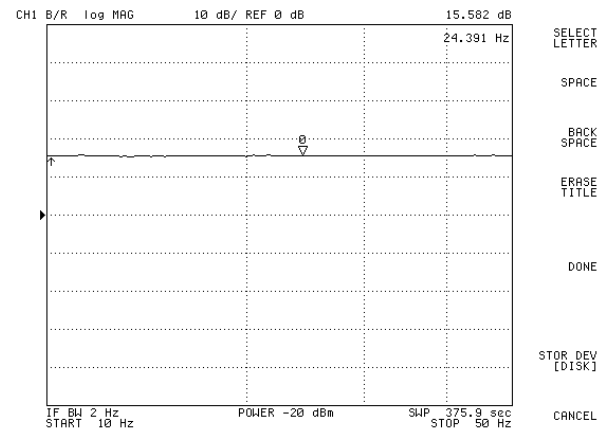
Figure 6-3 also shows the comparison of the output noise between the measured result and simulation result. The HSPICE simulation is done by using the transistor nominal model from the
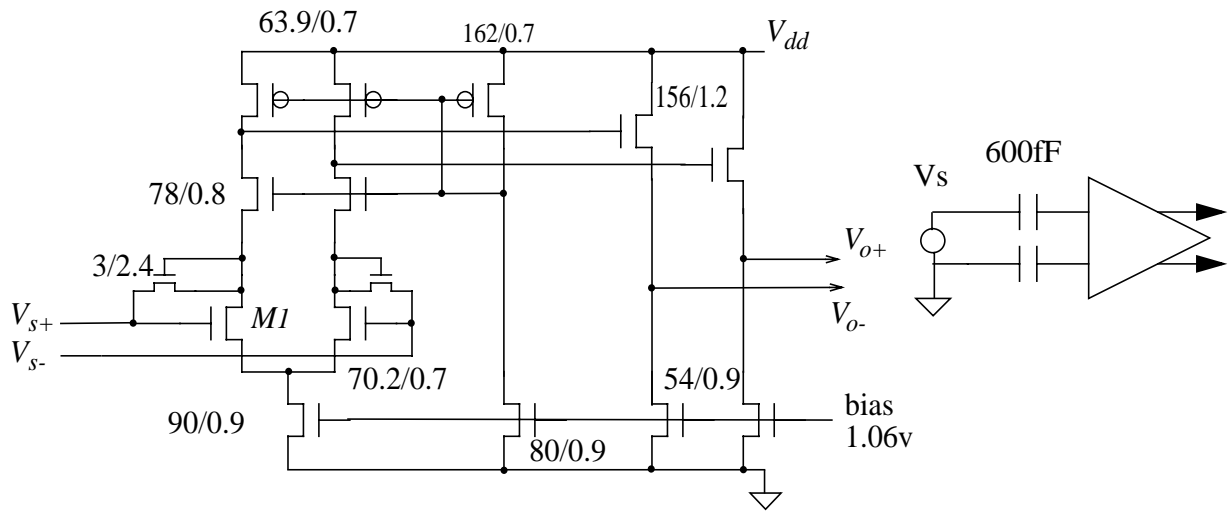
(a)
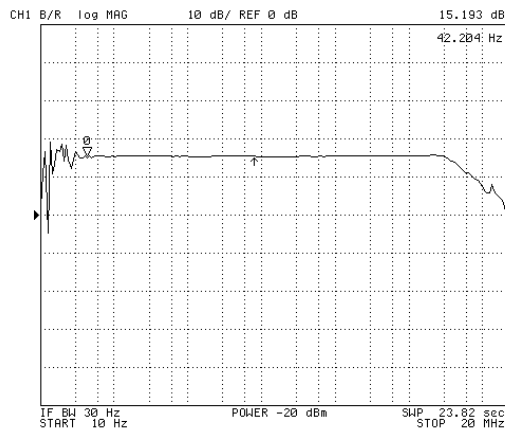
(b)

(c)

Figure 6-2. (a) Sensing pre-amplifier and AC transfer function measuring schematic.
(b) Measured AC transfer function. (c) AC transfer function in low frequency.

foundry. The spikes in the measured noise arises from the environment interference. The larger measured noise can be explained by the unexpected high flicker noise and the hot carrier noise. As can be seen from Figure 6-3 (c) the noise keeps decreasing with increasing frequency. The flicker noise corner frequency is even beyond 5 MHz. The higher slope of the noise at the very low fre-

quency (Figure 6-3 c) is due to the noise of the bias transistor being filtered by the dummy sensor

capacitor (remember the very large time constant at the input terminal). The hot carrier noise is

another reason for the higher measured noise. In the simulation the simulator assumes transistors

have a thermal noise of $8/3kT/g_m$, which is based on the long channel transistor model. Indeed the

thermal noise of MOS transistors is $4kT\Upsilon/g_m$[43]. The parameter Υ has a value of unity at zero

V_{DS} and, in long devices, decreases towards a value of 2/3 in saturation. In short channel devices,

e.g., half micron in this case, the Υ is typically 2~3, but can be considerably larger [44] .

(a)

(b)

(c)

(d)
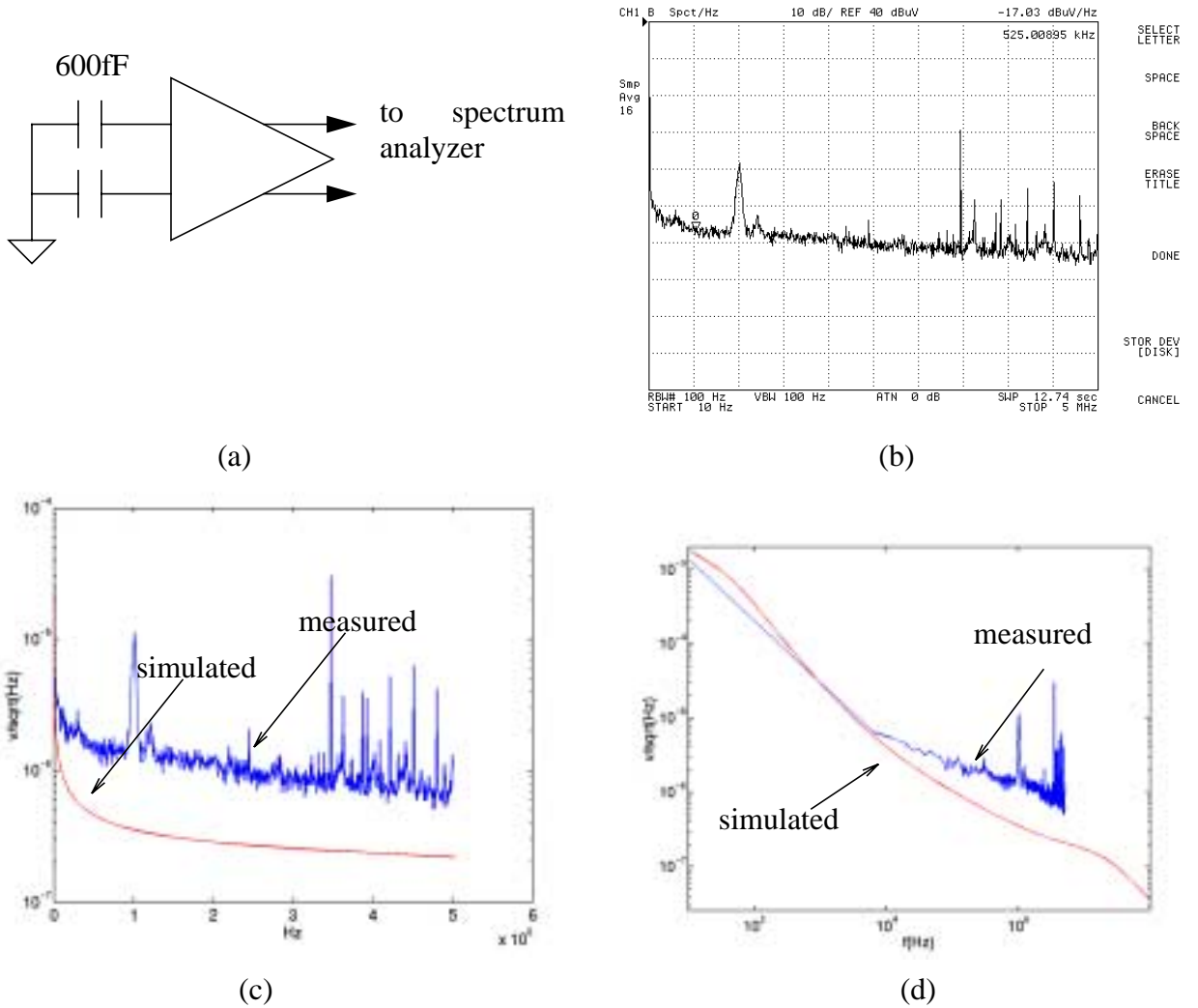
Figure 6-3. (a) Output noise measuring schematic. (b) Sensing pre-amplifier output noise. (c) Comparison with simulation. (d) Comparison in Log-Log scale

Hao Luo

The unit gain frequency (UGF) of the op_amp used in the switched-capacitor demodulator is found at 15.6MHz. The positive slew rate is 12 V/µs and the negative slew rate is 15 V/µs. Its noise is also measured (720 nV/$\sqrt{Hz}$ @ 20kHz)and is shown in Figure 6-4.
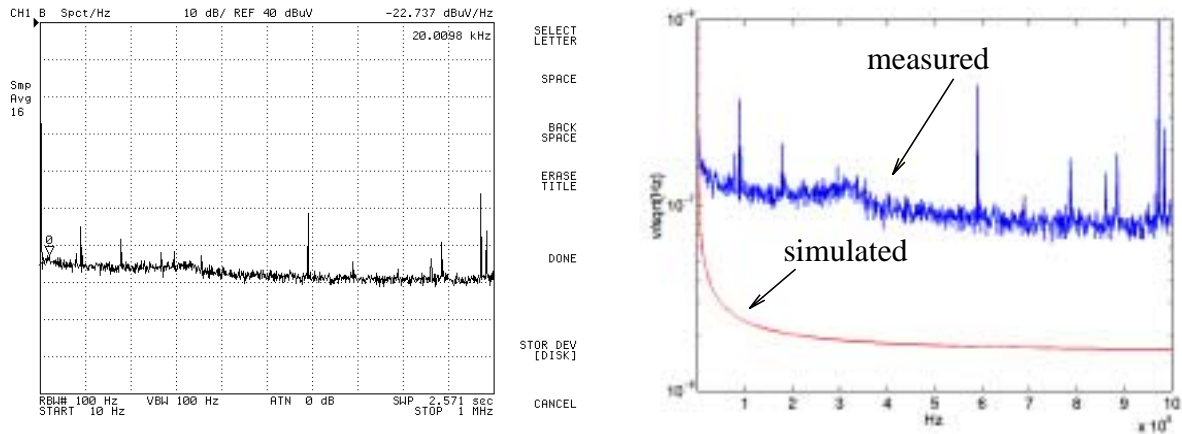

Figure 6-4. Op_amp output noise and comparison with simulation.

The tested switched-capacitor demodulator works under the on-chip clock of 1.38 MHz. It has a demodulation gain of 16. Its output noise is shown in Figure 6-5. The input referred noise is 220 nV/$\sqrt{Hz}$ at 2 kHz.

Figure 6-6 shows the total output noise of connected pre-amplifier and mixer. The total input referred noise is 126 nV/$\sqrt{Hz}$ at 2 kHz.

The unit-gain buffer for gyroscope oscillation sensing is also tested (Figure 6-7). It has a gain of 0.72 and input referred noise 300nV/$\sqrt{Hz}$ at 2MHz.
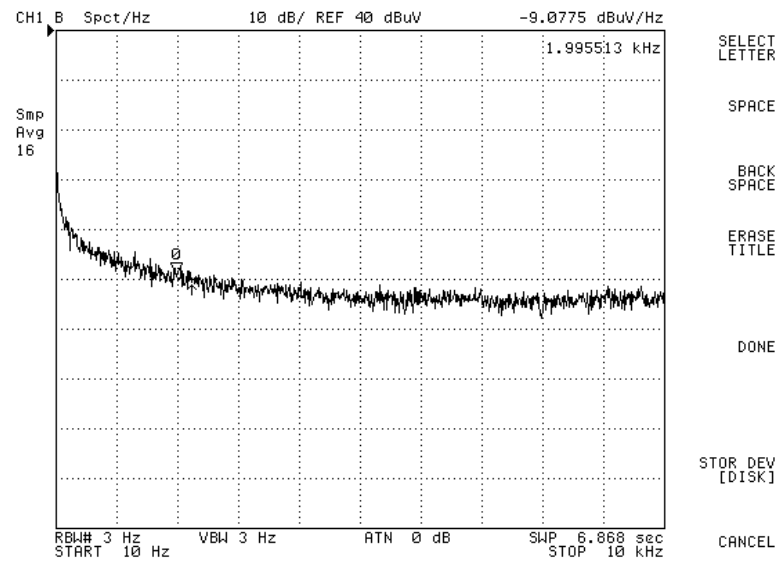
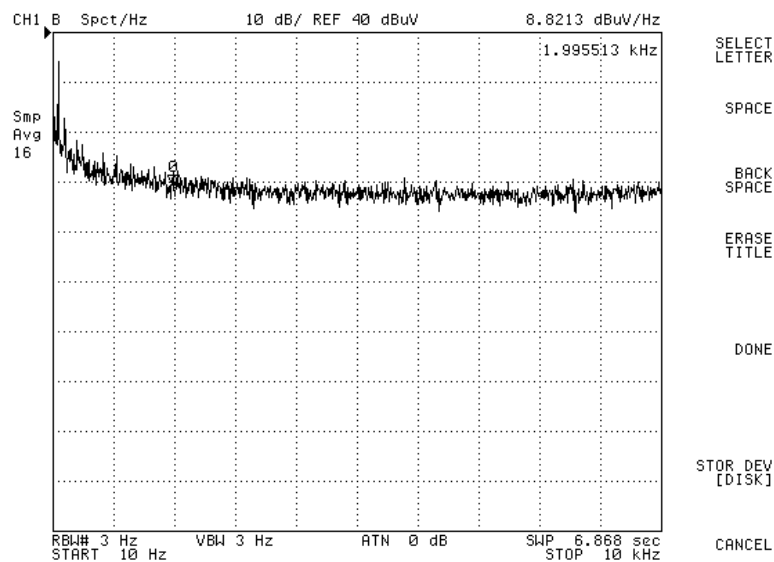Figure 6-5. Switched-capacitor mixer output noise.

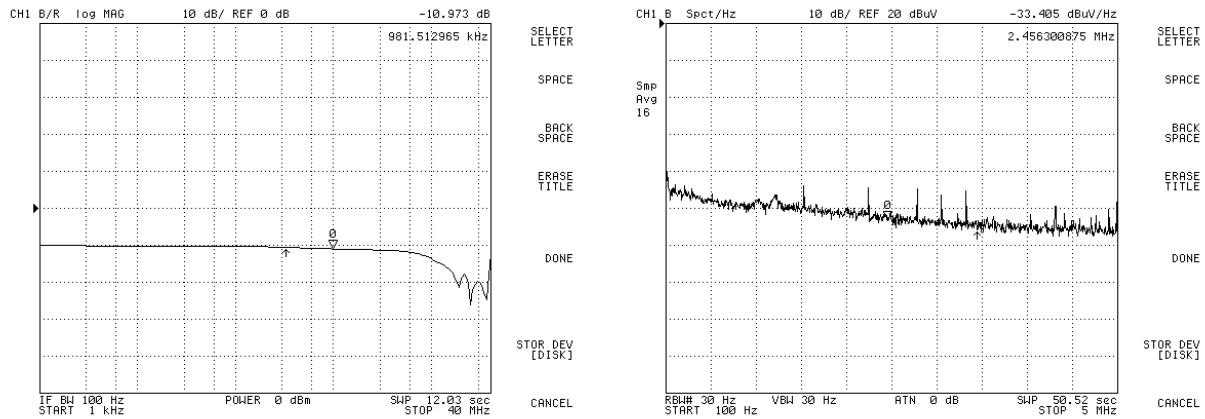Figure 6-6. Total output noise of connected pre-amplifier and mixer.

Figure 6-7. Unit-gain buffer AC transfer function and output noise.

6. 2 Individual device test

6-2-1 Accelerometer curl measurement

In a chip fabricated in Agilent 0.5 μm CMOS process (named actuators52a), a lateral acceler-ometer curl was measured by Wyco NT3300 optical profilemeter and shown in Figure 2-5. The maximum out-of-plane curl is 6 μm while the mismatch between the rotor and stator fingers is reduced to 0.3 μm.

Another similar accelerometer fabricated in AMS 0.6 μm CMOS process (named hh_AMS7) suffers severe curling problem (Figure 6-8). As can be seen, at the middle part of the structure, fingers are almost completely mismatched each other by 5 μm. The difference between these two processes is because the AMS material has much higher residual stress, which makes the curl matching technique can not work quite well for the AMS structure. The severe mismatch causes great loss of the capacitance for sensing. Thus in the later design and test, this structure has been abandoned and replaced by the inner accelerometer of gyroscope structure (will be discussed in 6-2-3).
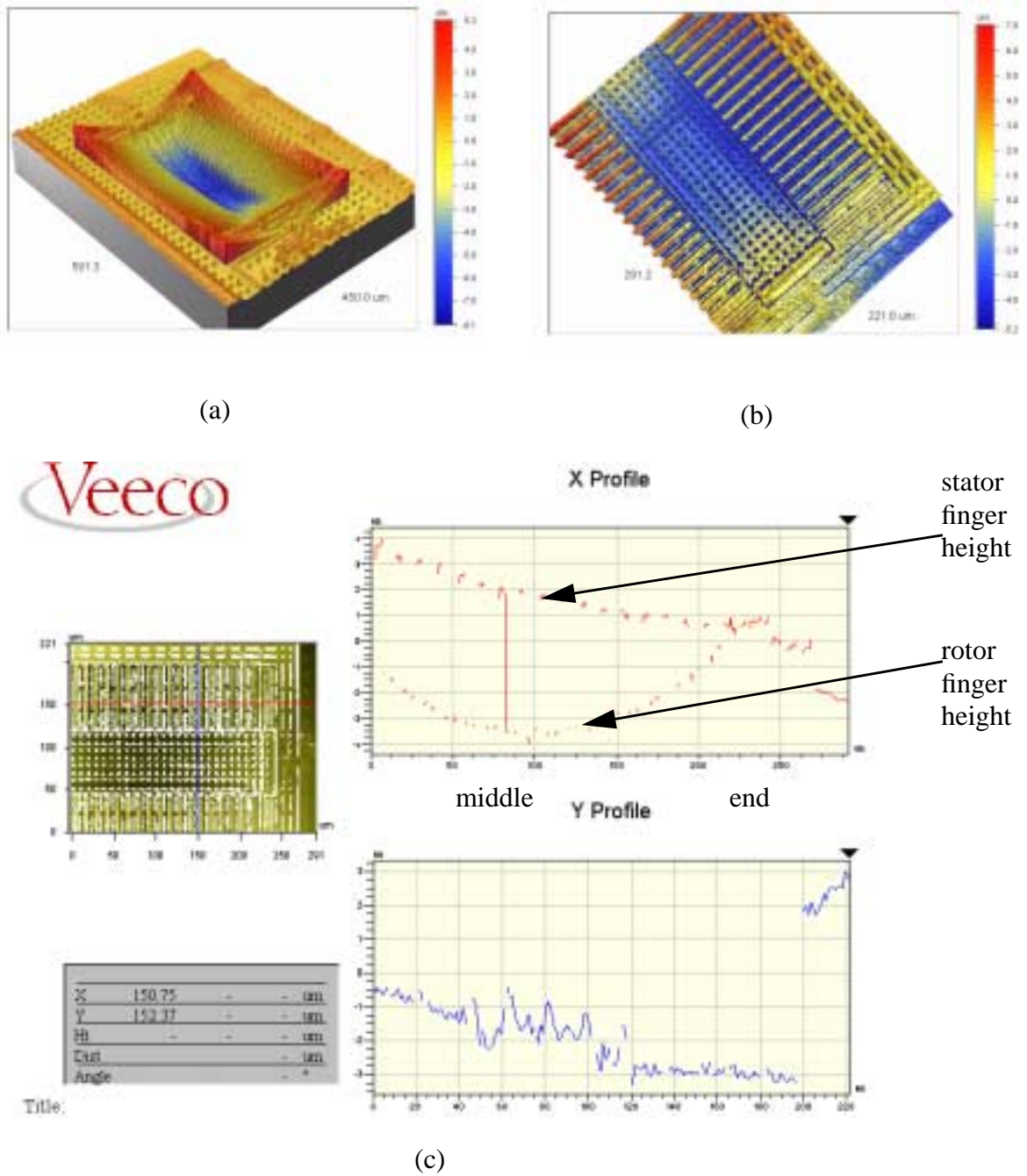
(a)

(b)

(c)

Figure 6-8. AMS accelerometer curl measurement result. (a) and (b) 3-D images of curl. (c) Measurement of the finger curl mismatch.

6-2-2 AMS Lateral accelerometer test

In the resonant frequency test of the AMS accelerometer (named hh_AMS9), a driving voltage of 18 V_{dc} plus 3 V_{ac} was applied to the self-test actuator finger on the accelerometer and the motion was measured with the MIT Microvision™ system. Figure 6-9 shows the measured displacement versus frequency. The measured resonant frequency is $2\pi18$ kHz. The higher resonant frequency than the Agilent accelerometer is due to the smaller structure and higher Young's modulus in the AMS process.
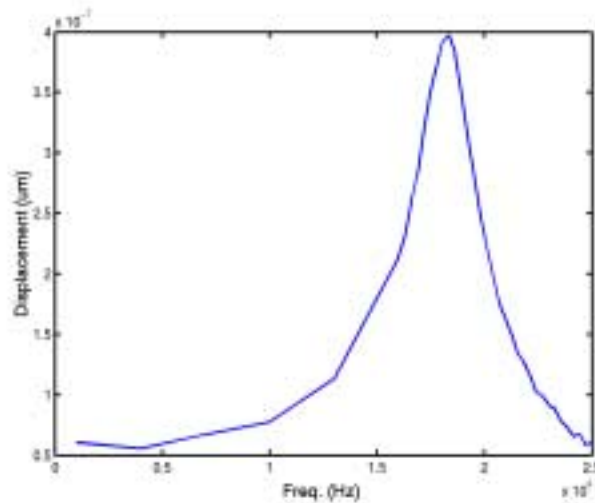
Figure 6-9. Displacement vs. frequency during self-test.

After successful release, the accelerometer chip was bonded on a 40-DIP package and put on a test board. Since the accelerometer is fully integrated, only several passive components were needed on the board (Figure 6-10).

In the dynamic test, the accelerometer was excited by a 100 Hz 1 G (p-p) sinusoidal acceleration on a Brüel and Kjær vibration table. The waveforms of the output from a reference accelerometer and the output from the CMOS-MEMS accelerometer are compared in Figure 6-11 (a).
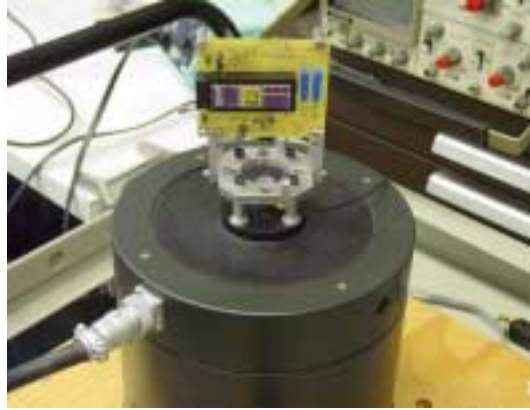
Figure 6-10. AMS accelerometer test board on vibration table.
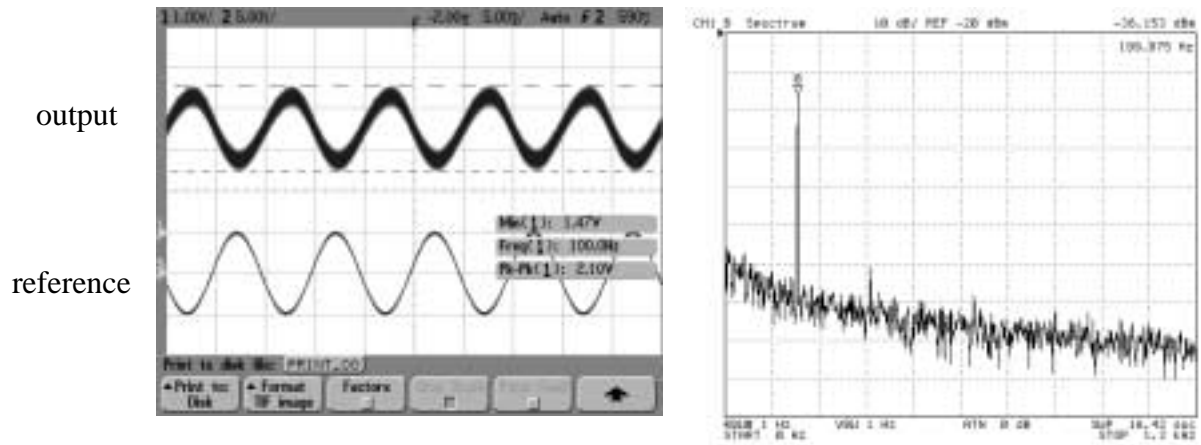

output

reference

Figure 6-11. Accelerometer dynamic test (a) Waveform of output (1G 100Hz acceleration), (b) Spectrum of output (1G 200Hz).

Figure 6-11 (b) shows the spectrum of the output from the accelerometer when excited by an 1 G acceleration at 200 Hz. As can be seen, this accelerometer has good linearity. The second order harmonic is attenuated by nearly 50dB, and the third or higher order harmonics are even smaller. The measured noise floor was 3 mG/$\sqrt{Hz}$, which is much larger than predicted (less than 100 µG/ $\sqrt{Hz}$ was predicted). When the test system was placed on an air table to isolate any test bench vibration, no decrease in the noise was found. In the next test, the accelerometer was put in a vac-

uum chamber to see the relationship between pressure and noise. Again, the noise did not decrease at low pressure. Thus we concluded that the electronic noise dominates the system noise performance.

6-2-3 Gyroscope curl measurement

Figure 6-12 shows the curl measurement result of the released AMS gyroscope structure (named hh_AMS9). The highest curling point is at the corner (+6.6 µm) while the lowest is at the middle of the proofmass (-1 µm). But the inner accelerometer core has very good curl matching on its rotor fingers and stator fingers (less than 0.5 µm). The outer driving finger mismatch is less than 2.5 µm. The inner accelerometer has much better matching than the sole accelerometer fabricated in the same process. This is because the accelerometer inside the gyroscope is suspended by four springs and the stress inside the structure gets better released. The measurement results implies that the inner core of the gyroscope can be just used as a good accelerometer. Actually it is used as a lateral accelerometer tested and discussed in section 6-2-2.
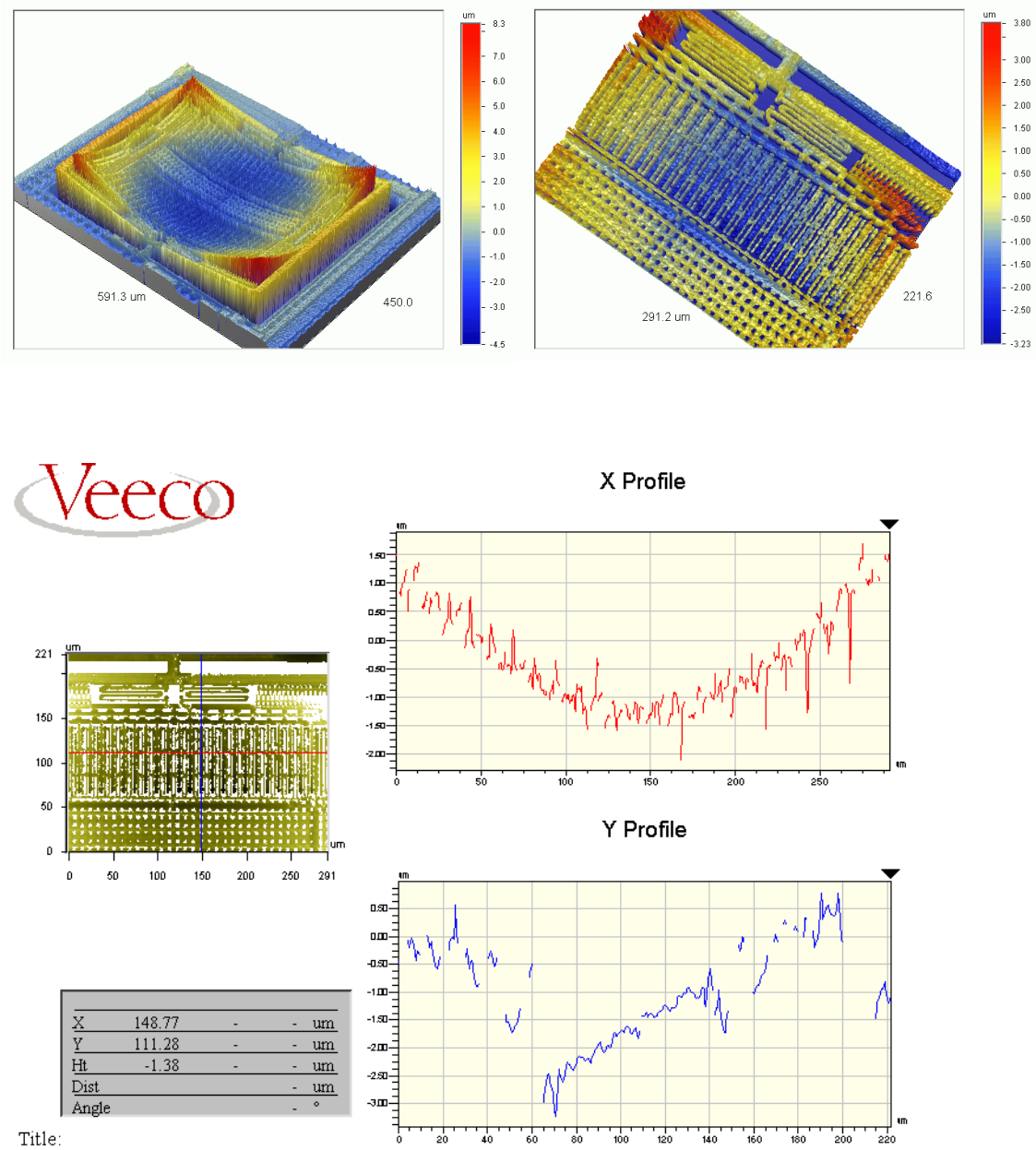
Figure 6-12. (a) Gyroscope structure curl. (b) 3-D images of the curling.
(c) Measurement of finger curl mismatch.

6-2-4 Mechanical structure vacuum Q measurement

Since the gyroscope does not depend on the mechanical Q enhancement, there is no need to tune the two mode resonant frequencies to match and thus it is not sensitive to the frequency drift. But it is still interesting and necessary to investigate the mechanical quality factor behavior. By putting the chip into a vacuum chamber, the two mode resonant frequencies and their relationship with the pressure were observed. The sense mode is measured by applying AC drive signal to the self actuating fingers and measuring the output from the Coriolis sensing amplifier. The drive mode is measured by applying AC drive signal to the oscillation drive fingers and measuring the output from the oscillation sensing buffer.

The measurement results are shown in Figure 6-14. There are several conclusions can be derived from it: a) The sense mode has very low Q=5 in the open air because of the large number of lateral comb fingers and the large squeeze damping between them. Thus decreasing the pressure can significantly boost the Q till it reaches saturation around 600 at 300 mtorr. b) The Q enhancement is almost log-linear to the decreasing of the pressure at the mid-pressure range (10^{-2} torr ~ 10^1 torr). c) The drive mode has relatively high Q=51 in the open air. d) At the low pressure
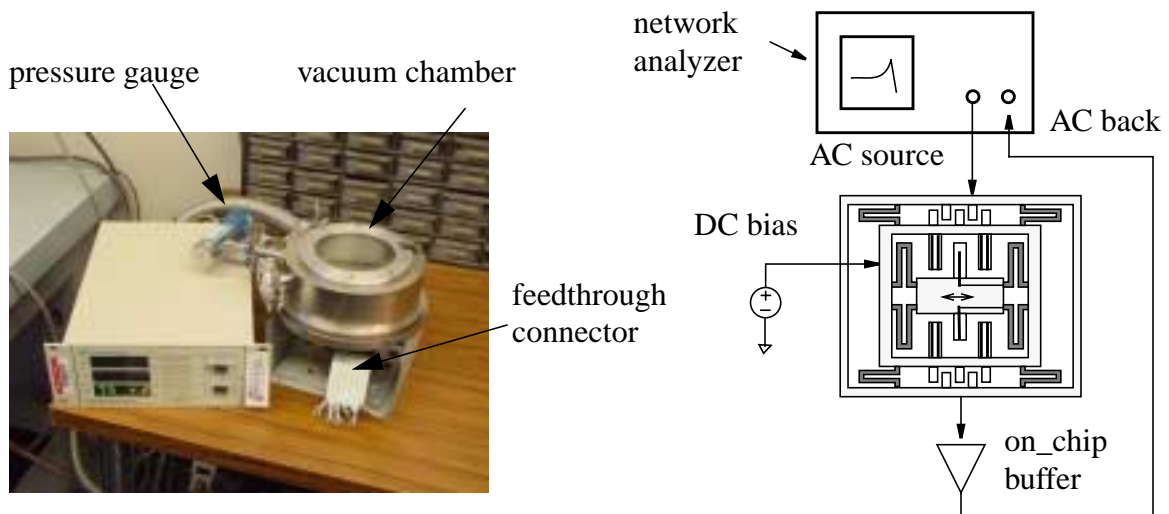

Figure 6-13. Vacuum Q test set up.

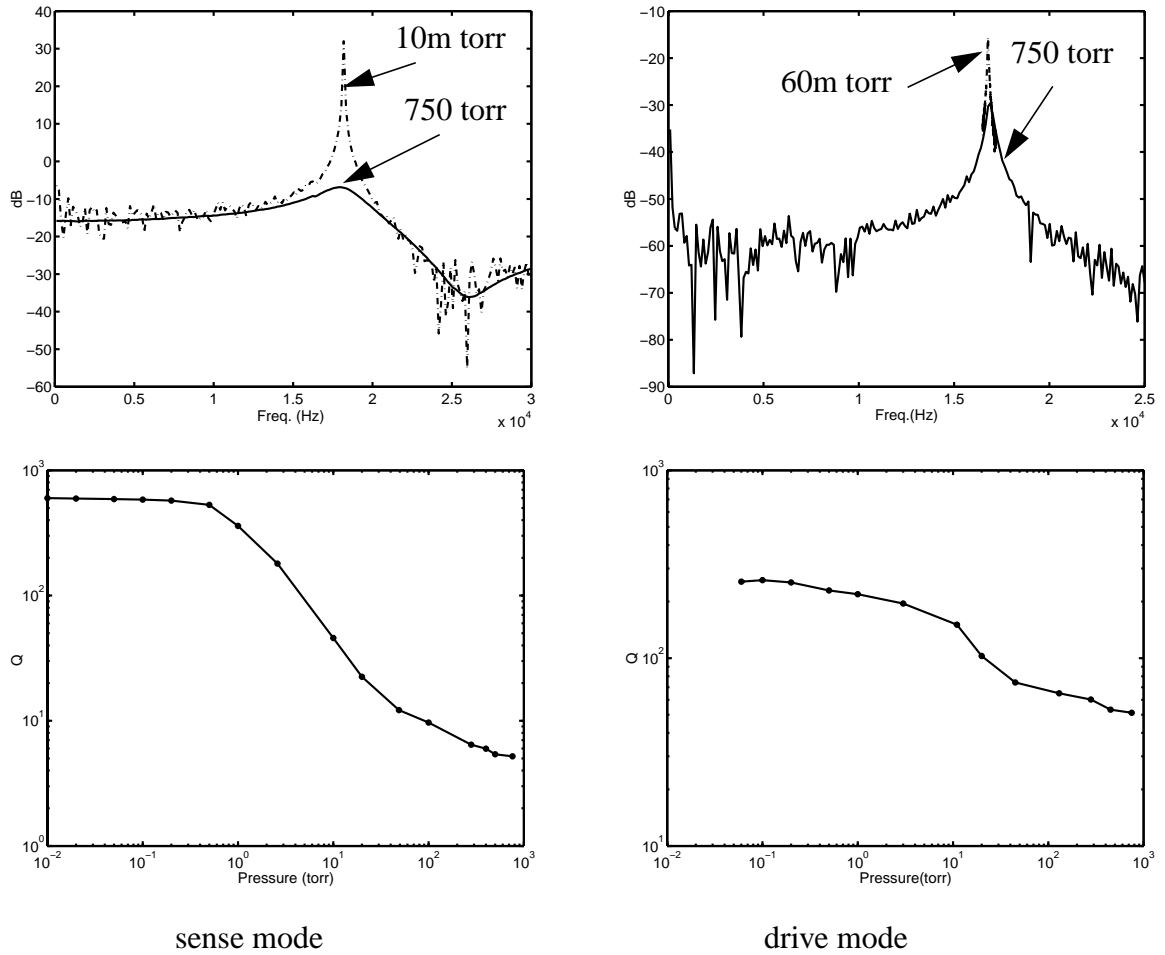sense mode   drive mode

Figure 6-14. Gyroscope mechanical resonant frequency and Q vs. pressure.

(under 10^{-1} torr), the drive mode has lower Q than the sense mode. This is because the drive mode has larger and more complicated structure, especially the inner part is not a rigid body, which causes more energy loss during vibration. That loss makes it has less Q in the vacuum.

6-2-5 Z-axis gyroscope mechanical stability test

The circuit used for gyroscope (named hh_AMS11) test is shown in Figure 6-15. The high voltage driving op-amp is off-chip (LMC660). After the oscillation builds up, the op-amp gets sat-
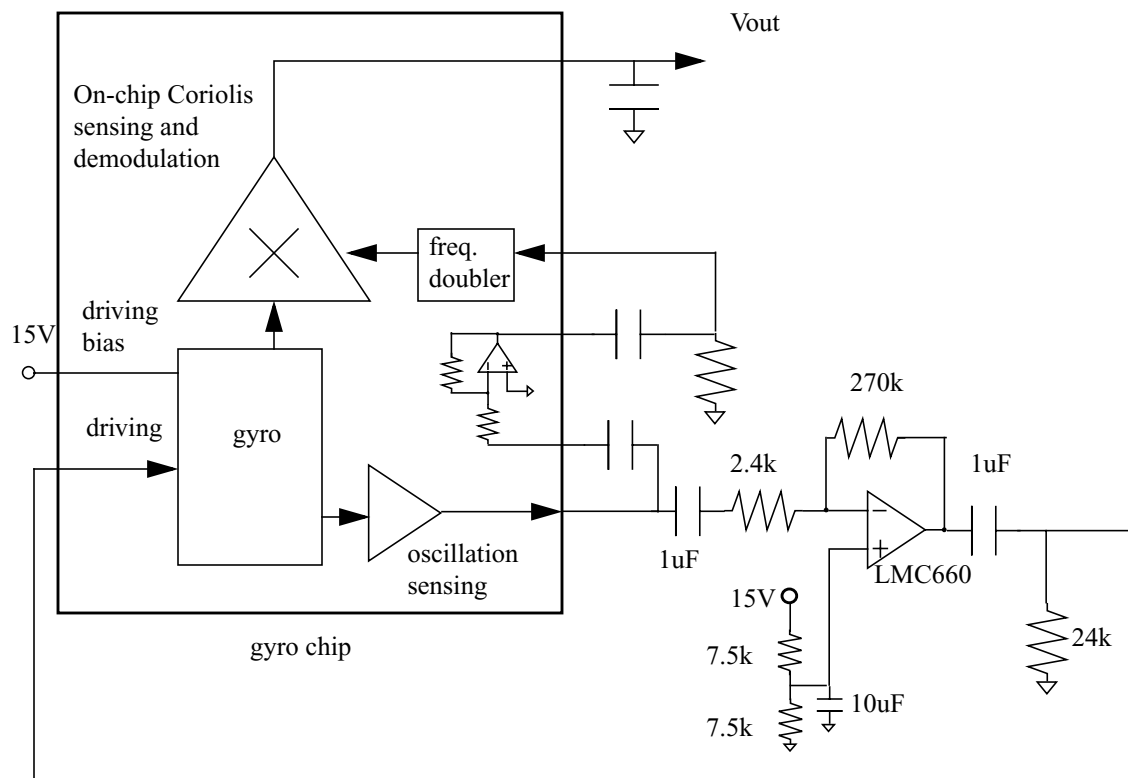
Figure 6-15. Gyroscope test board circuitry.

urated and outputs a square wave signal to drive the gyroscope. The op-amp output capacitor and

the resistor (24k) set the DC level to ground. This enables the maximum usage of the power sup-

ply for driving. The vibration amplitude is set by the saturation of the driving amplifier. For more

accurate amplitude control, an AGC can be applied (Figure 6-17). The oscillation sensing signal is

also sent to the on-chip frequency doubler to feed the demodulator (see chapter 4. 3). Figure 6-17

shows the picture of the chip and the test board.

    First, the gyroscope driving mode long term stability was tested. Three parameters were mea-

sured simultaneously during the test, chip temperature, oscillation frequency and oscillation sens-

ing amplitude. Figure 6-18 shows the continuous measurement results for 8 days. The chip

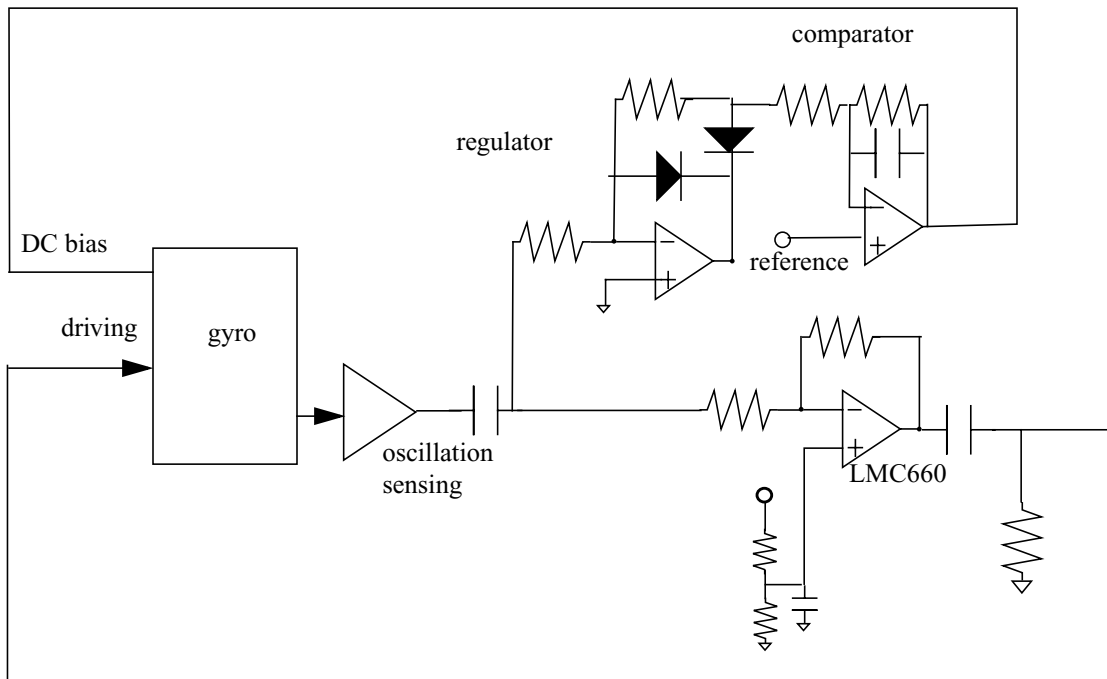temperature may vary with the environment temperature fluctuation. The frequency has a very

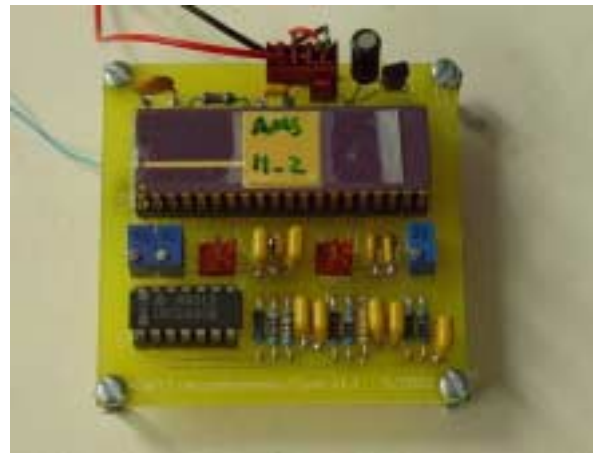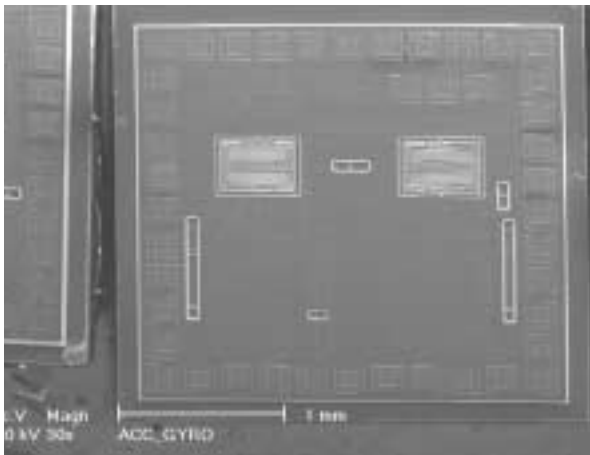Figure 6-16. Vibration amplitude control with AGC.

Figure 6-17. Gyroscope chip and test board.

small positive temperature coefficient. After one month continuous test, the structure did not show
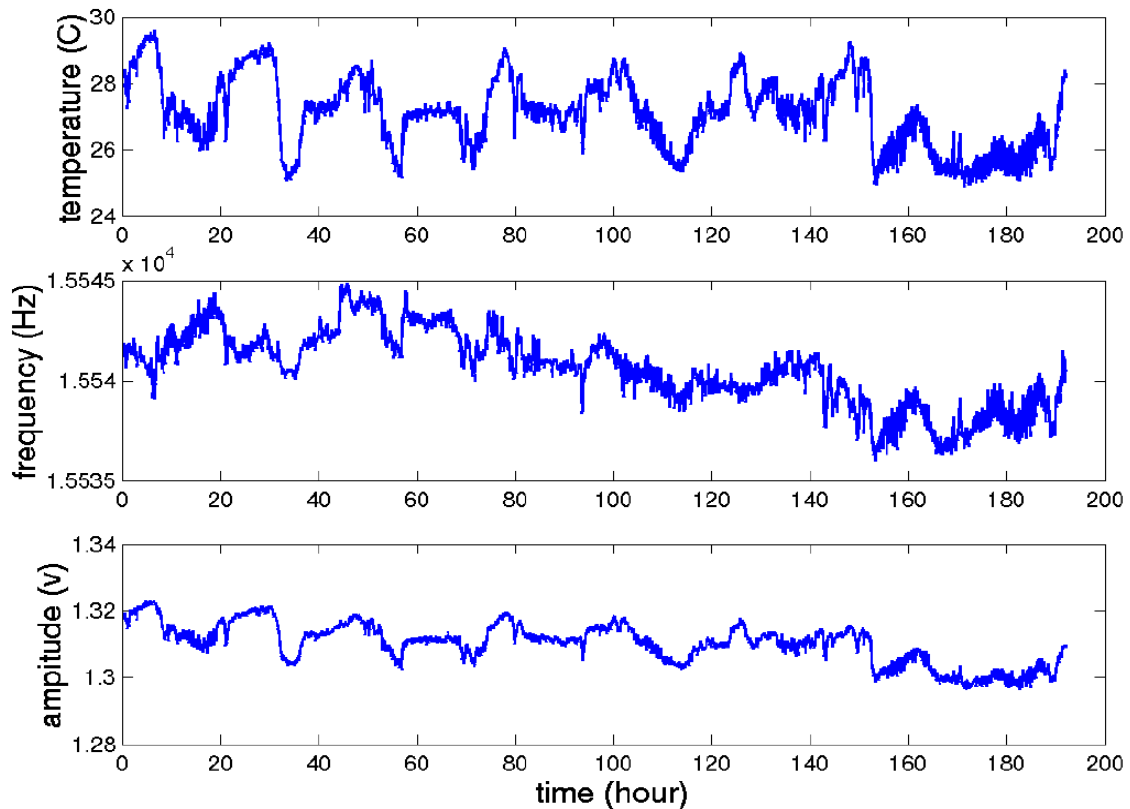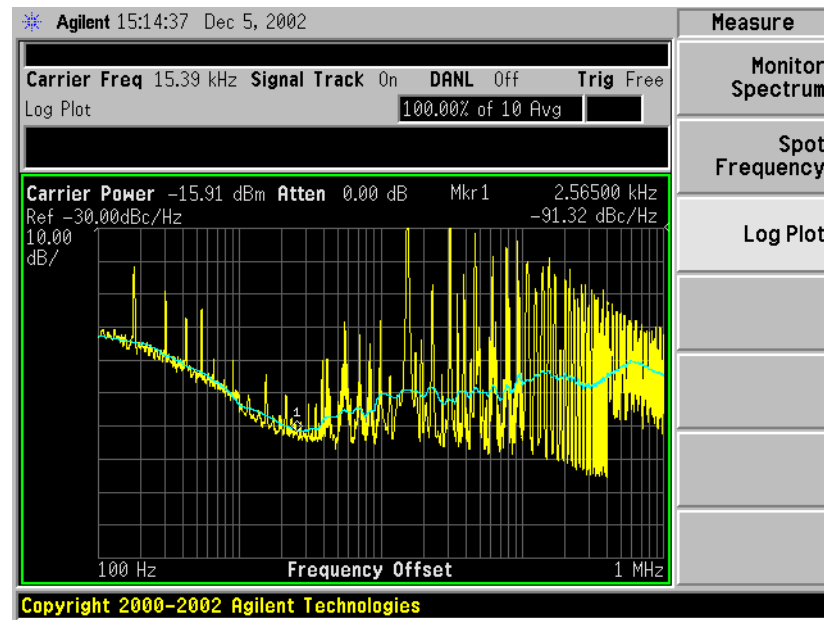
any fatigue.

Figure 6-18. Gyroscope oscillation phase noise and long term monitoring result.

6. 3 More about the circuit noise

All the previous measurement results show that the circuit noise dominates the whole system noise performance. Thus the circuit noise itself need more investigation. In the circuit the noise mainly comes from the transistor. There are two main noise models for the transistor in simulation, thermal noise and flicker noise, which can be modeled as

$$i^2/\Delta f \ = \ 4kT\Upsilon g_m + \frac{K_F I_d^{A_F}}{f C_{ox} WL} \tag{E 6-1}$$

where K_F and A_F are empirical parameters related to the fabrication process. At the low frequency (Figure 6-3) the circuit noise does show an increase when frequency decreases. But it is clear that this model is not accurate enough to describe the noise behavior. Since it is difficult to tell whether it is 1/f (flicker) noise and where the corner is, it implies that there might be some other noise terms in the noise equation (E 6-1) which is inversely proportional to the weak power of frequency. As seen from the measurement result, the noise decreases at higher frequency. Thus a test of the relation between the noise and the modulation frequency has been performed.

Figure 6-19 shows that, in a certain frequency range (lower than 2.6 MHz here), the noise floor decreases while increasing the modulation frequency. After that point, the noise floor increases sharply. At the lower frequency, increasing the modulation frequency will move more flicker noise out of band, thus the noise floor drops. But at frequencies higher than that range, the circuit bandwidth limit becomes a key role in the system performance. Since the sensing buffer gain drops quickly outside its bandwidth (Figure 4-6), as shown in the Figure 6-19, the equivalent system noise increases sharply.
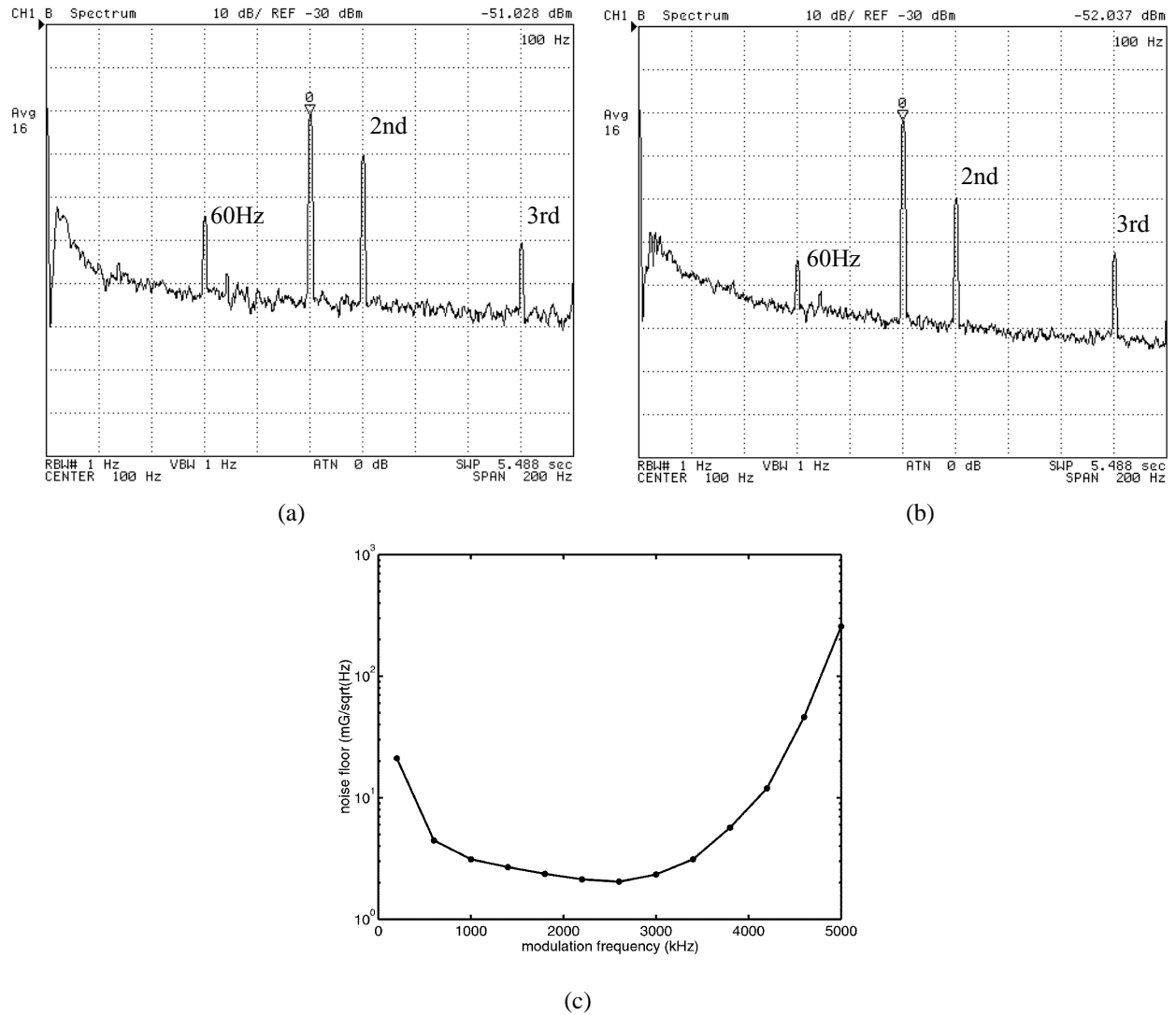
(a)

(b)

(c)

Figure 6-19. Noise performance under modulation frequency of (a) 600 kHz, (b) 2.6 MHz. (c) Noise vs. modulation frequency.

Another interesting thing is that the 60 Hz and its harmonics decreases with the noise while the signal peak does not change. The higher order harmonic have less decrease than the lower order harmonic. This proves that the 60 Hz and harmonics during the test do not come from the environment vibration, but rather come from the power supply as a common mode noise source. Because the real acceleration signal is a differential signal and its amplitude does not change with the modulation frequency, the signal peak does not change. But the 60 Hz and its harmonics are

common mode and removed by the switched capacitor demodulator. Increasing the modulation frequency will cancel them better, just as what happens to the flicker noise. The higher ratio of modulation frequency to the harmonic frequency, the better it will be removed. This explains why the higher order harmonics decrease less than the lower order ones.

6. 4 Multiple device chip test

Improvements can be achieved by using multiple devices as discussed in Chapter 5. The following tests were performed with multiple IMU chip including lateral accelerometers and vertical gyroscopes. These chips are fabricated in AMS 0.6 µm CMOS process.

6-4-1 Multiple accelerometers in parallel

Multiple accelerometers can be integrated into one chip in parallel. Due to the curling problem of the CMOS-MEMS structure, each device can not be too large, which may limit the noise floor performance. If the outputs of multiple accelerometers in parallel are combined together,
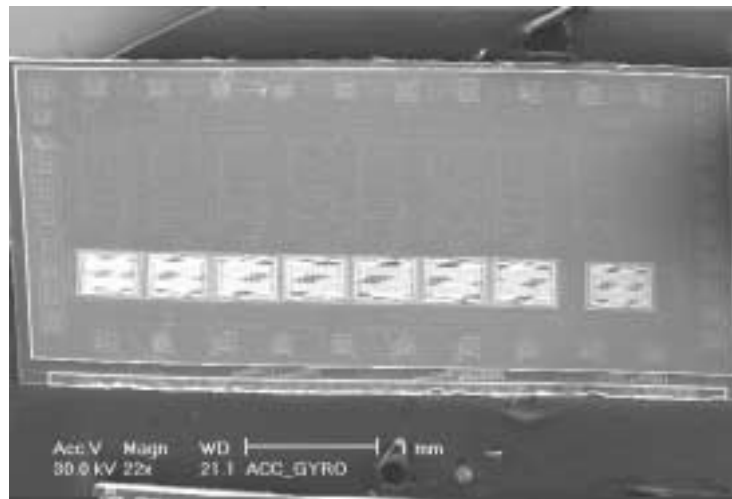

Figure 6-20. SEM of 8 accelerometers

because the sensing signal is correlated, the sensitivity increases by the times of N. At the same

time, since the noise is uncorrelated, it is increased by the times of sqrt(N). Thus the signal-to-noise-ratio (SNR) can increased. Figure 6-20 is the SEM of a chip (named hh_AMS16) which has 8 identical parallel accelerometers and supporting circuits on chip. Figure 6-21 shows waveforms and spectrum of the accelerometer output. Figure 6-21 (a) trace 1 is output of one of the 8 accelerometer, trace 2 is the sum (negative) of 8 accelerometers and trace 3 is the reference accelerometer (5G 400Hz). The peak of the sum signal is 16.3 dB higher than the single accelerometer output while the noise floor of the sum is 12 dB higher. Thus the signal to noise ratio (S/N ratio) is increased. The improvement is not as high as predicted 9 dB. This is because the noise of 8 accelerometers is not completely uncorrelated. There is common background noise to all of the 8 accelerometers and can be summed up.

Although the noise improvement is not impressive, the multiple parallel accelerometers have another potential benefit as a backup--if one accelerometer stops working the full system can still function.
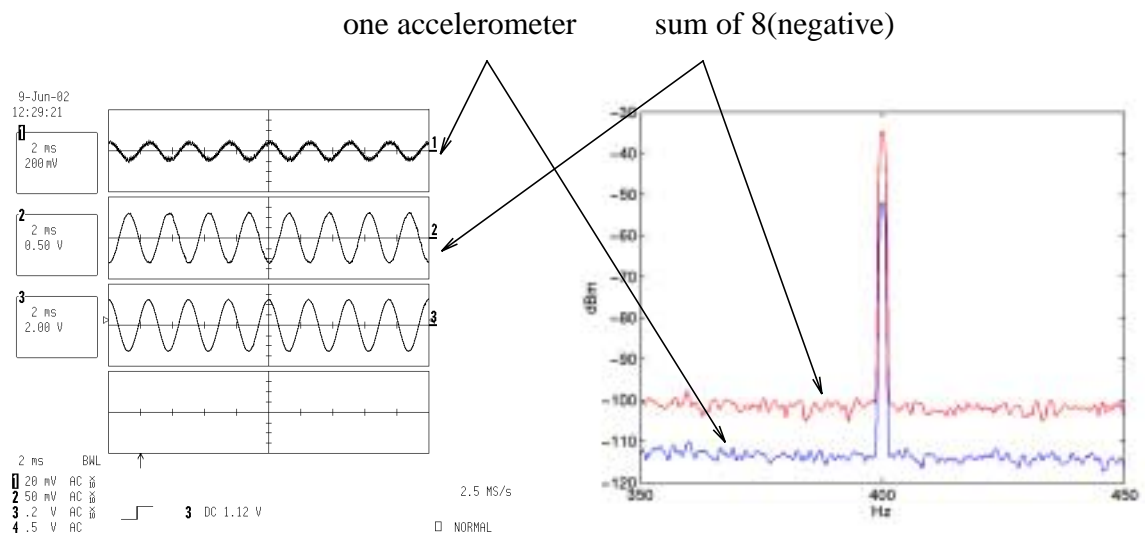
6-4-2 Orthogonal accelerometer pair

Figure 6-21. (a) Output waveforms of accelerometers (5G 400Hz). (b) Spectrum of one accelerometer and sum of 8 accelerometer (1G 400Hz).

Usually accelerometers inevitably have cross-axis coupling. Two orthogonal accelerometers can compensate each other to cancel the cross-axis sensitivity. Figure 6-22 is the orthogonal accelerometer pair (named hh_AMS12). Figure 6-23 shows the outputs of the two accelerometers with acceleration input of 1G 330 Hz in x-axis. The insensitive axis (ay) has an attenuation of 30 dB. By carefully adjust the canceling circuit, the cross-axis sensitivity can be compressed additionally 20 dB. But due to small phase error, the simple cancelling circuit shown in Figure 6-23 can not completely cancel the cross-axis sensitivity.
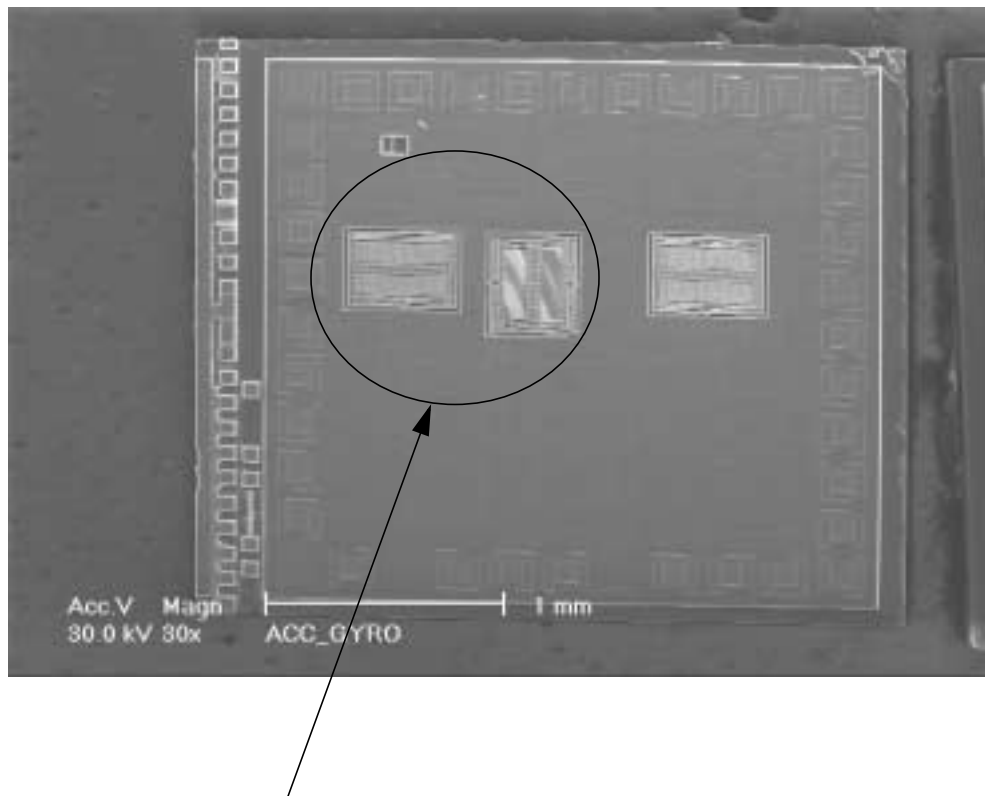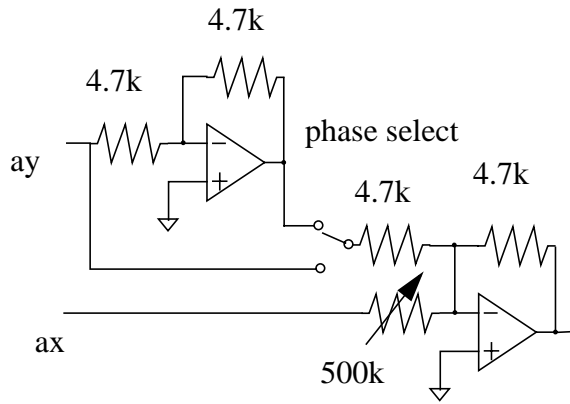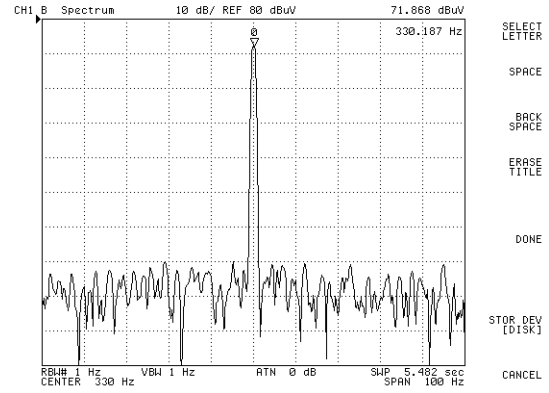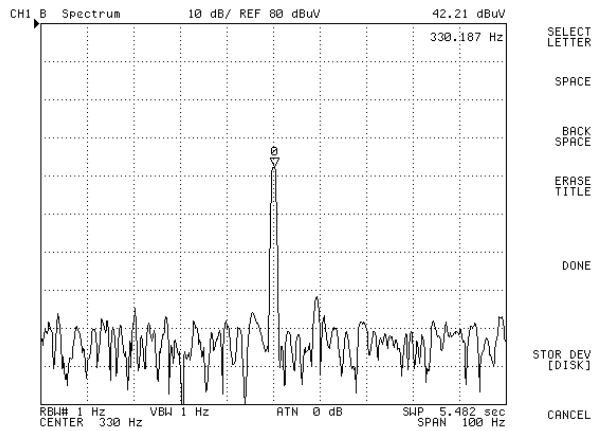

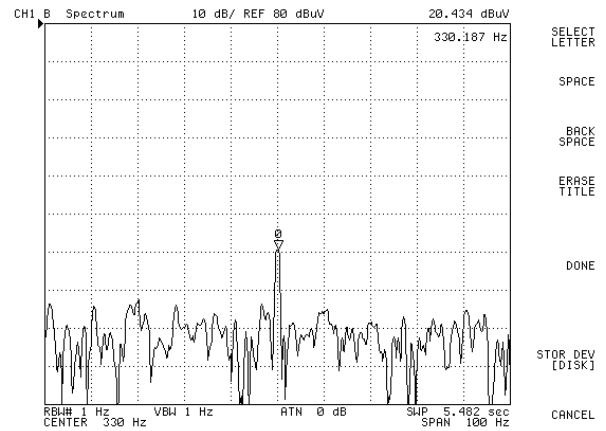Figure 6-22. Orthogonal accelerometer pair.

(a)

(b)

(c)

(d)

Figure 6-23. (a) Cross-axis canceling circuit. (b) Output of x-axis with input of 1G 330Hz in x-axis. (c) Output of y-axis without compensation. (d) Output of y-axis is compressed 20 dB with compensation.

6-4-3 Accelerometer and gyroscope pair

Although gyroscopes are designed to sense rotation, they have acceleration sensitivity in the sensing mode axis. Using another accelerometer aligned to the gyro sensing mode, the interference of acceleration to the gyroscope can be compensated. To get best compensation, it is better to have the same accelerometer as the gyroscope sensing core. In this test, two identical gyroscopes were designed on a same chip (named hh_AMS2_Sept_00). The only difference is that one of them has its oscillation driving node connected to the ground and only the sensing core, the inner accelerometer, is working. This arrangement works as the reference accelerometer. Since both gyroscopes are integrated on the same chip, they experience the same acceleration. By subtracting the output of the reference accelerometer, the acceleration part in the gyroscope output can be eliminated.

Figure 6-25 shows the outputs of both the accelerometer and the gyroscope. Trace 1 is the output from the accelerometer, trace 2 is the output from the gyroscope (after first stage demodulation), trace 3 is the reference accelerometer output, and the middle trace (1-2) is the result of
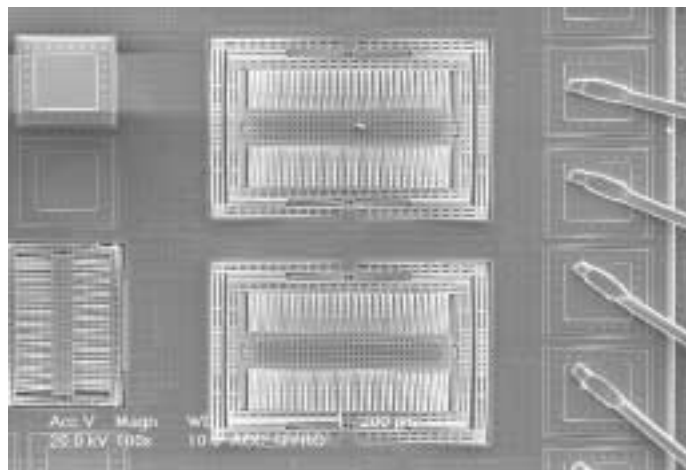

Figure 6-24. Accelerometer and gyroscope pair.

Hao Luo

subtracting the trace2 from the trace1. As can be seen, after subtracting, the final output trace (gyro-acc) cancels the existing acceleration, while the Coriolis signal is not affected.
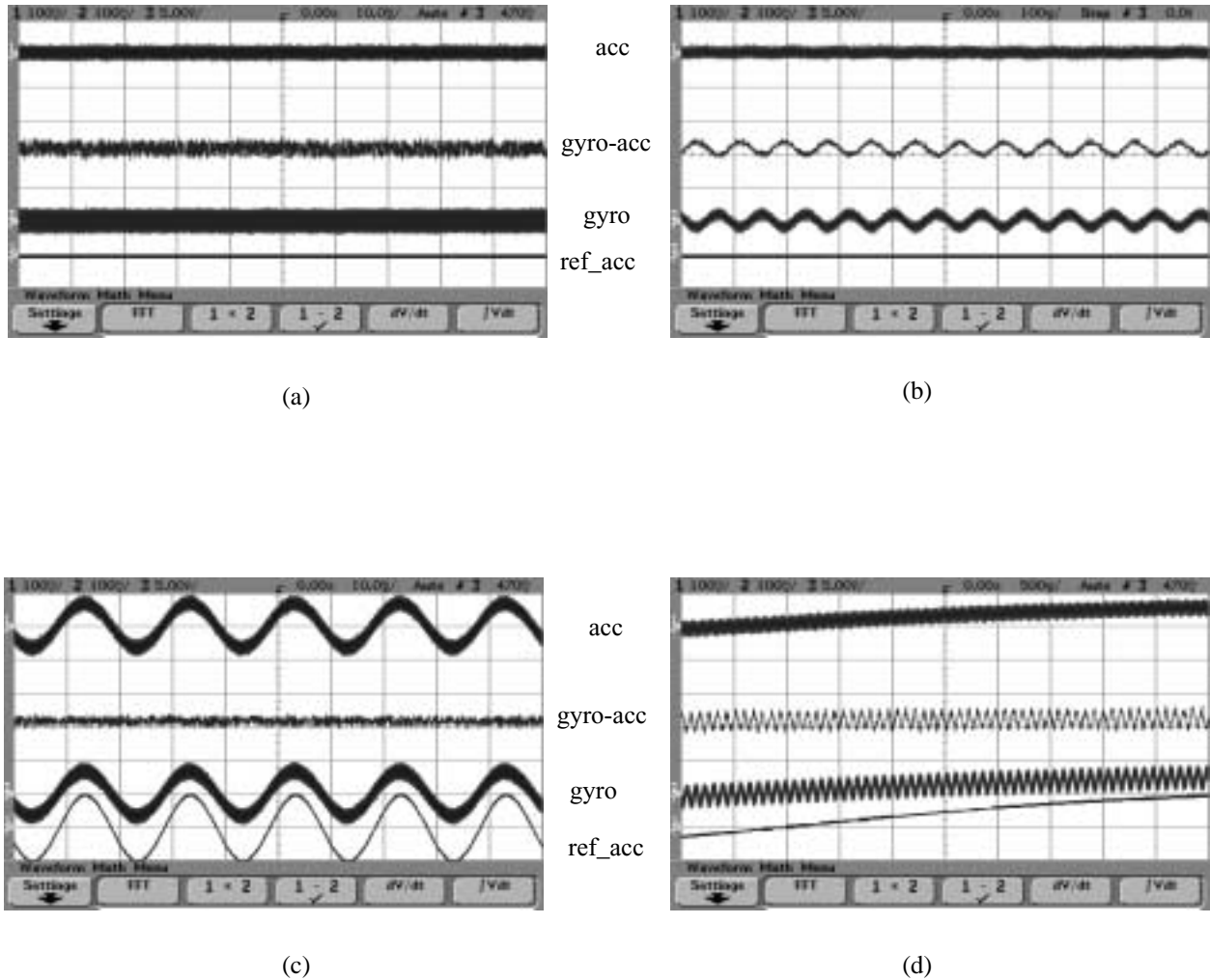

Figure 6-25. Accelerometer and gyroscope pair outputs (a) 0 G input, (b) 0 G input, close-up (c) 1G input (d) 1G input, close-up.

6-4-4 Gyroscope pair

Another way to cancel the linear acceleration sensitivity is using gyroscope pair driven in opposite direction. Since the Coriolis force is a differential signal while the acceleration is a common mode signal, it is possible to cancel the acceleration without affecting the rotation sensing signal. Two identical gyroscopes with mirror symmetry were designed on the same chip. But the fabrication variation cause these two gyroscopes to have different resonant frequencies. After several times of designs and fabrications we have found that the difference is normally about 200~600Hz which makes it impossible to drive these two gyroscopes in 180 degree out of phase. Another design (named hh_AMS15) uses coupling beam between the two gyroscopes to force them have a unique common resonant frequency (Figure 6-26). But due to the too large structure size, the device curls unbalanced. We did not get success to drive the two gyroscopes to move in opposite direction because the twist mode is always triggered when driving voltage is applied. For an improved design, the coupling beams can be designed at the corners of the frame so that the twist mode can not be easily triggered.
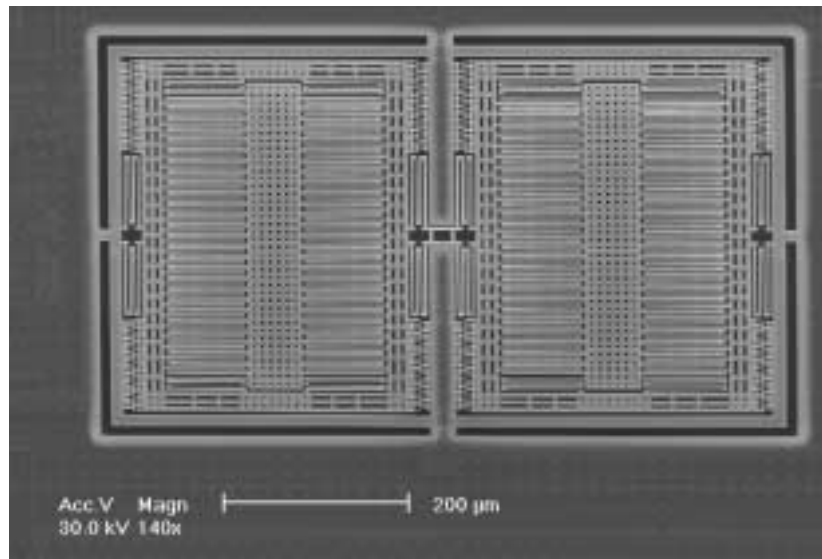

Figure 6-26. Gyroscopes pair with coupling beams.

6-4-5 3 DOF IMU system

As mentioned before, integration has many benefits. The main motivation for integration is size and cost (Figure 6-21).

An integrated IMU system with 3-degree-of-freedom (3DoF) sensing abilities has been designed in a 2.5mm by 2.5mm chip. This system (named hh_AMS12) has two accelerometers in x and y axes and one z-axis gyroscope integrated on the same chip. It also includes the gyroscope oscillation driving amplifier and the frequency doubler for demodulation. Figure 6-28 is the SEM of the released chip and Figure 6-29 shows the system block diagram.

1st generation accelerometer
(off-chip circuit)

1st generation gyroscope
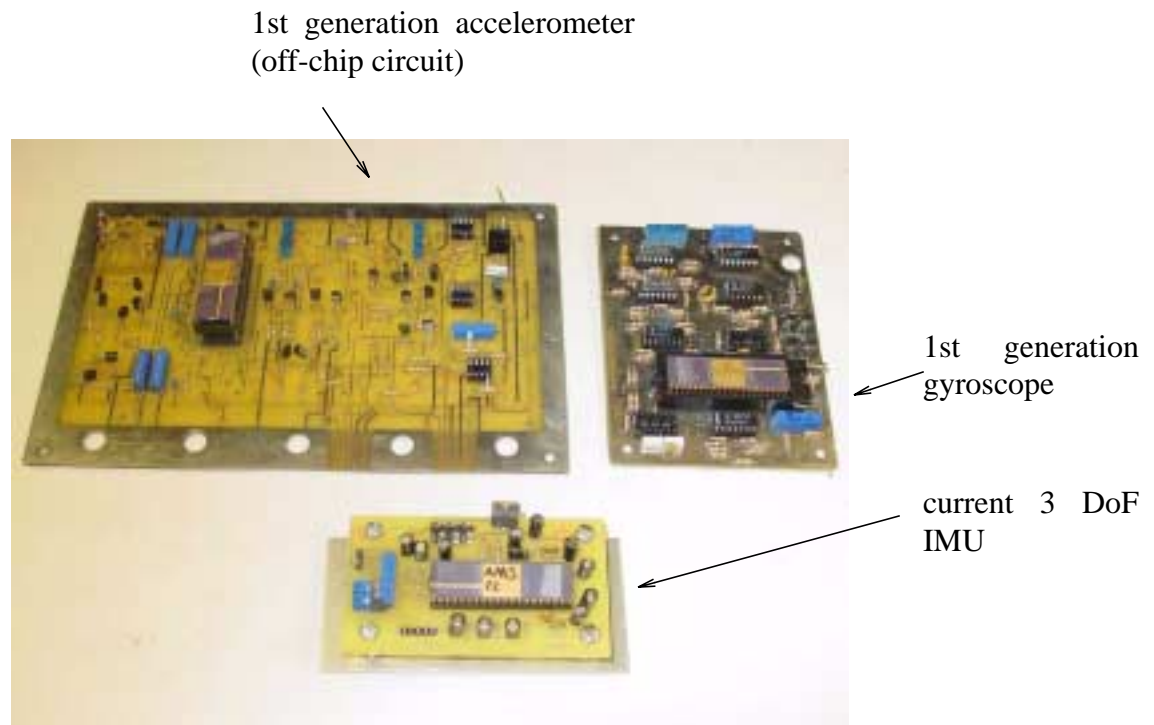
current 3 DoF IMU

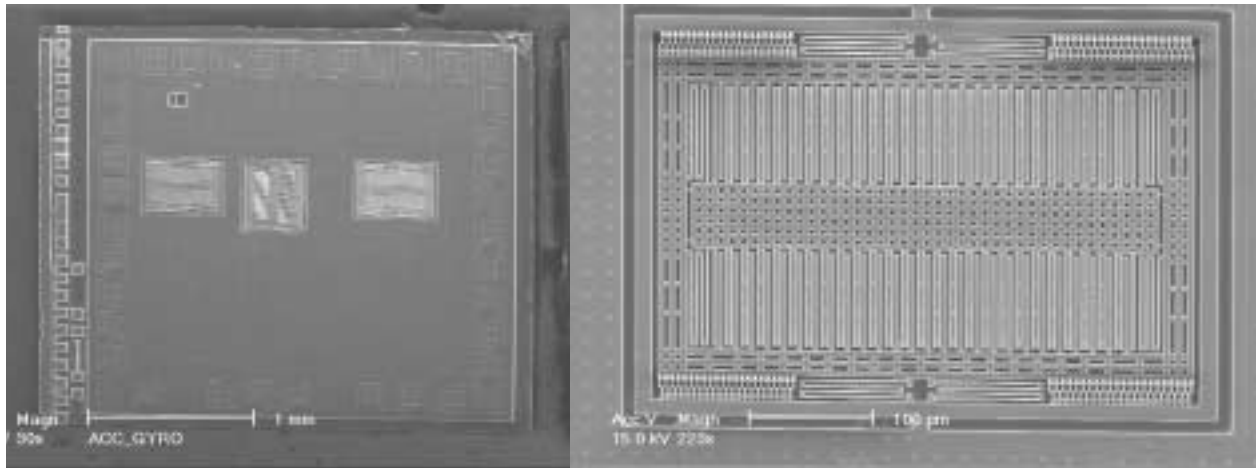Figure 6-27. Comparison of previous IMU system and current design.

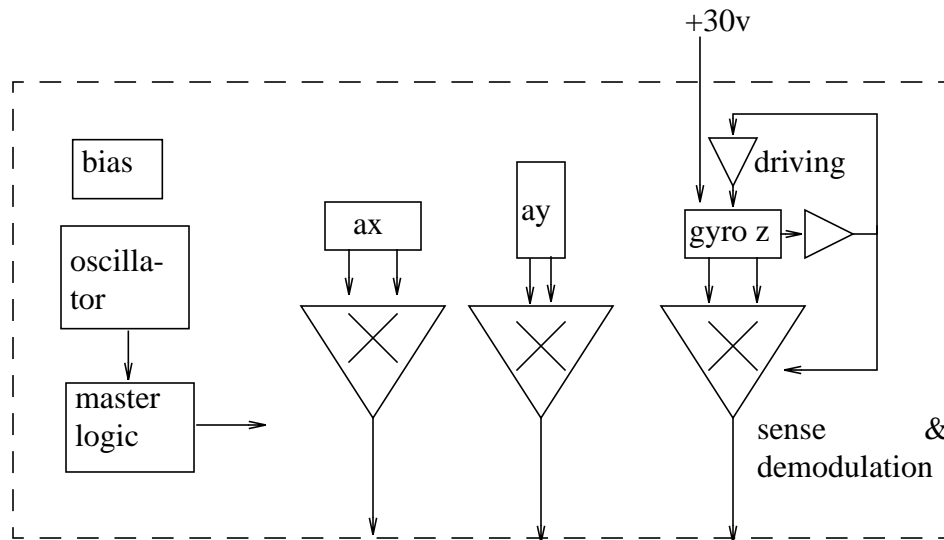Figure 6-28. SEM of 3DOF IMU chip and gyroscope.

Figure 6-29. 3DOF IMU system block diagram

Figure 6-30 shows the pictures captured while the gyroscope is in oscillation. Note that the

comb fingers engagement changes in two phases. The driving mode has a resonant frequency of

Hao Luo

11.6 kHz with Q of 70. The driving motion amplitude is 2.6 µm. The sensing mode has a resonant

frequency of 16 kHz with Q of 6. After the mechanical characteristics under normal conditions
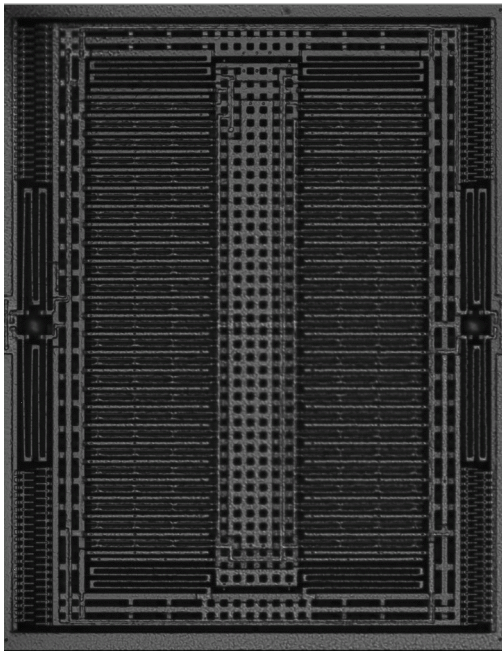
spring compressed
to the right side
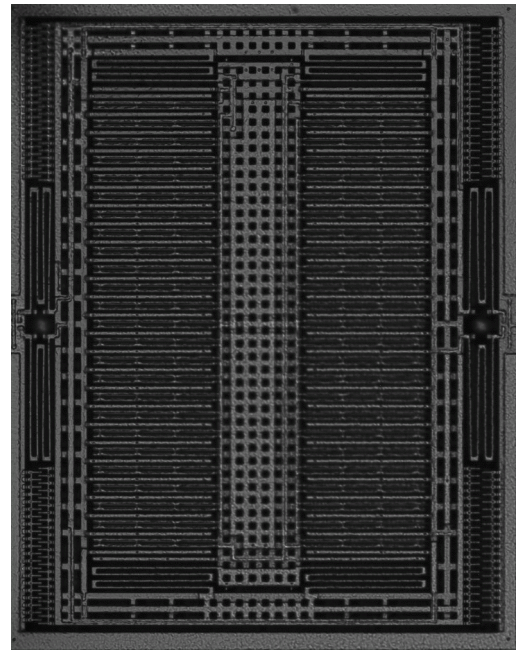
spring compressed
to the left side

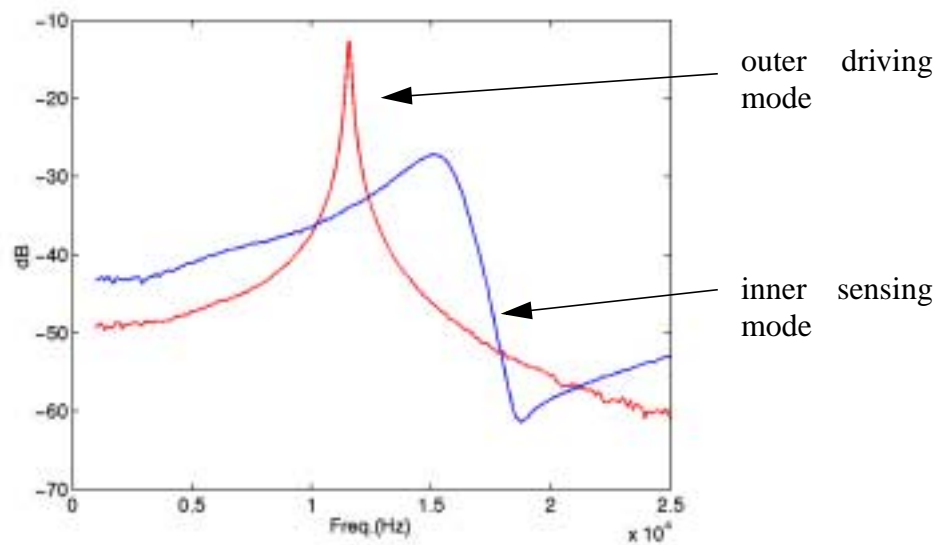outer driving mode

inner sensing mode

Figure 6-30. (a) Two phases captured in gyroscope oscillation (tested with 9 V DC bias, 9 V AC driving). (b) Gyro driving mode resonant frequency (tested with 30 V DC bias, 315 mV AC driving) and sensing mode resonant frequency (tested with 5 V DC bias, 315 mV AC driving).

were tested, another experiment under vacuum condition was performed. A vacuum sealing machine was created to make a vacuum package (Figure 6-31, see the appendix for the vacuum sealing process details). The ceramic package is sealed under 200 mtorr pressure in the chamber, then it was taken out and tested in the open air. Figure 6-32 shows again the two mode resonant frequencies. The quality factor of the driving mode is increased from 70 to 270 while the sensing mode Q is boosted even more from 6 to 90. After long term observation, no leakage was found. Although test shows that no performance has been improved from the vacuum sealing, it has at

Figure 6-31. Vacuum sealer, sealing machine controller and vacuum sealed package.

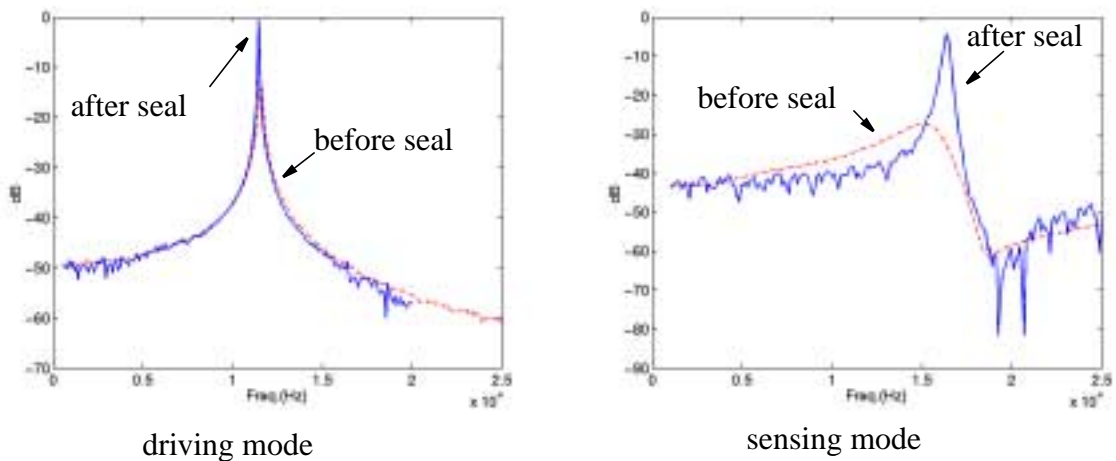driving mode   sensing mode

Figure 6-32. Two mode resonant frequencies after vacuum sealing.

least one benefit -- it reduces the gyroscope driving voltage more than 3 times. For example, the normal gyroscope requires 30 V DC bias voltage to drive the proof-mass 2.6 μm in oscillation, after vacuum sealing, it only needs 10 V, which can be easily achieved with an integrated charge pump (this is important because the AMS CMOS process transistor breaks down at 15 V).

Outputs from three IMU sensors are shown in Figure 6-34. The accelerometer output sensitivity is 160mV/G (sensor sensitivity is 0.7mV/G). The integrated accelerometer has a noise floor of $0.5mG/\sqrt{Hz}$. The gyroscope has an output sensitivity of 0.14 mv/°/sec (sensor 0.7μV/°sec) and noise floor of $0.3°/sec/\sqrt{Hz}$.
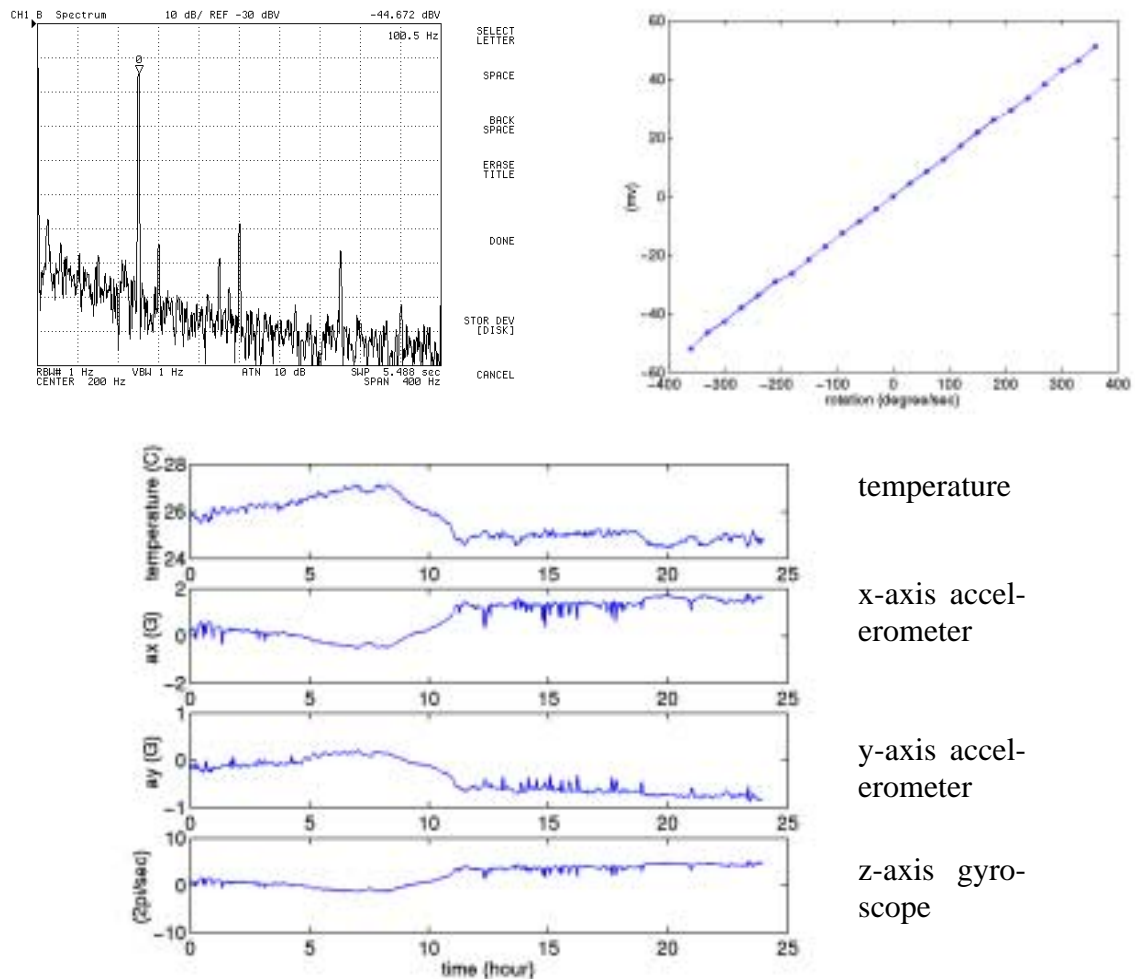

Figure 6-33. Accelerometer output spectrum (1G 100Hz), gyroscope DC response and system temperature drift.
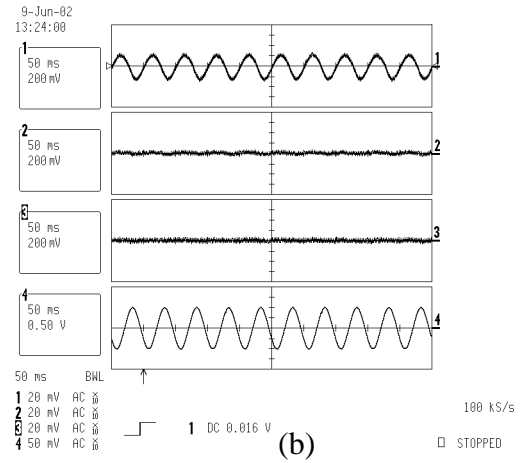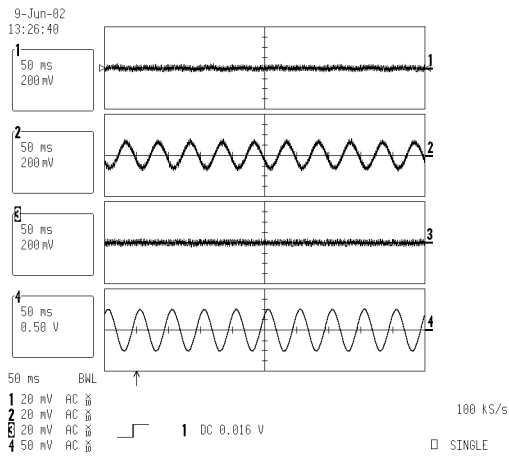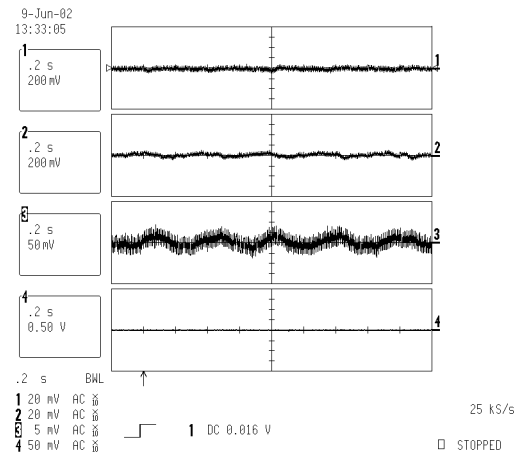
Figure 6-34. (a) 3DOF IMU test board. (b) Excited by 1 G 20Hz acceleration in x-axis. (c) Excited by 1 G 20 Hz acceleration in y-axis. (d) Rotated by hand with speed about 360 °/sec.

6. 5 Summary

In this chapter several kinds of IMU chips are tested. These results validate the design methodology described in previous chapters. As the last chapter discussing CMOS-MEMS IMU in this thesis (the next chapter will focus on RF applications) some general conclusions and future work are given below.

CMOS-MEMS has advantages as a low-cost highly integrated process to implement inertial measurement units. However, before commercialization, several challenges have to be met. First, the structure curling problem has to be solved. It is important to use low stress material to build the device. It would be better to have a separate mechanical layer with controlled stress. During past several years, we have met several situations that changes in the foundry fabrication requires redesign of our devices (a fabless design house is not likely to meet this requirement). Secondly, the electronic noise has to be lowered. It is quite clear that there is still plenty of room to improve the performance by better designed circuits. Low noise low drift circuit is the key to improve the system performance. Thirdly, packaging cost has to be lowered. The CMOS-MEMS structure can not be sealed as normal CMOS chip in the plastic packages. How to seal the structure without destroying it is a key issue that needs to be investigated. For example, how does one make a cover on the structure so that the structure will not be touched during packaging process.

Hao Luo

Chapter 7

CMOS-MEMS in RF Applications

CMOS-MEMS technology can not only be used in IMU applications, but also can be applied in other fields. In this chapter, we will exploit the CMOS-MEMS technology in RF applications. Current IC technology in RF design is difficult. One of the main reasons is that high quality inductors are not available in conventional IC fabrication process. The loss due to eddy currents makes the integrated inductor in the conventional IC process have very low Q at GHz frequencies. CMOS-MEMS technology can be used to reduce the eddy current by removing the silicon under inductor coils. In this chapter, two types of RF oscillators using MEMS technology are investigated.

7. 1 Copper RF oscillator using CMOS-MEMS technology

Two main reasons for the energy loss in the RF inductor are the resistive loss and substrate eddy current loss. Due to the limited conductance of the inductor building material, there is inevitable resistive loss. This problem worsens at high frequency because of skin effect. The resistive loss can be mitigated by using thicker metal or choosing higher conductive material such as copper. Meanwhile, if there is conductive substrate underneath the coil, such as the silicon, there will still be eddy currents in the substrate due to the magnetic field generated by RF currents in the coil. Using the MEMS technology, the silicon can be removed by deep RIE process and the eddy currents will be significantly decreased. As a result, the quality factor (Q) of the inductor can be improved (Figure 7-1).
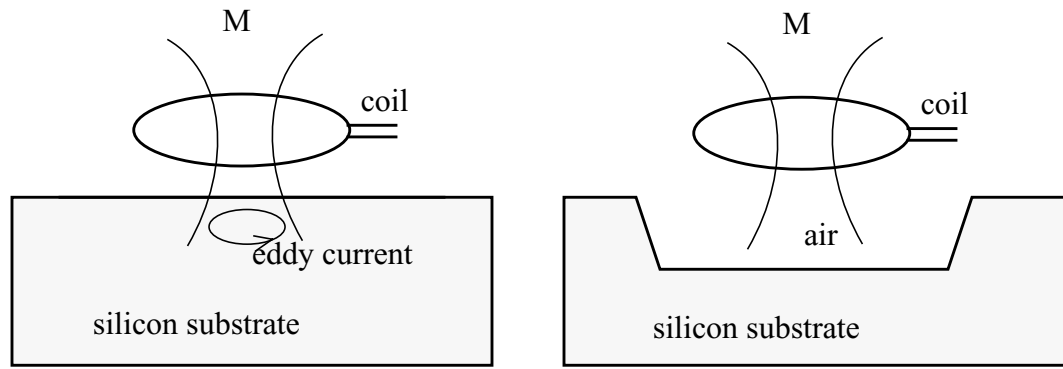
Figure 7-1. Remove silicon underneath the coil to decrease eddy current.

An RF oscillator has been designed and fabricated in the UMC 0.18 μm 6 layer copper CMOS process. Figure 7-2 shows the oscillator schematic and its layout. The 3.2 nH inductor is integrated on the chip using the copper interconnect.

Before the release process, the chip was tested and no oscillation signal was found. The possible reason is that the inductor has too much parasitic capacitance and very low Q. The energy loss is greater than the supply from the circuit so that the oscillation could not be built. In the next step, the silicon underneath the copper coil is removed by deep RIE process to reduce the eddy current. By this way the inductor Q can be improved to 12 at 7.5 GHz [51]. With the power supply voltage of 3 V, the oscillator consumes power of 60mW and generates oscillation around 2.2 GHz. Figure 7-4 shows the oscillation signal spectrum and the relation between the supply voltage and the oscillation frequency. The phase noise at 100kHz offset is about -60dBc/Hz.

It was also found that the structure becomes leaky after the micromachining process. Some isolated layer or circuits becomes conductive after the process. It is caused by the RIE by-product which was deposited on the structures during the micromachining process. The frequency control voltage could not be applied to the tuning transistor capacitor (will stop the oscillation). But the

98/
0.36   vdd

98/
0.36

MOS
cap

output buffers
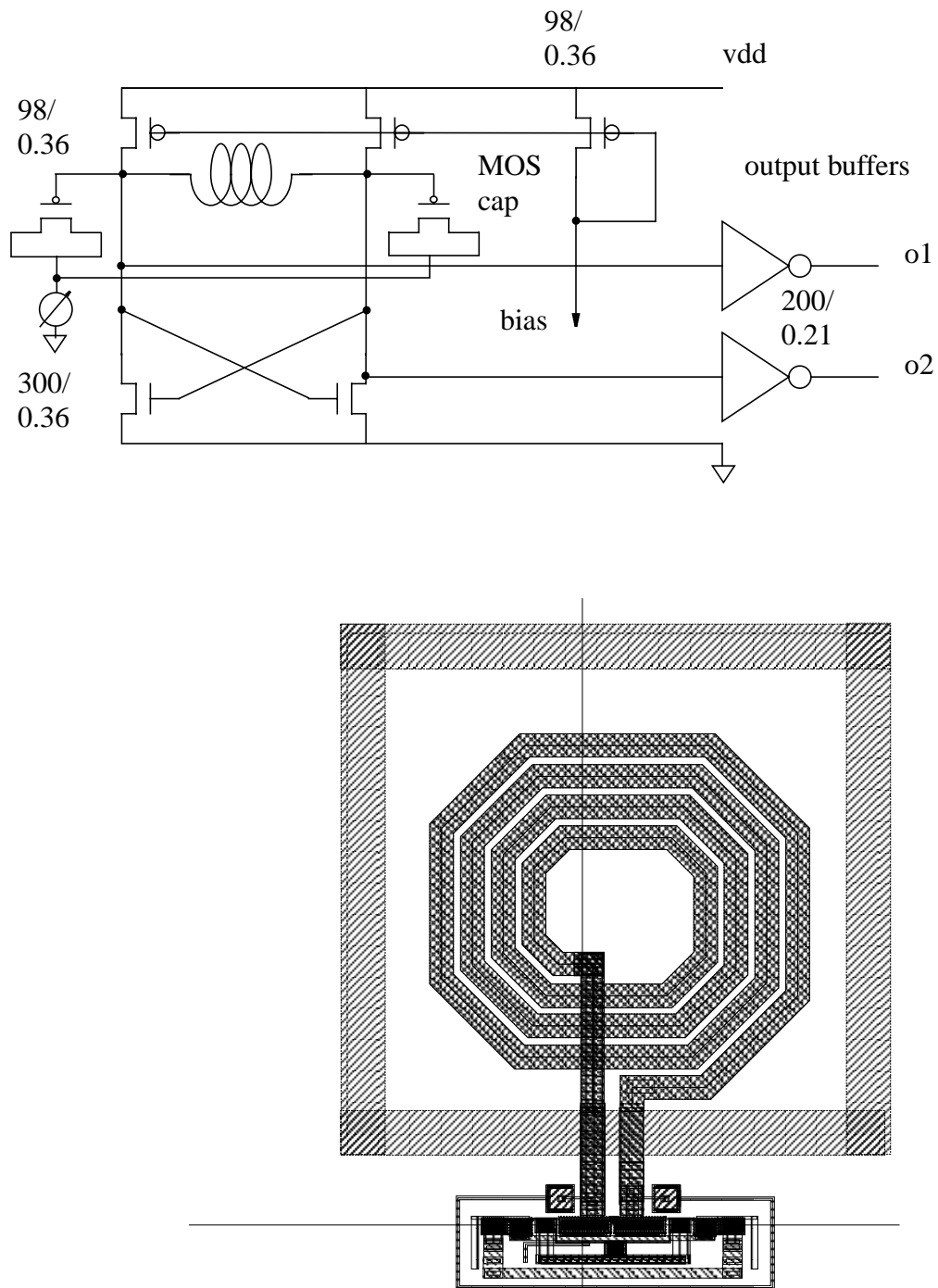
o1

200/
0.21

bias

o2

300/
0.36

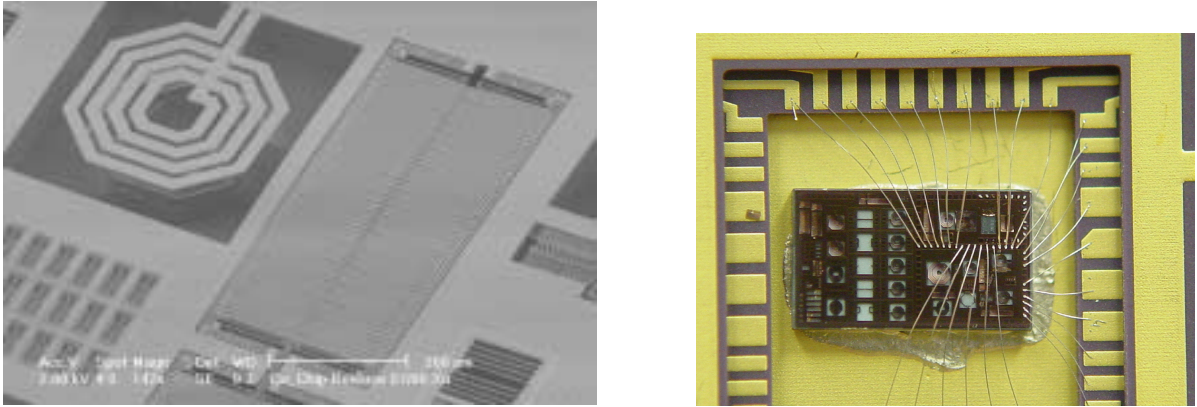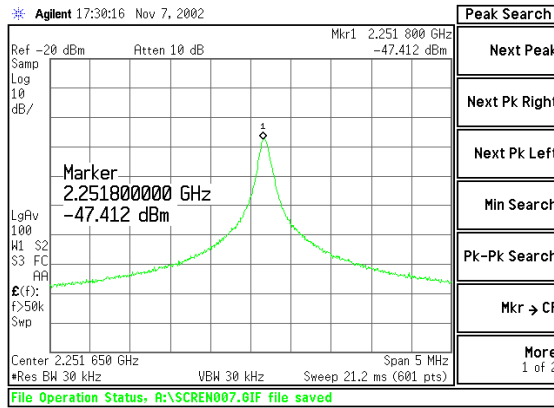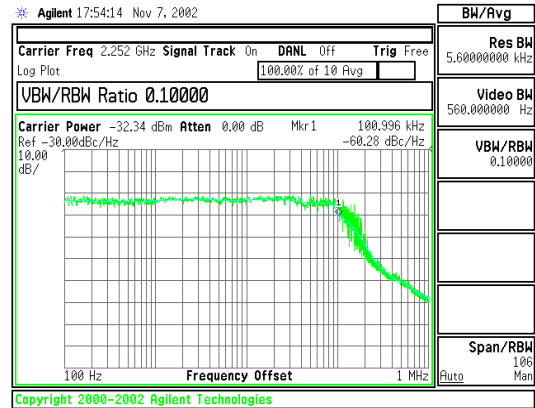Figure 7-2. Copper CMOS RF VCO schematic and layout.

Figure 7-3. Released copper CMOS RF oscillator chip and test package.
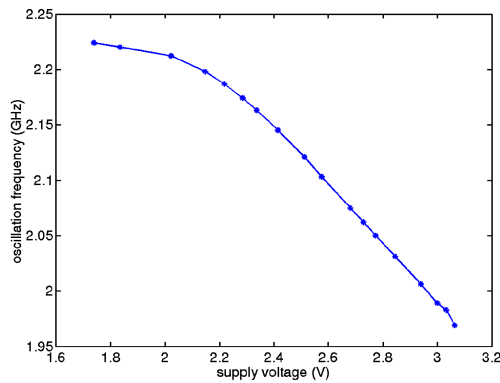
frequency can be tuned by the power supply voltage and the tunable frequency range is about

800 MHz (Figure 7-4).

(a)

(b)

(c)

Figure 7-4. (a) Copper CMOS RF VCO oscillation signal spectrum. (b) Phase noise. (c) Frequency tuning range.

7. 2 SiGe RF oscillator with micromachined inductor

Another RF VCO is fabricated with the IBM 5HP silicon-germanium process through MOSIS. In this process, the inductor is implemented with the aluminum interconnect. To reduce the coil resistance, most of the coil is in the top 2 μm thick metal layer and the round shape coil is used. The silicon underneath the coil is removed by the deep RIE process. The coil is designed with multiple paths so that each path structure has smaller width which is helpful to remove the silicon. The peripheral metal is cut with some slots to reduce the eddy current loss further. Figure 7-5 shows the schematic and layout of the VCO.

The test board and setup are shown in Figure 7-7. Six packaged VCO chips have been tested with Agilent PSA4440 spectrum analyzer. The tested samples include three released chips and three unreleased chips. For the released chips, the resonant frequency distribution is within 5.05 GHz~5.2 GHz with power supply of 3 V and 12 mA. For those chips without micromachining enhanced inductors, no oscillation signal can be found under 3 V power supply. After the power voltage has been increased to 3.7 V with 18 mA current, the unreleased chips start to oscil-
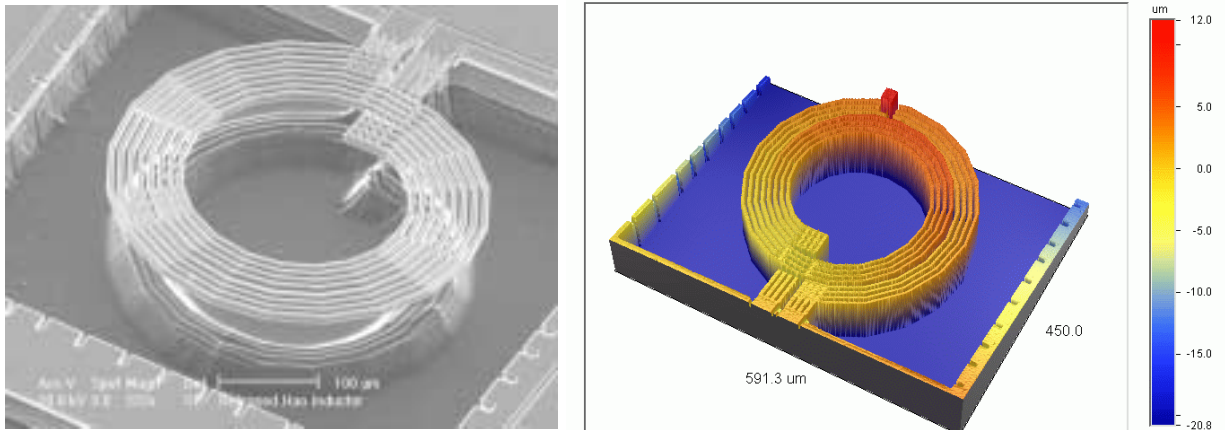
Figure 7-6. Inductor fabricated in IBM SiGe process and its curl measurement result.

Figure 7-5. SiGe CMOS RF VCO schematic and layout.

late. The oscillation frequency for unreleased chips is lower (4.96GHz~4.98 GHz) and the amplitude is also lower (about 30 dBm lower than those micromachined chips). The wider frequency distribution of the released chip is due to the curling variation after the micromachining process. The superiority of the released chips is not a surprise since those micromachined inductors has
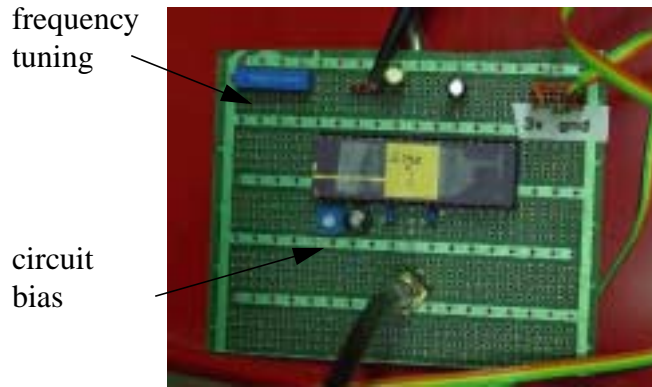
Figure 7-7. SiGe VCO test board.
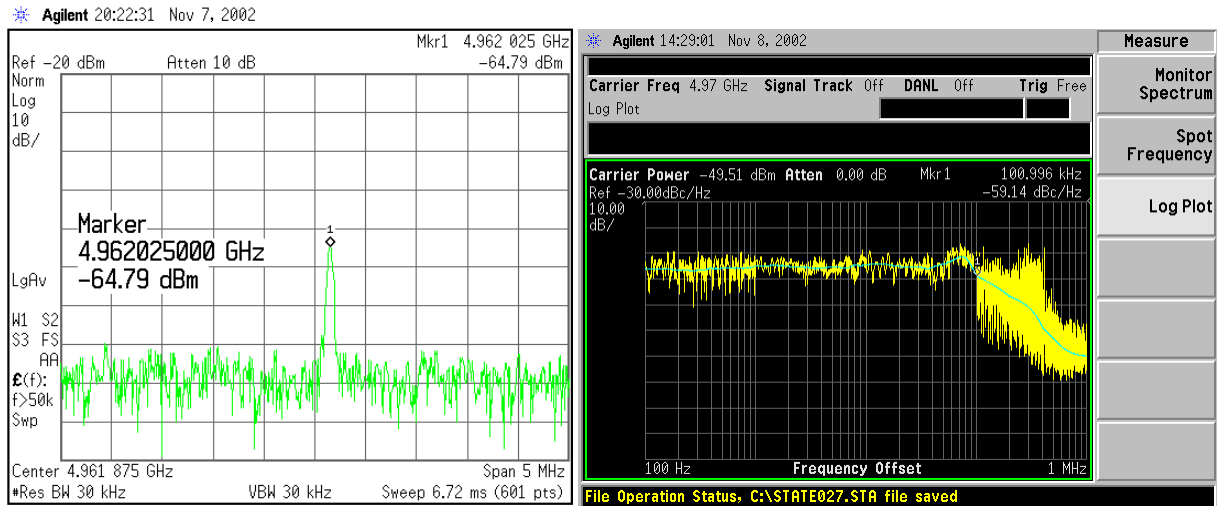
Figure 7-8. The unreleased VCO generates an oscillation signal at 4.96 GHz.

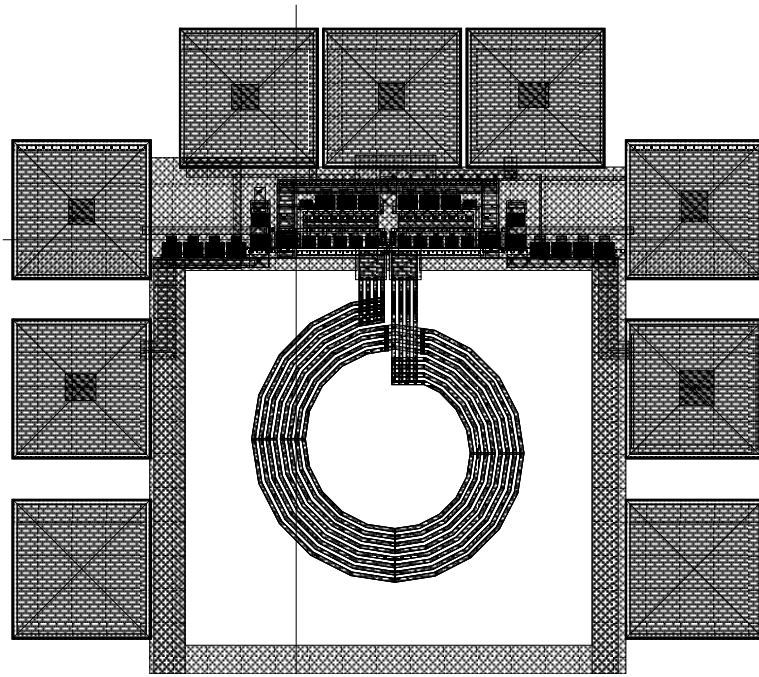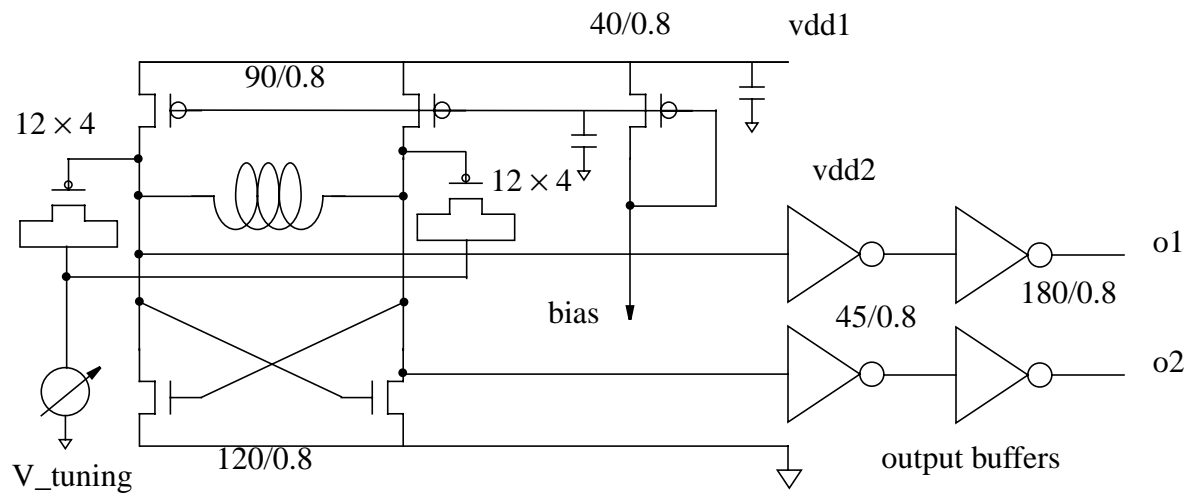higher Q which makes it easier for the circuit to oscillate. Since the released inductors have less parasitic capacitance to the substrate, the oscillation frequency is higher. The unreleased inductors has lower Q, thus they need more power and higher transistor g_m to compensate the power loss for sustaining the oscillation.

Figure 7-8 shows the oscillation signal spectrum of a VCO with unreleased inductor. The frequency is at 4.96 GHz and power is -65dBm.

Figure 7-9 shows the oscillation signal of a VCO with micromachined inductor (singe-ended output, span 5MHz, VBW of 30kHz). Note that the single-ended output impedance is not carefully tuned to match the 50 Ohm transmission cable, thus there is some attenuation. But it can still give some general information about the signals. The output power from the output buffer is -34 dBm and the phase noise at 100 kHz offset is about -70dBc/Hz. The power consumption of the resonator core is 12mA with 3V supply. The two output buffers consume power of 20mA at 3V (may vary depending on the load).

The frequency can be tuned by changing the MOS capacitors bias (Figure 7-10). The tuning range is ~120MHz for control voltages from 2.8V to 4V (Figure 7-11). Figure 7-12 shows the tuning frequency versus control voltage. The actual maximum tuning range is larger than 120MHz, but if the frequency is out of that range the signal becomes too weak and the oscillation may stop.
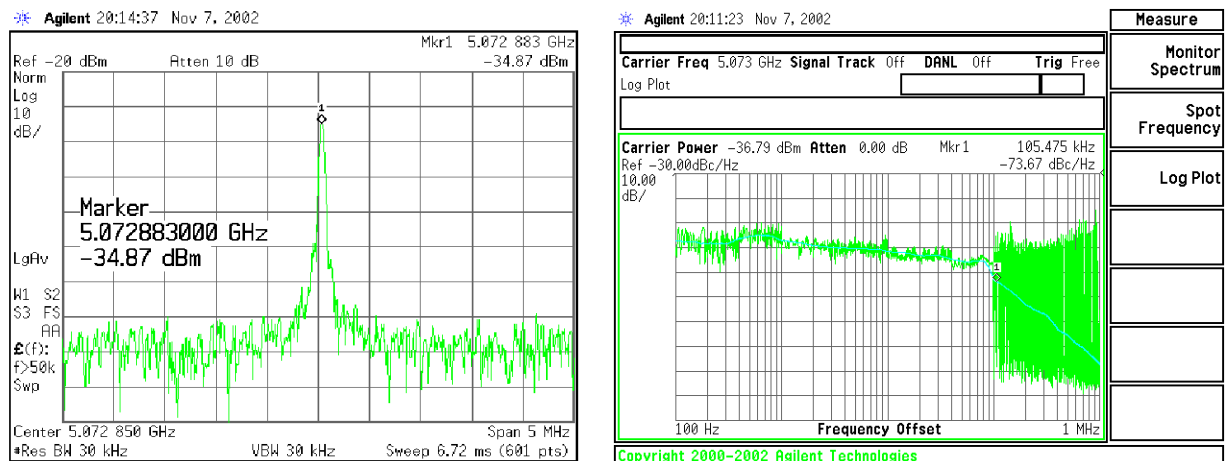
Figure 7-9. (a) Spectrum of the oscillation signal from a released chip. (b) Phase noise
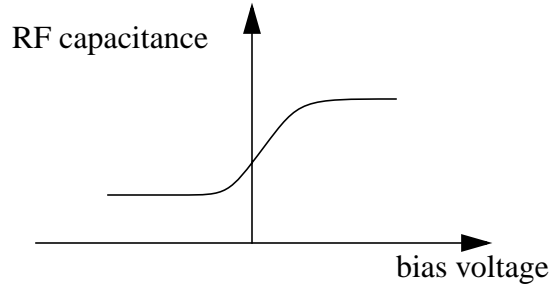
Figure 7-10. MOS capacitor RF capacitance change with bias voltage.
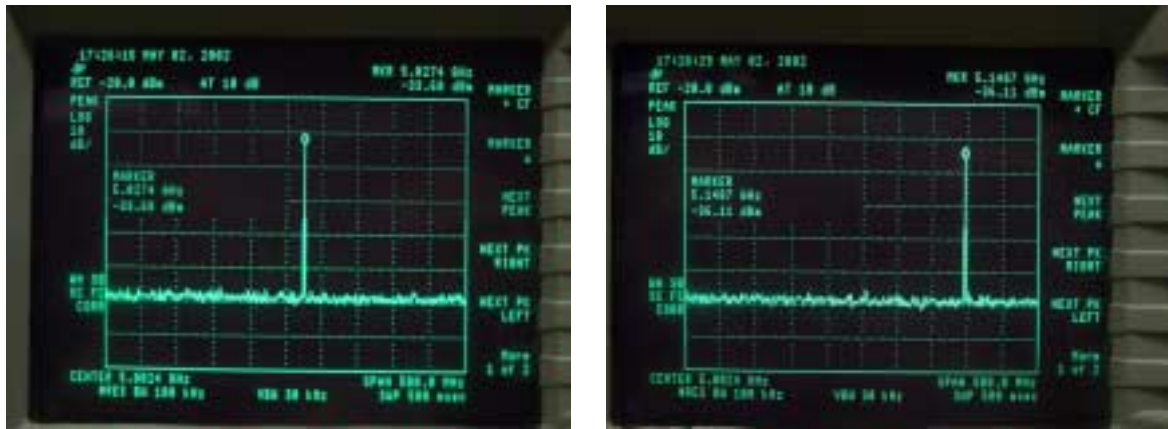
Figure 7-11. Frequency tuning range from low end to high end

7. 3 Simulation of the inductor coils

Although it is difficult to precisely simulate the RF distributed system, it is helpful to use CAD tools to simulate it to get some insights about the parts, especially when the parts are integrated in the circuit, such as the inductor in the SiGe chip, which have no way to be measured. The following paragraphs and pictures show the simulated behaviors of the inductor coils using RF FEM software "Hewlett-Packard advanced design system (hpads)".
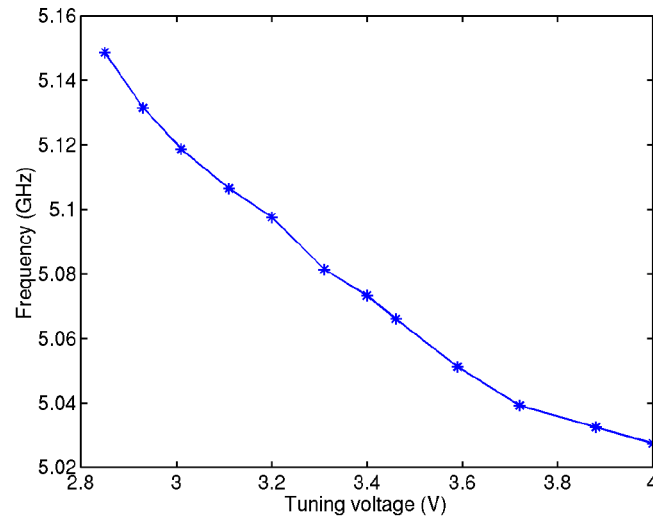
Figure 7-12. Frequency versus tuning voltage.

Measured examples have been simulated to validate the simulator. This step can be used as the calibration of the simulator for future design. The example inductors were fabricated in the previous copper process and measured results are presented in [51]. They are octagonal shape inductors with two ports on two sides (Figure 7-13). The layout is imported into the "hpads" from "Cadence" through GDSII format.

The simulator generates the S-parameters of the network. With the following definition of the inductance and quality factor [52], the inductor parameters are extracted and shown in Table 7-1 and Figure 7-14.

$$Q = -\frac{Img(Y_{11})}{Real(Y_{11})} \qquad \text{(E 7-1)}$$

$$L = \frac{Img(Y_{21})}{\omega|Y_{21}|^2} \qquad \text{(E 7-2)}$$
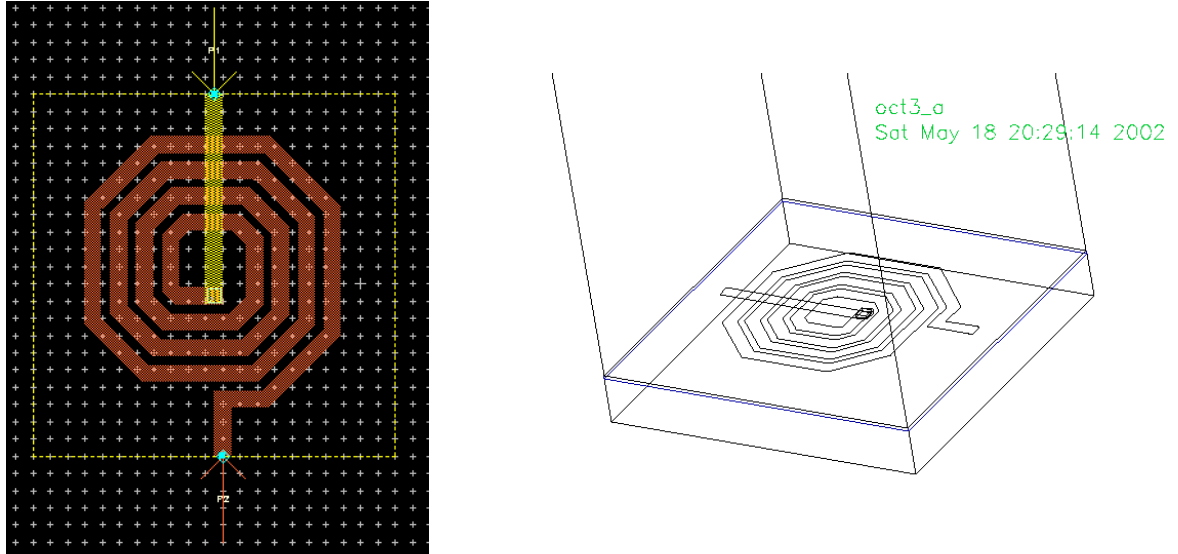
Figure 7-13. Inductor layout and its model in "hpads".

Table 7-1: Inductors measurement and simulation results

		L1	L2	L3	L4
Outer diameter (μm)		300	336	350	365
Inductance (nH)	measured	3.19	3.91	4.15	4.69
	simulation	3.15	3.86	4.21	4.63
Q max	measured	12.5	11.2	10.46	7.61
	simulation	24.7	25.3	23.9	22.1
Q max f (GHz)	measured	7.75	6.50	5.72	4.75
	simulation	14.1	11.2	10.02	10.02
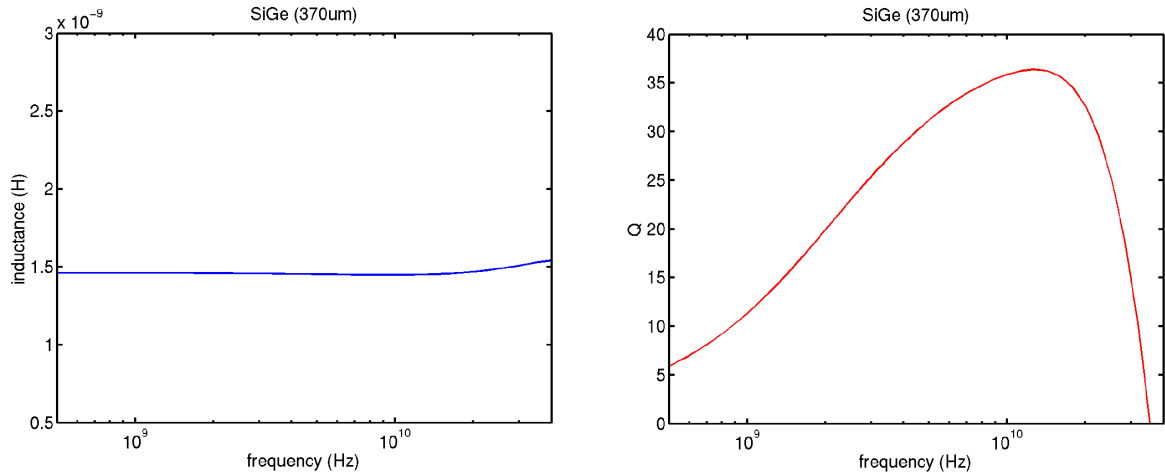
Figure 7-15. Simulation results of inductance and Q of inductors fabricated in SiGe process.

As can be seen, the simulated inductance is very close to the measured value. The simulated quality factor curve has the same shape as the measured curve [51], but the Q_{max} and its frequency are higher than the measured values. The main reason, from the "hpads" manual, is that the "hpads" only takes the skin effect into account while disregards the substrate eddy current loss. The eddy current loss could cost half or even more loss of the Q.

With the above conclusions, the circular inductor in SiGe process is also put into simulation. Unfortunately, due to too complicated mesh of the slotted structure, the simulator never finished the simulation. Thus simplification was made by replacing the slotted structure with a solid metal path which has exactly same geometry size. The simulated inductance is 1.46nH, and the Q_{max} is 36.4 @ 13GHz (Figure 7-15). As can be seen, with the same simulation setup, the SiGe inductor has higher Q and higher usable frequency than the copper counterpart. Some explanations will be given in the next part of this chapter.

To check whether the simulation above makes sense, another circuit simulation in Cadence Spectre^{TM} is performed. The chip was fabricated through MOSIS service using BiCMOS process.
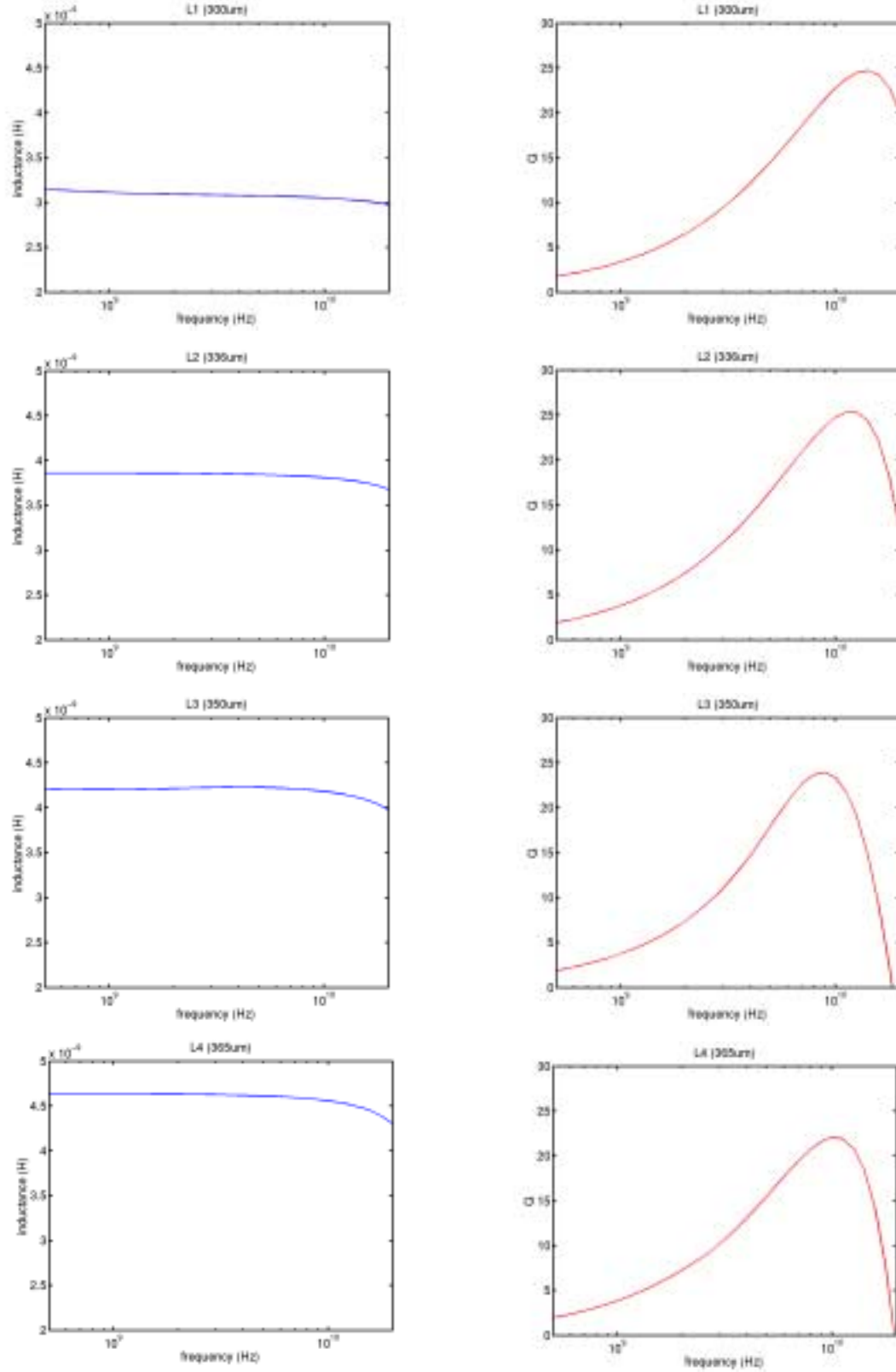
Figure 7-14. Simulation results of inductance and Q of inductors fabricated in copper process [51].
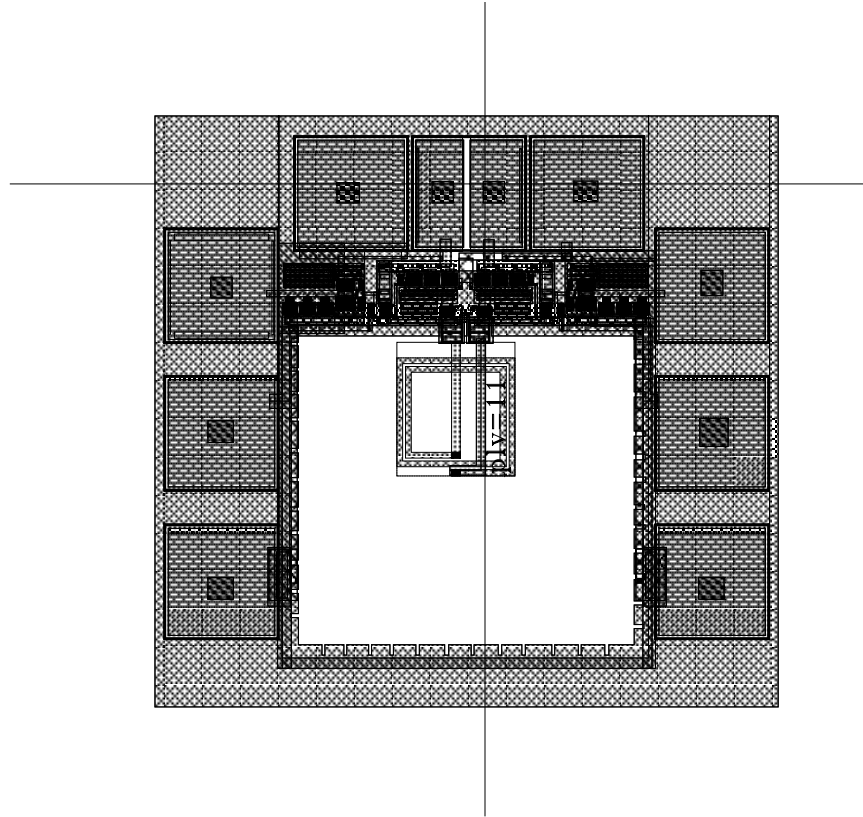
Figure 7-16. Dummy simulation layout.

This service provides models for most of the devices in the process, including some inductors. There are 22 different kind of square inductor cells in the model kit. As described from the released model help information, all the models are verified by fabrication and measurements. Thus they can be used as our standards. An inductor with inductance value closest to the circular SiGe inductor was chosen. This inductor is a square coil with 2 turn, 10 μm wide metal and 200 μm diameter (numbered as "ind11" in the model kit). It has inductance of 1.5nH which is very close to our simulated value. It is used to replace the circular inductor and put into the layout extraction and simulation with Spectre (Figure 7-16). The transient simulation shows the oscillation signal at 5.46 GHz. Considering there is extra parasitic capacitance in the real chip, the measured number (5.1GHz) satisfactorily matches the simulation. The periodic steady state (pss)

simulation and periodic noise (pnoise) simulation shows that this oscillator has a phase noise of -103 dBc/Hz at 100 kHz offset (Figure 7-17). This number is smaller than the measurement result (-73dBc/Hz). The noise is mainly contributed by the transistors which are not modeled very well and lack of RF test experience may also cause extra noise arising from the test enviroment.

7. 4 Comparison to previous work

Table 7-2 compares the RF oscillators with MEMS enhanced inductor to some other works reported recently. As can be seen from the table, generally speaking, the smaller technology feature size, the higher frequency the oscillator can work. The frequency is also determined by the technology process. As silicon-germanium process has higher f_T transistor and the bipolar transistor is available, it has advantages for the RF applications. The MEMS enhanced inductor technique is compatible to all the other process. It can be used as an add-on process to the available technologies to improve the RF performance further.

Comparing the two RF chips in copper and SiGe processes, we may find out that even though the copper process has smaller transistor feature size and less metal resistance, the SiGe chip is superior in RF performance. There are several reasons for this superiority. First, the SiGe process is specially developed for RF analog application while the copper process is for digital circuits. The SiGe transistor has much higher cut off frequency f_T (in 40~200 GHz range) [58][59][60][61][62]. Secondly, the copper coil is in an octagonal shape and each corner is a high resistive point which may cost more Q loss (The coil in the SiGe chip is in round shape). Although the copper has higher conductivity (Cu 5.8×10^7 Siemens/m vs. Al 3.8×10^7 Siemens/m), the SiGe process has thicker aluminum layer (Al 2 µm vs. Cu 0.7 µm), thus the benefit of copper
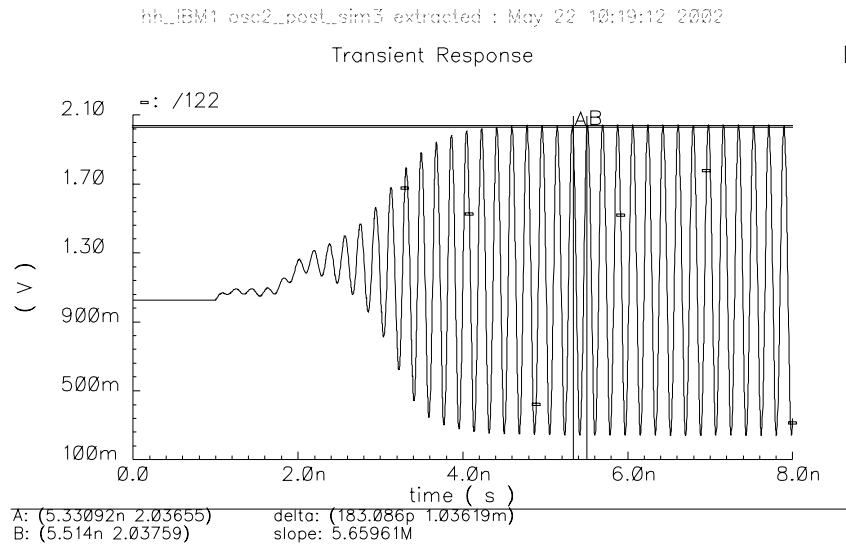
(a)
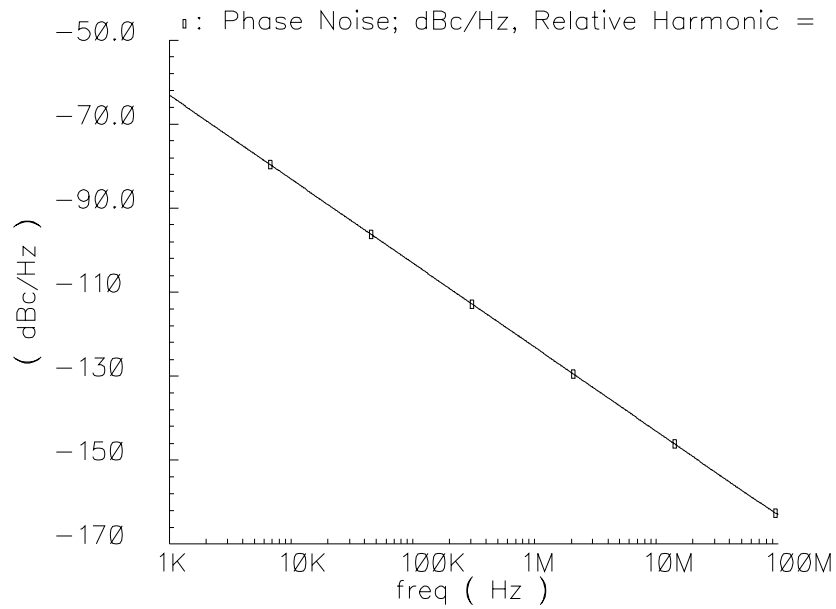
(b)

Figure 7-17. (a) Transient oscillation signal at 5.46GHz. (b) Pnoise simulation phase noise.

Table 7-2: Comparison of RF oscillators

	Technology	LC tank #	Frequency (GHz)	Phase Noise (dBc/Hz)
C.-M. Hung 99 [53]	0.8 µm CMOS conventional spiral inductor	two tanks	1.24	-137 @ 3MHz
Jan Cran-inckx 96 [54]	0.7 µm CMOS conventional spiral inductor	two tanks	1.8	-116 @ 600kHz
Aleksander Dec 99 [55]	0.5 µm CMOS conventional spiral inductor micromachined tunable capaci-tor	two tanks	1.9	-126 @600kHz
C.-M. Hung 01 [56]	0.25 µm CMOS conventional spiral inductor	two tanks	5.35	-116.5 @1MHz
Jean Oil-vier Plou-chart 00 [57]	IBM SiGe BICMOS 0.32 µm bipolar transistor conventional spiral inductor	two tanks	5	-98 @100kHz
This work copper	UMC 0.18 µm copper 0.36 µm CMOS transistor MEMS enhanced inductor	one tank	2	-60 @ 100kHz
This work SiGe	MOSIS SiGe BICMOS 0.8 µm CMOS transistor MEMS enhanced inductor	one tank	5.1	-73 @ 100kHz

property can not show in these two cases. Thirdly, the wide metal path in copper chip hampers the

undercut of the silicon which may cost extra Q loss due to eddy current.

7. 5 Summary

This chapter discusses another application for CMOS-MEMS technology. Two types of RF

VCOs with MEMS enhanced inductors are introduced. The undercut of silicon can improve the

inductor quality factor and increase the self-resonant frequency. This process is compatible to other currently available RF technologies. The micromachined inductors can increase the oscillation frequency and lower the phase noise.

References

[1] M. Lemkin, M. a. Ortiz, N. Wongkomet, B. Boser and J. H. smith, "A 3-axis force balanced accelerometer using a single proof-mass," Tech. Digest 9th Int. Solid State Sensors and Actuators (Transducers'97), Chicago, IL, June 1997, pp. 1185-1188

[2] Analog Device ADXL210 accelerometer datasheet. http://www.analog.com/pdf/ADXL202_10_b.pdf.

[3] Navid Yazdi, Farrokh ayazi, and Khalil Najafi, "Micromachined Inertial Sensors," Proc. of the IEEE, Aug. 1998, pp1640-1659

[4] Mohamed M.R. Mostafa, Applanix Corporation, "History of Inertial Navigation Systems in Survey Applications," Photogrammertric engineering & remote sensing, Journal of the American society for photogrammertry and remote sensing, November 2001,vol. 67, no. 11

[5] http://www.motorvista.com/airhist.htm

[6] http://zapport.eecs.berkeley.edu/~boser/publications/hotchips96.pdf

[7] R. T. Howe and R. S. Muller, "Polycrystalline silicon micromechanical beams," in Proc. Electrochemical society Spring Meeting, Montreal, Quebec, Canada, May 9-14, 1982, pp. 184-185.

[8] R. T. Howe and R. S. Muller, "Polycrystalline silicon micromechanical beams," J. Electrochem, Soc., vol. 130, pp. 1420-1423, 1983.

[9] R. T. Howe and R. S. Muller, "Resonant microbridge vapor sensor," IEEE Trans. Electron Devices, vol. ED-33, pp. 499-507, 1986.

[10] Y. -C. Tai and R. S. Muller, "IC processed electrostatic synchronous micromotors," Sensors Actuators, vol. 20, pp. 48-56, 1989.

[11] "ADXL05-monolithic accelerometer with signal conditioning," Analog Devices, Norwood, MA, data sheet, 1995.

[12] M. Lemkin, B. Boser, and J. Smith, "A 3-axis surface micromachined $\Sigma\Delta$ accelerometer," in Tech. Digest Int. Solid State Circuits Conf. (ISSCC'97), San Francisco, CA, Feb. 1997, pp. 202-203.

[13] K. Y. Park, C. W. Lee, Y. S. Oh, and Y. H. Cho, "Laterally oscillated and force-balanced micro vibratory rate gyroscope supported by fish hook shape springs," in Proc. IEEE Micro Electro Mechanical Systems Workshop

(MEMS'97), Japan, 1997, pp. 494-499.

[14] M.S. Kranz and G.K. Fedder, "Micromechanical Vibratory Rate Gyroscopes Fabricated in Conventional CMOS," Proc. Symposium Gyro Technology, Stuttgart, Germany, September 16, 1997, pp.3.0-3.8.

[15] H. Song, Y.S. OH, I.S. Song, S.J. Kang, S.O. Choi, H.C. Kim, B.J Ha, S.S. Baek, C.M.Song, "Wafer Level Vacuum Packaged De-coupled Vertical Gyroscope by a New Fabrication Process," Proc. IEEE Micro Electro Mechanical Systems Workshop (MEMS'00), Japan, 2000, pp. 520-524.

[16] Guohong He, and Khalil Najafi, "A Single Crystal Silicon Vibrating Ring Gyroscope," Proc. IEEE Micro Electro Mechanical Systems Workshop (MEMS'02), Las Vegas, Jan. 20-24, 2002, pp. 718-721.

[17] Hao Luo, Xu Zhu, Hasnain Lakdawala, L. Richard Carley and Gary K. Fedder, "A copper CMOS-MEMS Z-axis gyroscope," Proc. IEEE Micro Electro Mechanical Systems Workshop (MEMS'02), Las Vegas, USA 2002, pp. 631-634.

[18] http://www.europractice.com/technologies/microsystems/products/mc1.html

[19] http://www.analog.com/technology/mems/gyroscopes/index.html

[20] http://www.analog.com/technology/mems/markets/consumer/Joymfsto.html

[21] Chad B. O'Neal, Ajay P. Malshe, Sushila B. Singh, and W.D. Brown, "Challenges in the Packaging of MEMS," 1999 International Symposium on Advanced Packaging Materials, pp. 41-47, 1999

[22] http://207.224.6.57/mdc/mumpso1.htm

[23] Y. Kawazu, H. Kudo, S. Onari, and T. Arai, "Initial Stage of the Interfacial Reaction between Nickel and Hydrogenated Amorphous Silicon," Japanese J. Applied Physics, Vol. 29, No. 4, April 1990.

[24] S.-W. Lee, Y.-C. Jeon, and S.-K. Joo, "Pd Induced Lateral Crystallization of Amorphous Si Thin Films," Applied Physics Lett., Vol. 66, No. 13, March 1995.

[25] Z. Tan, S. M. Heald, M. Rapposch, C. E. Bouldin, and J. C. Woicik, "Gold-Induced Germanium Crystallization," Physical Review B, Vol. 46, No. 15, October 1992.

[26] http://buffy.eecs.berkeley.edu/IRO/Summary/02abstracts/liugang.1.html

[27] H. Baltes, O. Brand, A. Hierlemann, D. Lange and C. Hagleitner, "CMOS MEMS -Present and Future," Proc. IEEE Micro Electro Mechanical Systems Workshop (MEMS'02), Las Vegas, USA 2002, pp. 459-462.

[28] J.H. Smith, S. Montague, J.J. Sniegowski, J. R. Murray, P.J. McWhorter. "Embedded micromechanical devices

for monolithic integration of MEMS with CMOS," IEDM '95 Technical Digest, pp. 609-612, 1995

[29] C. Hierold, "Intelligent CMOS Sensors," Proc. IEEE MEMS2000, Jan. 23-27, 2000, Miyazaki, Japan, pp. 1-6

[30] K. H. -L. Chau, S. R. Lewis, Y. Zhao, R. T. Howe, S. F. Bart, and R. G. Marcheselli, "An integrated force-balance capacitive accelerometer for low-g applications," *Sensors and Actuators A*, vol.54, pp.472-476, 1996.

[31] P.F. van kessel, L.J. Hornbeck, R.E. Meier, M.R. Douglas, "A MEMS-based Projection Display," Proc. IEEE 86 (1998) 1687-1704

[32] G.K.Fedder, S.Santhanam, M.L.Reed, S.C.Eagle, D.F.Guillou, M.S.-C.Lu, and L.R.Carley, "Laminated high-aspect-ratio micro-structures in a conventional CMOS process," Sensors and Actuators, 1996, vol.A57, no. 2, pp. 103-110.

[33] T. Muller, M. Brandl, O. Brand, H. Baltes, "An industrial CMOS process family adapted for the fabrication of smart silicon sensors," Sensors and Actuators A 84 (2000) 126-133.

[34] Huikai Xie, Yingtian Pan, and Gary Fedder, "A SCS CMOS micomirror for optical coherence tomographic imaging," Proc. IEEE MEMS2002, Jan. 20-24, 2002, Las Vegas, USA, pp. 495-498

[35] X.Zhu, D.W.Greve., R.Lawton, N.Presser, and G.K.Fedder, "Factorial Experiment on CMOS-MEMS RIE Post Processing," in *Proc. of the 194th Electrochemical Society Meeting, Symposium on Microstructures and Microfabricated Systems* IV, vol. 98-14, Boston, MA, Nov. 1-6, 1998, pp.33-42.

[36] Michael Lu, Xu Zhu, Gary K. Fedder, "Mechanical Property Measurement Of 0.5-mm CMOS Microstructures," in *MRS 1998 Spring Meeting., Symposium N: Microelectromechanical Structures for Materials Research,* April 13-17, 1998. San Francisco, CA.

[37] G. Zhang, H. Xie, L. E. de Rosset and G.K.Fedder, "A Lateral Capacitive CMOS Accelerometer with Structural Curl Compensation," in *Proc. IEEE Micro Electro Mechanical Systems Workshop* (MEMS'99) Orlando, FL, USA: 17-21 Jan. 1999, pp. 606-611.

[38] H. Lakdawala and G. K. Fedder, "Analysis of Temperature-Dependent Residual Stress Gradients in CMOS Micromachined Structures", The 10th International Conference on Solid State Sensors and Actuators, Sendai Japan, pp 526 -9,June 1999.

[39] H. Luo, G. K. Fedder and L. R. Carley, "An Elastically Gimbaled CMOS-MEMS Gyroscope," in *CD Proc. of the*

Hao Luo

International Symposium on Smart Structure and Microstructure, HongKong, Oct. 19-22, 2000, B1-2, pp.1-6

[40] M.S.-C.Lu, X.Zhu, and G.K.Fedder, "Mechanical Property Measurement of 0.5μm CMOS Microstructures," in *Proc. of the Material Research Society (MRS) 1998 Spring Meeting, Symposium on Microelectromechanical Structures for Materials Research, San Francisco, CA*, Apr. 13-17, 1998.

[41] G. K. Fedder and Q. Jing, "A Hierarchical Circuit-level Design Methodology for Microelectromechanical Systems," IEEE Tran. on Circuits and Systems II: Analog and Digital Signal Processing. Oct. 1999, vol. 46, no. 10. pp. 1309-1315.

[42] C. Kittel, Elementary Statistical Physics. New York: Wiley, 1958.

[43] A. van der Ziel, "Thermal Noise in Field Effect Transistors," Proc. IEEE, August 1962, pp. 1801-12.

[44] Thomas H. Lee, "The Design of CMOS Radio-Frequency Integrated Circuits," Chapter 10, Cambridge University Press

[45] C.T.-C Nguyen and R.T. Howe, "Quality factor control for micromechanical resonators," Technical Digest, IEEE International Electron Devices Meeting, San Francisco, California, December 14-16, 1992, pp. 505-508.

[46] K. K. Hung, P. K. Ko, C. Hu, "A Physics-based MOSFET Noise Model for Circuit," *IEEE Transactions on Electron Devices*, vol. 37, No. 5, May 1990.

[47] David a. Johns, Ken Martin, "Analog integrated circuit design," 1997, by John Wiley & Sons, Inc. Chapter 10.

[48] G.K. Fedder, Ph.D. thesis, "Simulation of Microelectromechanical Systems," EECS, UC Berkeley, 1994.

[49] J. B. Marion and S.T. Thornton, "Classical Dynamics of Particles & Systems," Harcourt Brace Jovanovich, Inc., 1988.

[50] Thomas H. Lee, "The design of CMOS radio-frequency integrated circuits," Cambridge University Press 1998, Chapter 9.

[51] H. Lakdawala, X. Zhu, H. Luo, S. santhanam, L.R. Carley and G.K. Fedder, "Micromachined high-Q inductors in a 0.18 μm copper Interconnect low-K dielectric CMOS process," IEEE Journal of solid-state circuits, vol. 37, NO. 3, March 2002.

[52] R. Groves, K. Stein, d. Harame, and d. Jadus,"Temperature dependence of Q in spiral inductors fabricated in a silicon-germanium/BiCMOS technology," proc. of BCTM, pp. 153-156.

[53] C-M. Hung and Kenneth K. O, "A 1.24-GHz Monolithic CMOS VCO with Phase Noise of -137 dBc/Hz at a 3-

MHz Offset," IEEE Microwave and guided wave letters, vol.9, No.3, pp.111-113March 1999

[54] Jan Craninckx and Michiel Steyaert, "A 1.8GHz Low Phase Noise Spiral LC CMOS VCO," IEEE Symposium on VLSI circuits digest of technical papers, pp.30-31, 1996.

[55] Aleksander Dec, Ken Suyama, "A 1.9GHz Micromachined Based Low Phase Noise CMOS VCO," IEEE International solid-State Circuits Conference, pp.80-82

[56] Chih-Ming Hung, Brian A. Floyd, Namkyu Park and Kenneth K. O, "Fully Integrated 5.35 GHz CMOS VCOs and Prescalers," IEEE Tran. on microwave theory and techniques, vol. 49, No. 1, pp.17-22, January, 2001

[57] Jean Olivier Plouchart, Herschel Ainspan, Mehmet soyuer, and Albert Ruehli, "A Fully Monolithic SiGe Differential Voltage-controlled Oscillator for 5 GHz Wireless Applications," IEEE Radio Frequency Integrated circuits Symposium, pp.57-60, 2000.

[58] http://www-3.ibm.com/chips/micronews/vol5_no4/divergilio.html

[59] K. Oda, E. Ohue, M. Tanabe, H. Shimamoto, T. Onai and K. Washio, Techn. Dig. IEDM 1997, pp. 791-794.

[60] A. Schüppen, U. Erben, a. Gruhle, H. Kibbel, H. Schumacher and U. König, Techn. Dig. IEDM 1995, pp. 743-746.

[61] E. Ohue, K. Oda, R. Hayami and K. Washio, Proc. BCTM 1998, pp.97-100.

[62] D. L. Harame, J. H. Comfort, J. D. Cressler, E. F. Crabbe, Y. C. Sun and B.S. Meyerson, IEEE Trans. Electron Devices vol. 42, 1995, pp. 455-468

Appendix

This appendix gives the reader some background knowledge about motion in a non-inertial reference frame. By going through this appendix reader should understand the principle of vibratory gyroscope. Most of the information comes from the 12th chapter of the book 'Classical Dynamics of Particles & Systems' written by J. B. Marion and S.T. Thornton [49].

At end of this appendix, documentation of some tested chips and process is given.

A. 1 Rotating Coordinate Systems

First, let us consider two sets of coordinate frames, one is 'fixed' or inertial frame designated by '$x^* y^* z^*$', the other one is rotating frame designated by '$x\ y\ z$'. If we choose some point in the space P and assign two radius vectors r^* and r to the two frames, respectively (Figure A-1), we clearly have

$$r^* = R + r \qquad \text{(E A-1)}$$

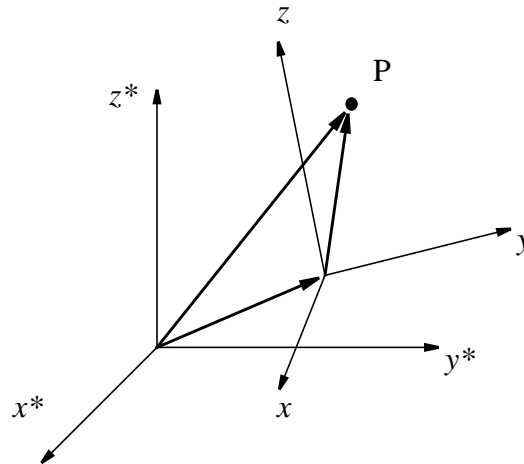where r* is the radius vector of P in the fixed frame and r is the radius vector of P in the rotating frame.

Figure A-1. Two frames and the radius vectors.

If the rotating frame undergoes an infinitesimal rotation $d\theta$, corresponding to some arbitrary infinitesimal displacement, the motion of P in the rotating frame may be described as

$$(dr)_{fixed} = d\theta \times r \qquad \text{(E A-2)}$$

where the designation "fixed" means that the displacement dr is measured in the fixed, or inertial frame. Dividing this equation by the time dt, we obtain the rate of the change of r as measured in the fixed frame.

$$\left(\frac{dr}{dt}\right)_{fixed} = \frac{d\theta}{dt} \times r = \omega \times r \qquad \text{(E A-3)}$$

where ω is the angular velocity of the rotation.

If we consider the velocity $(\frac{dr}{dt})_{rotating}$ of P with respect to the rotating frame, this velocity must be added to the Equation 4-3 to obtain the time rate of change of r in the fixed system.

$$\left(\frac{dr}{dt}\right)_{fixed} = \left(\frac{dr}{dt}\right)_{rotating} + \omega \times r \qquad \text{(E A-4)}$$

Actually there is no limitation on the validity of the Eq. A-4 to be applied to an arbitrary vector.

If we also consider the velocity $(\frac{dR}{dt})_{fixed}$ of the rotating frame with respect to the fixed frame, we may obtain the expression of the velocity of the point P as measured in the fixed coordinate frame.

$$\left(\frac{dr^*}{dt}\right)_{fixed} = \left(\frac{dR}{dt}\right)_{fixed} + \left(\frac{dr}{dt}\right)_{rotating} + \omega \times r \qquad \text{(E A-5)}$$

If we define

$$v_f = \dot{r}_f = \left(\frac{dr^*}{dt}\right)_{fixed} \qquad \text{(E A-6)}$$

Hao Luo

$$V = \dot{R}_f = \left(\frac{dR}{dt}\right)_{fixed} \tag{E A-7}$$

$$v_r = \dot{r}_r = \left(\frac{dr}{dt}\right)_{rotating} \tag{E A-8}$$

we may have

$$v_f = V + v_r + \omega \times r \tag{E A-9}$$

where

v_f = velocity relative to the fixed frame

V = linear velocity of the moving origin of the rotating frame

v_r =velocity relative to the rotating frame

ω =angular velocity of the rotating frame

$\omega \times r$ = velocity due to the rotation of the moving frame

A. 2 The Coriolis Force

Newton's equation $F=ma$ is valid only in an inertial frame of reference. The force on a particle can be obtained by

$$F = ma = m\left(\frac{dv_f}{dt}\right)_{fixed} \tag{E A-10}$$

where the differentiation must be carried out with respect to the fixed frame. Here we only consider the case of constant angular velocity situation (so that $\dot{\omega}=0$). By taking differentiation of the Eq. A-9, we have

$$F = m\ddot{R}_f + m\left(\frac{dv_r}{dt}\right)_{fixed} + m\omega \times \left(\frac{dr}{dt}\right)_{fixed} \tag{E A-11}$$

---

where the $\ddot{R}_f$ is the acceleration of the origin of the rotating frame. The second term can be evaluated by Eq. A-4 (replace the vector r by v_r)

$$\left(\frac{dv_r}{dt}\right)_{fixed} = \left(\frac{dv_r}{dt}\right)_{rotating} + \omega \times v_r$$

$$= a_r + \omega \times v_r$$

(E A-12)

where a_r is the acceleration in the rotating frame.

The last term in Eq. A-11 can be detained directly from Eq. A-4

$$\omega \times \left(\frac{dr}{dt}\right)_{fixed} = \omega \times \left(\frac{dr}{dt}\right)_{rotating} + \omega \times (\omega \times r)$$

$$= \omega \times v_r + \omega \times (\omega \times r)$$

(E A-13)

Combining Eq. A-11 - Eq. A-13, we obtain

$$F = ma_f = m\ddot{R}_f + ma_r + m\omega \times (\omega \times r) + 2m\omega \times v_r$$

(E A-14)

For an observer in the rotating frame, the effective force on the particle is given by

$$F_{eff} = ma_r = ma_f - m\ddot{R}_f - m\omega \times (\omega \times r) - 2m\omega \times v_r$$

(E A-15)

The first two quantities are the usual terms from Newton's equation. The quantity $-m\omega \times (\omega \times r)$ is the usual centrifugal force term which reduces to $-m\omega^2 r$ for the case that ω is normal to the radius vector (Figure A-2).

The last quantity in Eq. A-15 is the Coriolis force term. It arises from the motion of the particle and varnishes if there is no motion. Note that the Coriolis force is a 'virtual' force, which means that there is no such a real force applied on the particle. The reason for this force to show
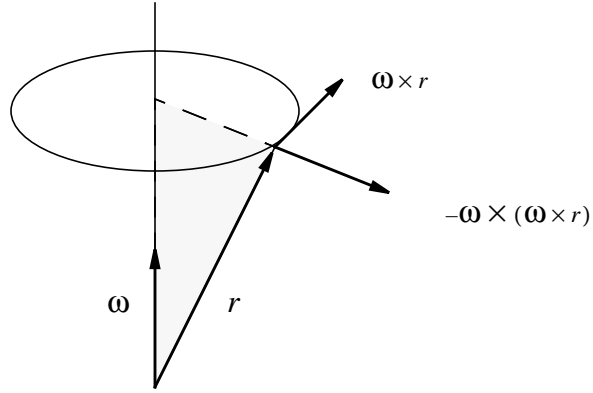
Hao Luo

Figure A-2. Vectors of rotation

up in the equation is because the observer is measuring the force in a non-inertial system -- the rotating frame.

A. 3 Coriolis force and Gyroscope

Eq. A-15 can be applied to the gyroscope design. For a gyroscope design, it is not a great limitation for $a_f = 0$ -- no interference from the outside while measuring the rotation. Although the centrifugal force term includes the information of rotation, in many cases the rotation radius is not known. And usually an output which is proportional to the angular velocity is preferred, thus the Coriolis force is a perfect candidate. But there are other quantities mixed with the Coriolis force and need to be removed from the output.

- $m\ddot{R}_f$ -- the acceleration of the gyroscope frame
  In many cases, the gyroscope may experience this acceleration, such as a moving automobile and flying missile. It can be canceled by a reference accelerometer which is bundled with the gyroscope. Another way to cancel this acceleration is using modulation technique which will be discussed later.

- $m\omega \times (\omega \times r)$ -- the centrifugal force

If the gyroscope is not located at the rotation center, it will experience the centrifugal force. As mentioned before, when the rotation radius is unknown, it would be impossible to recover the rotation speed. Thus it need to be canceled either by reference accelerometer of modulation technique. It is theoretically correct to use two identical accelerometers at different locations to detect the rotation by measuring the difference of centrifugal acceleration. But the sensitivity is proportional to the distance between the two accelerometers which is greatly constrained by the chip size.

- $2m\omega \times v_r$ -- the Coriolis force

  This force is directly proportional to the product of ω and v_r. To get the information of angular velocity, a velocity must be introduced to the particle -- the gyroscope proof mass. Due to the physical dimension limitation, the proof mass can not have a constant velocity -- it would move far away from the frame. Thus a vibration motion can be applied to the proof mass and the gyroscope is called vibratory gyroscope. This vibration velocity ($v_r \ sin(wt)$) will modulate the Coriolis force term. By demodulating this term we may obtain the angular velocity ω. And since the other two terms, acceleration and centrifugal force, are not modulated by the vibration, they will not show up in the final output.
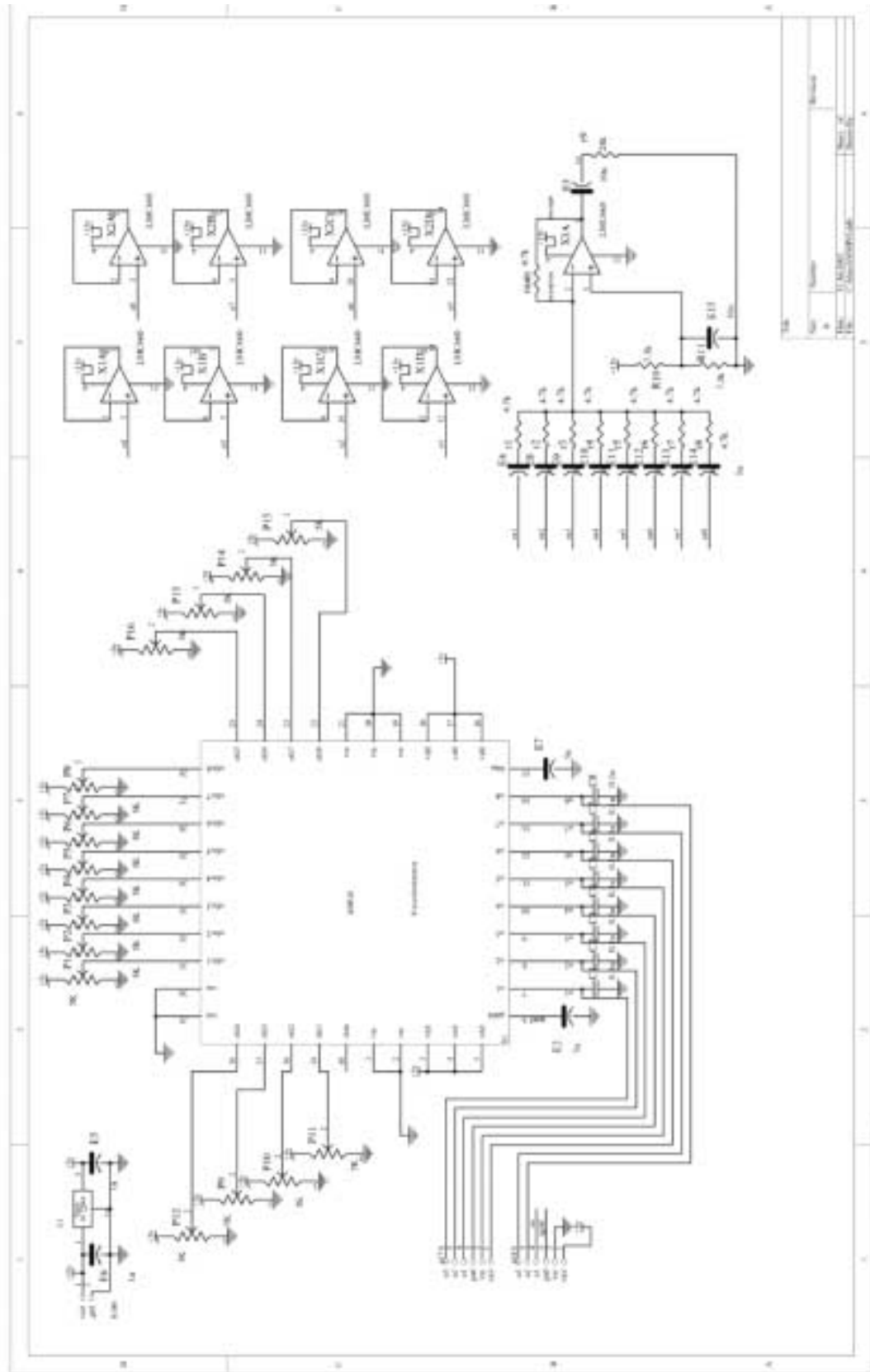
Hao Luo

A. 4 8 accelerometers documents

A-4-1 Bonding diagram

A-4-2 PCB schematic

A-4-3 Package note

Hao Luo
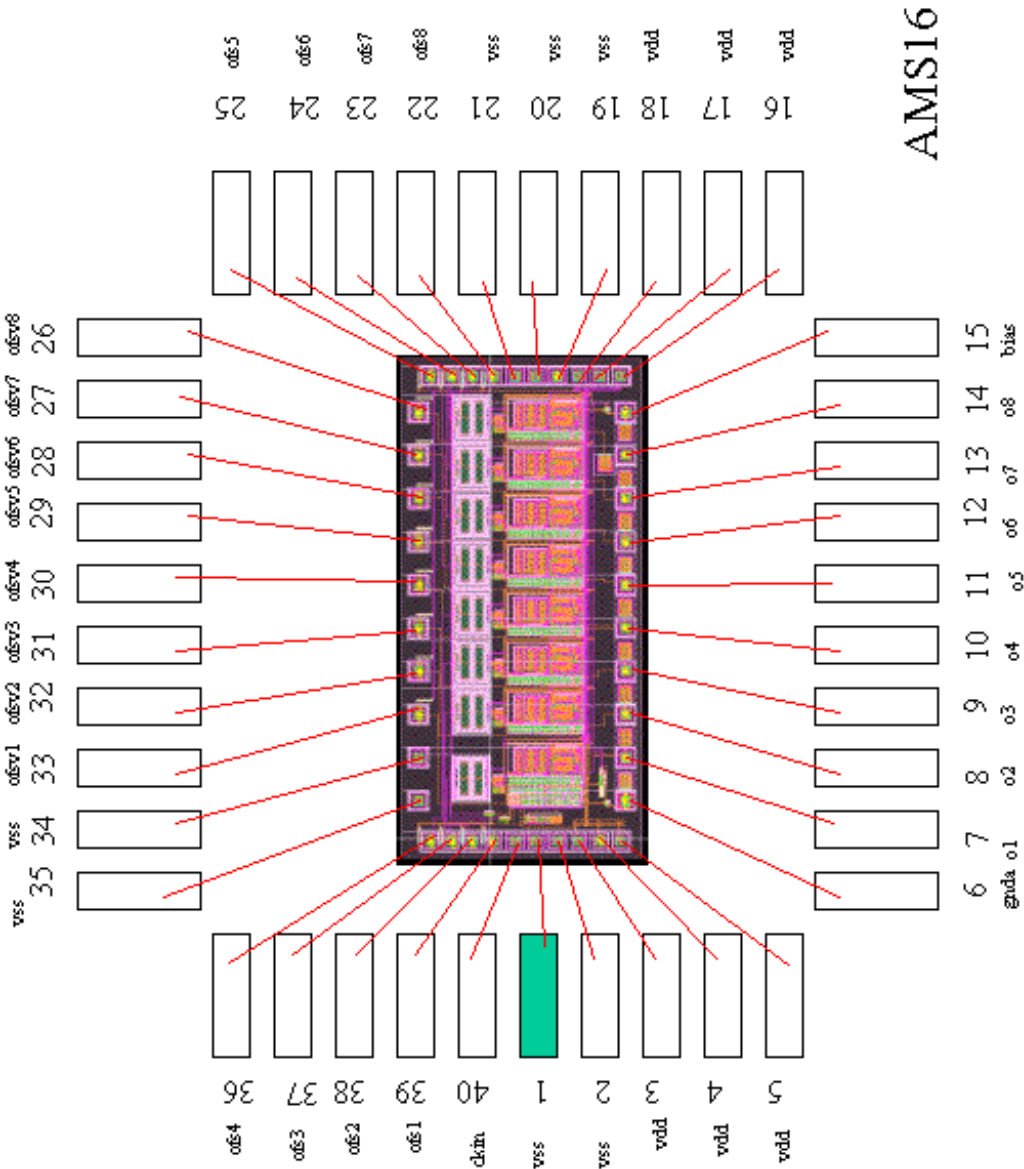
Table 1: hh_ams16 pin connections

PIN #	note	PIN #	note
1 vss	power supply negative 0v	21 vss	power supply negative 0v
2 vss	power supply negative 0v	22 ofs8	accelerometer 8 offset adjust
3 vdd	power supply positive 5v	23 ofs7	accelerometer 7 offset adjust
4 vdd	power supply positive 5v	24 ofs6	accelerometer 6 offset adjust
5 vdd	power supply positive 5v	25 ofs5	accelerometer 5 offset adjust
6 gnda	analog ground 2.5v	26 ofsv8	accelerometer 8 circuit offset adjust
7 o1	accelerometer 1 output	27 ofsv7	accelerometer 7 circuit offset adjust
8 o2	accelerometer 2 output	28 ofsv6	accelerometer 6 circuit offset adjust
9 o3	accelerometer 3 output	29 ofsv5	accelerometer 5 circuit offset adjust
10 o4	accelerometer 4 output	30 ofsv4	accelerometer 4 circuit offset adjust
11 o5	accelerometer 5 output	31 ofsv3	accelerometer 3 circuit offset adjust
12 o6	accelerometer 6 output	32 ofsv2	accelerometer 2 circuit offset adjust
13 o7	accelerometer 7 output	33 ofsv1	accelerometer 1 circuit offset adjust
14 o8	accelerometer 8 output	34 vss	power supply negative 0v
15 bias	internal circuit bias 1.1v	35 vss	power supply negative 0v
16 vdd	power supply positive 5v	36 ofs4	accelerometer 4 offset adjust
17 vdd	power supply positive 5v	37 ofs3	accelerometer 3 offset adjust
18 vdd	power supply positive 5v	38 ofs2	accelerometer 2 offset adjust
19 vss	power supply negative 0v	39 ofs1	accelerometer 1 offset adjust
20 vss	power supply negative 0v	40 ck	inner clock generator output

Hao Luo

A. 5 3DOF documents

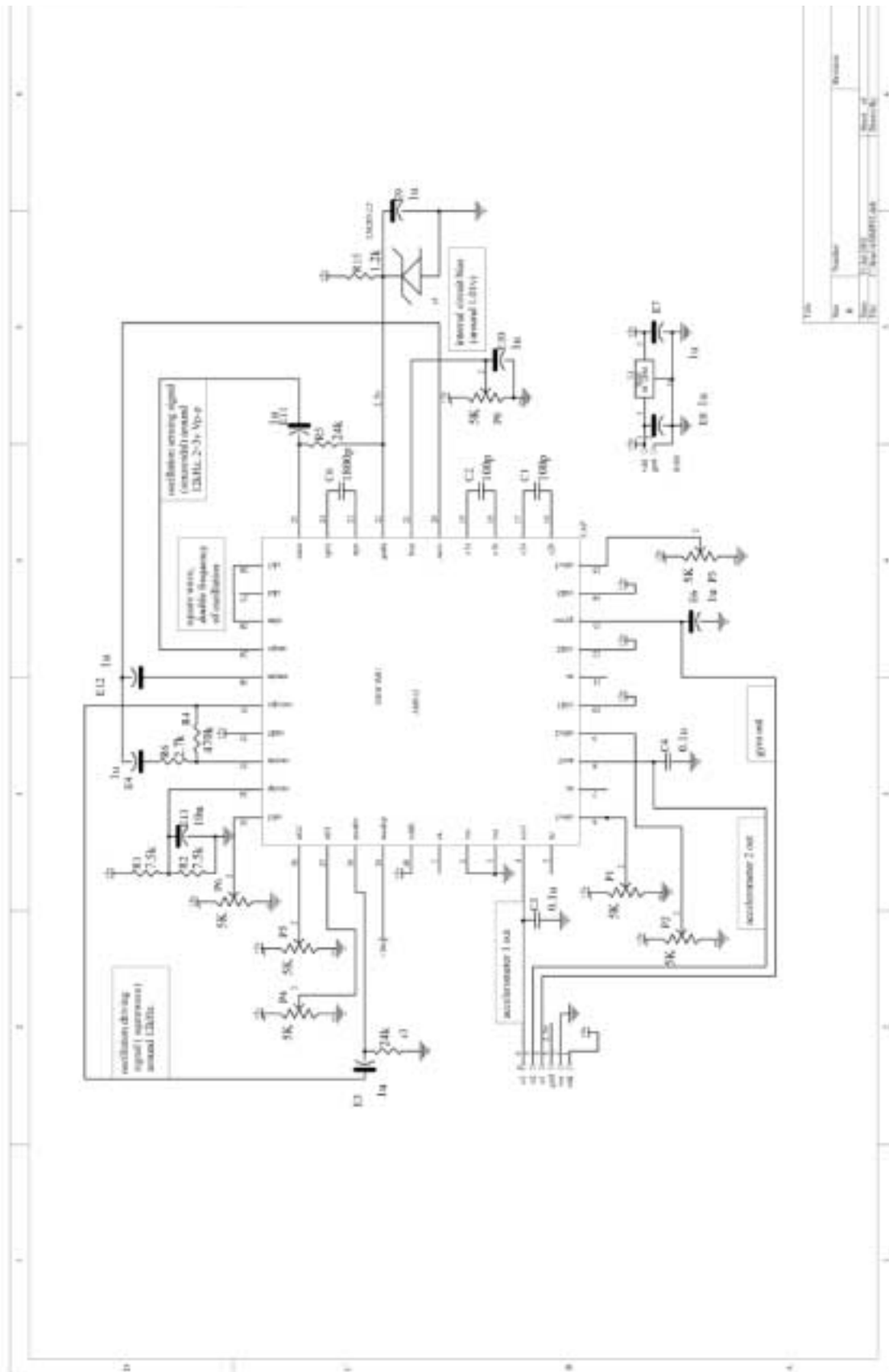### A-5-1 Chip layout

directory: ~/asimps3/hh_AMS12

A-5-2 Bonding diagram

A-5-3 PCB schematic

A-5-4 Package pin note

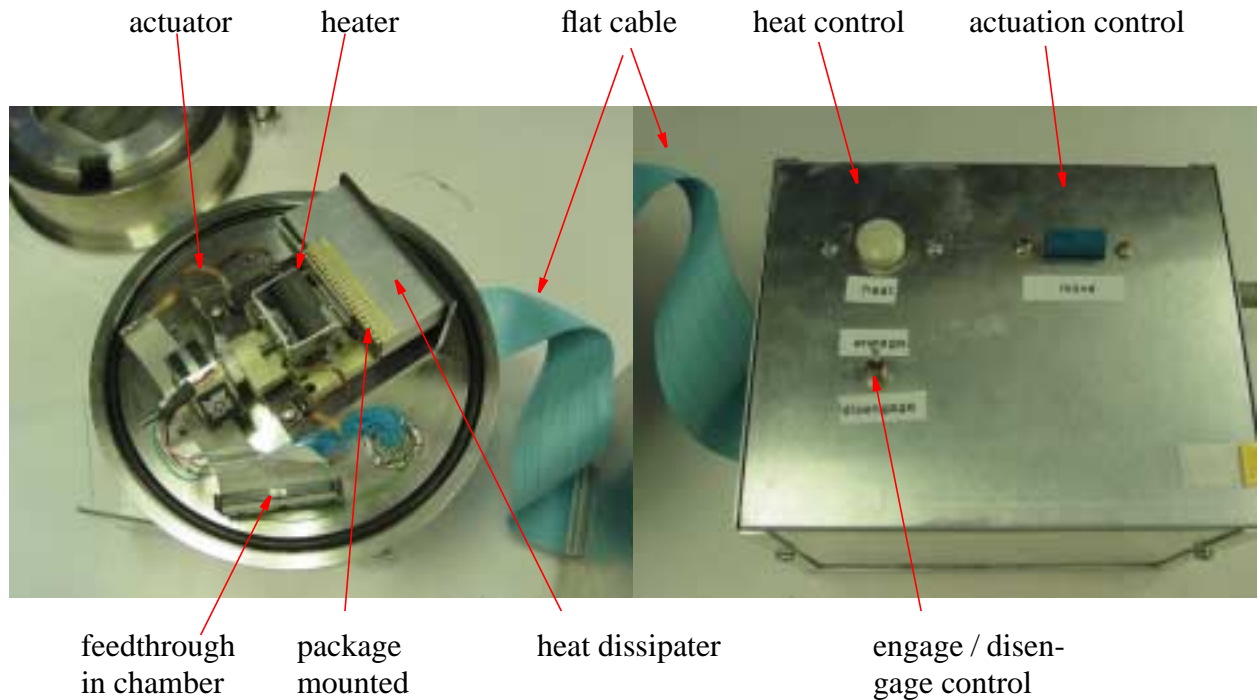12dB oscillation signal amplifier

clock generator gyro oscillation driver frequency doubler

X accelerometer Y accelerometer Gyroscope bias block

digital master controller X accelerometer read out circuit Gyroscope read out circuit

Y accelerometer read out circuit

Hao Luo
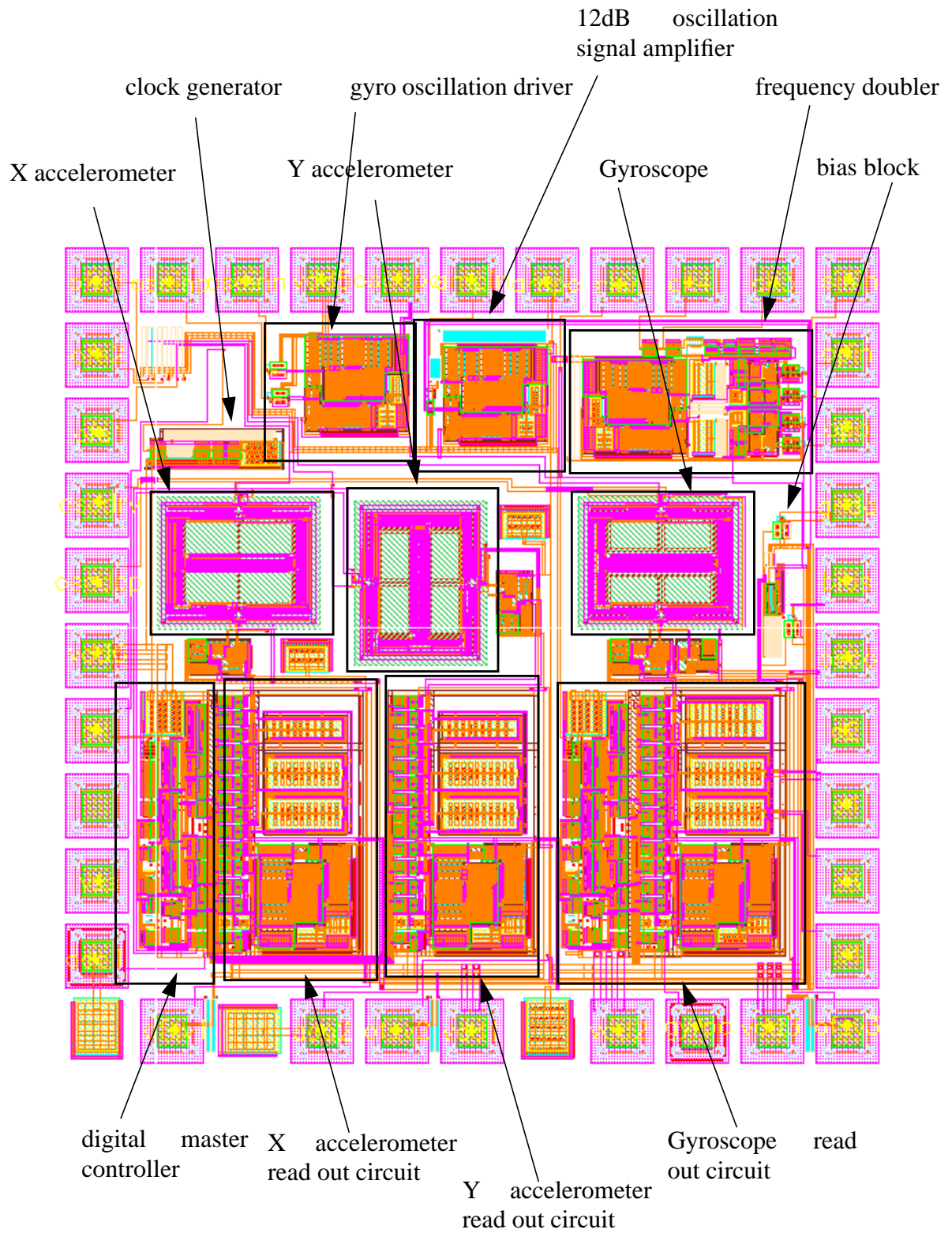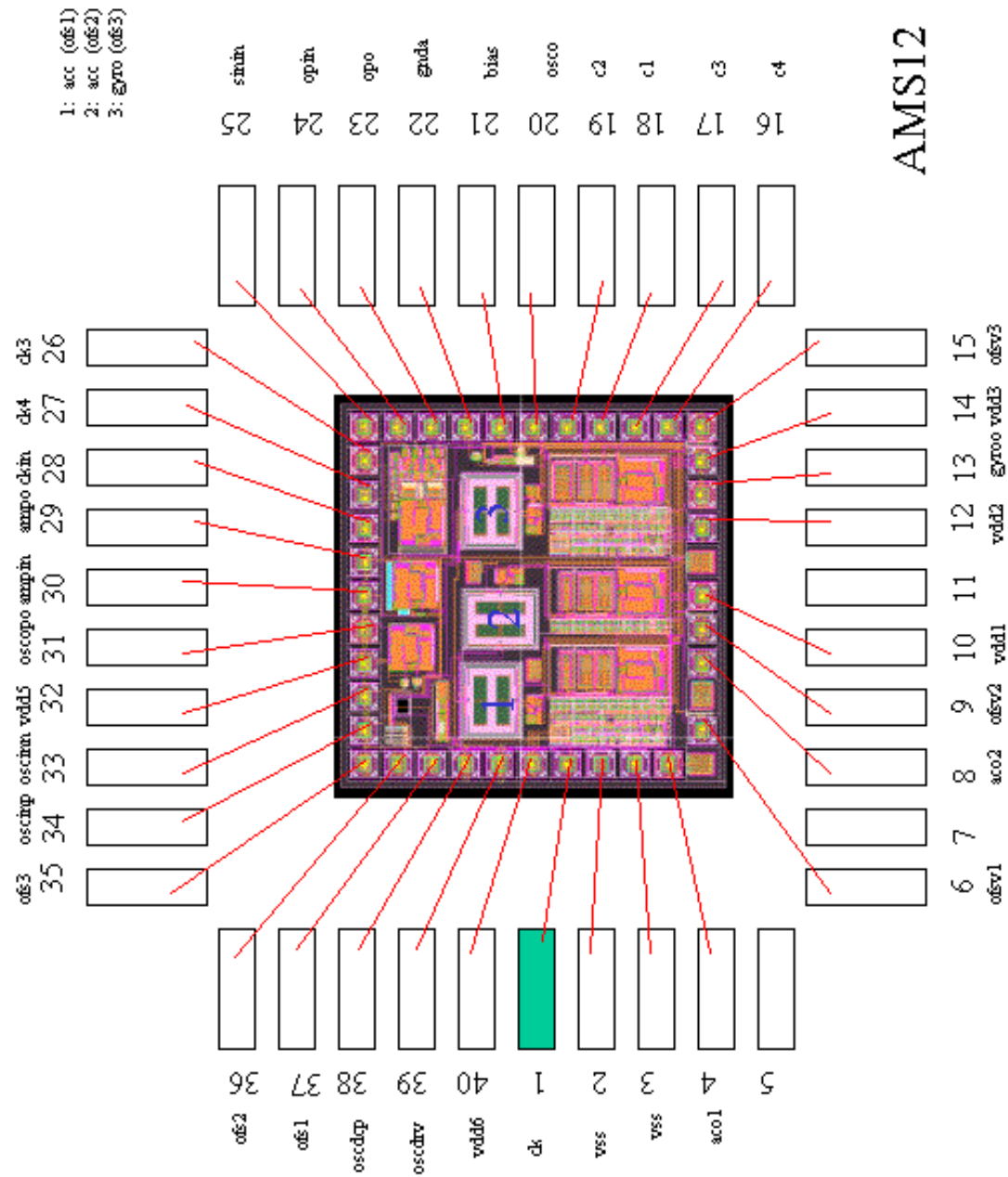
Table 2: hh_ams12 pin connections

PIN #	note	PIN #	note
1 ck	inner clock generator output	21 bias	inner circuit bias, about 1.1v
2 vss	power supply negative 0v	22 gnda	analog ground, 2.5v reference
3 vss	power supply negative 0v	23 opo	1800p capacitor, shift phase 90 degree in freq. doubler
4 aco1	accelerometer 1 output	24 opin	
5 nc	no bonding pad	25 sinin	freq. doubler sinusoidal input
6 ofsv1	accelerometer 1 circuit offset adjust	26 ck3	doubled frequency output (square-wave)
7 nc	no bonding pad	27 ck4	doubled frequency (inversed phase)
8 aco2	accelerometer 2 output	28 ckin	switched capacitor mixer clock in
9 ofsv2	accelerometer 2 circuit offset adjust	29 ampo	13 dB amplifier output
10 vdd1	power supply positive 5v	30 ampin	13 dB amplifier input, amplifies oscillation signal
11 nc	no bonding pad	31 oscopo	gyroscope oscillation driver op-amp output
12 vdd2	power supply positive 5v	32 vdd5	power supply positive 5v
13 gyroo	gyroscope output	33 oscinn	gyroscope oscillation driver op-amp negative input
14 vdd3	power supply positive 5v	34 oscinp	gyroscope oscillation driver op-amp positive input
15 ofsv3	gyroscope circuit offset adjust	35 ofs3	gyroscope offset adjust
16 c2b	switched capacitor--integration capacitor	36 ofs2	accelerometer 1 offset adjust
17 c2a		37 ofs1	accelerometer 2 offset adjust
18 c1b	switched capacitor--sampling capacitor	38 oscdrv	gyroscope oscillation drive terminal
19 c1a		39 oscdcp	gyroscope oscillation bias (high positive voltage)
20 osco	gyro oscillation sensing output	40 vdd6	power supply positive 5v

A. 6 Vacuum sealing process

The vacuum sealer includes sealing machine and controller. They are connected with flat cable through the vacuum chamber feedthrough.

actuator   heater   flat cable   heat control   actuation control

feedthrough   package   heat dissipater   engage / disen-
in chamber   mounted   gage control

The basic procedure is -- pump out air --> heat the heater --> engage the heater --> wait for solder melting --> disengage the heater --> cool down while keep pumping. The steps are shown below:

step 1: Prepare package.
Choose a clean cap, melt small amount of solder on the cap edge and the seal ring of the package.
Align and solder the cap onto the package but leave a gap so that the air inside can be pumped out freely.

step 2: Prepare sealing machine.
Connect the sealing machine and the controller.
Put the sealing machine into the vacuum chamber.

step 3: Insert the package.
Put the package under the spring clip and make a good thermal contact against the big aluminum heat dissipator.
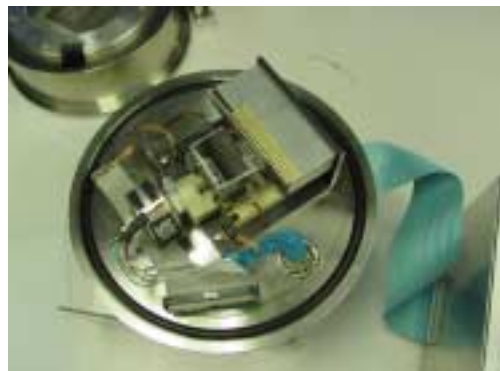
step 4: Disengage the heater.
Put the 'engage/disengage' button to 'disengage' position and then press the 'move' button to disengage the heater.

step 5: Pumping air and heat the heater
Pump out the air to the desired pressure and then press the 'Heat' button to raise the heater temperature. A LED will indicate the heating 'On'
The chamber pressure may raise a little bit, keep pumping while heating.
Wait about 2 minutes and observe from the glass window that the solder starts melting.
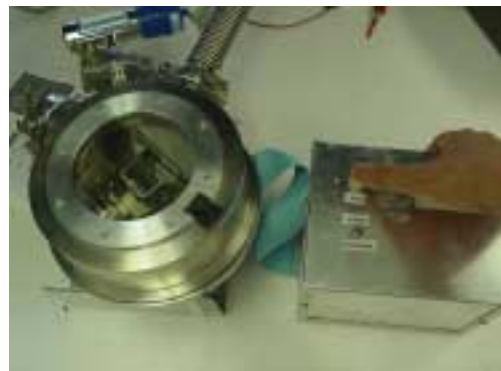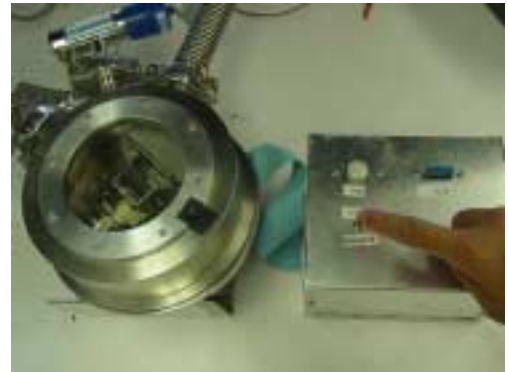
step 6: Engage the heater
Put the 'engage/disengage' button to 'engage' position and press the 'move' button to engage the heater.
Let the heater press on the spring clip to heat the package cap until the solder melts. The melting process can be observed from the glass window.
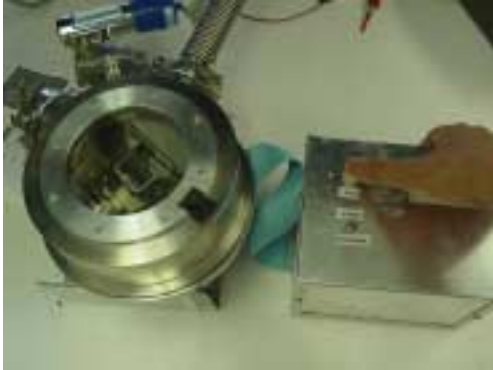
step 7: Stop heating and disengage the heater.
Press the 'Heat' button again to stop the heating. Then disengage the heater.

step 8: Cool down while keep pumping. Keep pumping and wait for about 30 minutes till the package cools down.
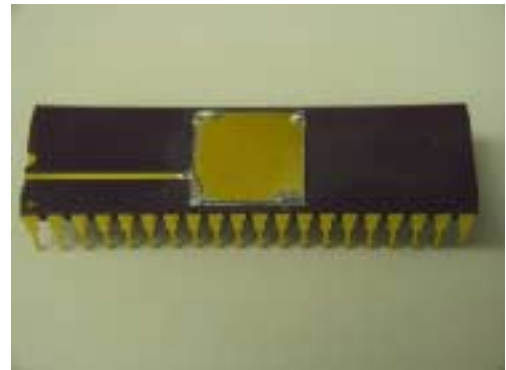
A. 7 Submitted chips numbering and results

Table 3: Fabricated IMU chip numbering, function and test results

Chip # & file locations	Layout	Result
actuators52a /afs/ece.cmu.edu/usr/ mems/.vol10/ cadence_mosis_archive/ cds.lib	HP 0.5 µm process Lateral accelerometer	one good accelerometer, results published in MEMS00
actuators53a ~/cds.lib	HP 0.5 µm process Large lateral accelerometer	severe curling, not usable circuit does not work
actuators55a ~/cds.lib	HP 0.5 µm process Large lateral accelerometer	severe curling, not usable
actuators56a ~/cds.lib	HP 0.5 µm process Lateral accelerometer and vertical gyroscope	accelerometer works, gyro doesn't due to severe curling
actuators59b ~/cds.lib	HP 0.5 µm process Lateral accelerometer and several kind of design of gyroscope	accelerometer works, gyro doesn't due to severe curling
actuators61a ~/cds.lib	HP 0.5 µm process Lateral accelerometer and vertical gyroscope	Both devices work. First gyroscope working. Result Published in Ism3.
hh_AMS2_Sept_00 /afs/ece.cmu.edu/usr/ mems/.vol11/ asimps_cds/cds.lib	AMS 0.6 µm process Vertical gyroscopes with unity-gain buffers. Switched-capacitor demodulator	Low yield due to severe curling. All system circuits proven working.
hao4 ~/cds.lib	AMS 0.6 µm process Lateral accelerometer and vertical gyroscope array of 12	Severe curling. Only lateral accelerometer works

Table 3: Fabricated IMU chip numbering, function and test results

Chip # & file locations	Layout	Result
hh_AMS5 ~/cds.lib	AMS 0.6 μm process Device with 'N selective layer' to reduce curling. Lateral accelerometer with fixed-gain amplifier. Vertical gyroscope with pre-amplifier. Springs are put at the center of device to reduce curling effect. One switched-capacitor demodulator	Both accelerometer and gyroscope works. The fixed-gain amplifier for accelerometer has large offset. Not very successful. The first integrated gyroscope works.
hh_AMS6 ~/cds.lib	AMS 0.6 μm process Large bulk gyroscope	Releasing not successful
hh_AMS7 ~/cds.lib	AMS 0.6 μm process Accelerometer and gyroscope array of 6. Each device has its own fixed-gain amplifier and switched-capacitor demodulator. Fully integrated	Due to large circuit offset not very successful. Only several devices can work on one die.
hh_AMS8 ~/cds.lib	AMS 0.6 μm process Large bulk gyroscope pair	Releasing not successful.
hh_AMS9 ~/cds.lib	AMS 0.6 μm process Similar to hh_AMS5. The difference is in the sensor design. The springs are put at four corners of the device to get simpler layout routing and less parasitic capacitance.	Severe device curling due to the springs' location.
hh_AMS10 ~/cds.lib	AMS 0.6 μm process Surface gyroscope pair	Single device can work. But due to fabrication variation, two devices have different resonant frequencies.
hh_AMS11 ~/cds.lib	AMS 0.6 μm process One fully integrated lateral accelerometer and one fully integrated vertical gyroscope.	Both devices work. But due to the share of bias, only one device can be tuned to work at one time.

Table 3: Fabricated IMU chip numbering, function and test results

Chip # & file locations	Layout	Result
hh_AMS12 ~/cds.lib	AMS 0.6 μm process Fully integrated 3 DOF chip with X-axis accelerometer, Y-axis accelerometer and Z-axis gyroscope	Chip works but yield is low. The best results are: accelerometer 0.5mG/sqrt(Hz), gyroscope 0.3 degree/sec/sqrt(Hz)
hh_AMS13 ~/cds.lib	AMS 0.6 μm process Same sensor design as the hh_AMS12. But the circuit uses P-type sensing amplifier and switches as demodulator.	The P-type sensing amplifier is not successful due to large offset. Chip does not function.
hh_AMS14 ~/cds.lib	AMS 0.6 μm process Same sensor design as the hh_AMS12. But the circuit uses P-type sensing amplifier	The P-type sensing amplifier is not successful. Chip does not function.
hh_AMS15 ~/cds.lib	AMS 0.6 μm process Fully integrated gyroscope pair with coupling beams.	Device not successful. Twist mode triggered instead of the anti-phase driving mode.
hh_AMS16 ~/cds.lib	AMS 0.6 μm process Fully integrated 8 identical accelerometers.	Chip works. Does improve noise performance, but not much (4 dB)
hh_AMS17_circuit ~/cds.lib	AMS 0.6 μm process Test chip with dummy device and each stage circuits to measure the circuit performance	Circuits of each stages are quantitatively calibrated to measure their performance.
hh_AMS18 ~/cds.lib	AMS 0.6 μm process Accelerometer and gyroscope array of 6 using P-type sensing amplifier.	The P-type sensing amplifier is not successful. Chip does not function.

(a)

(b)

(c)

(d)

(e)

(f)
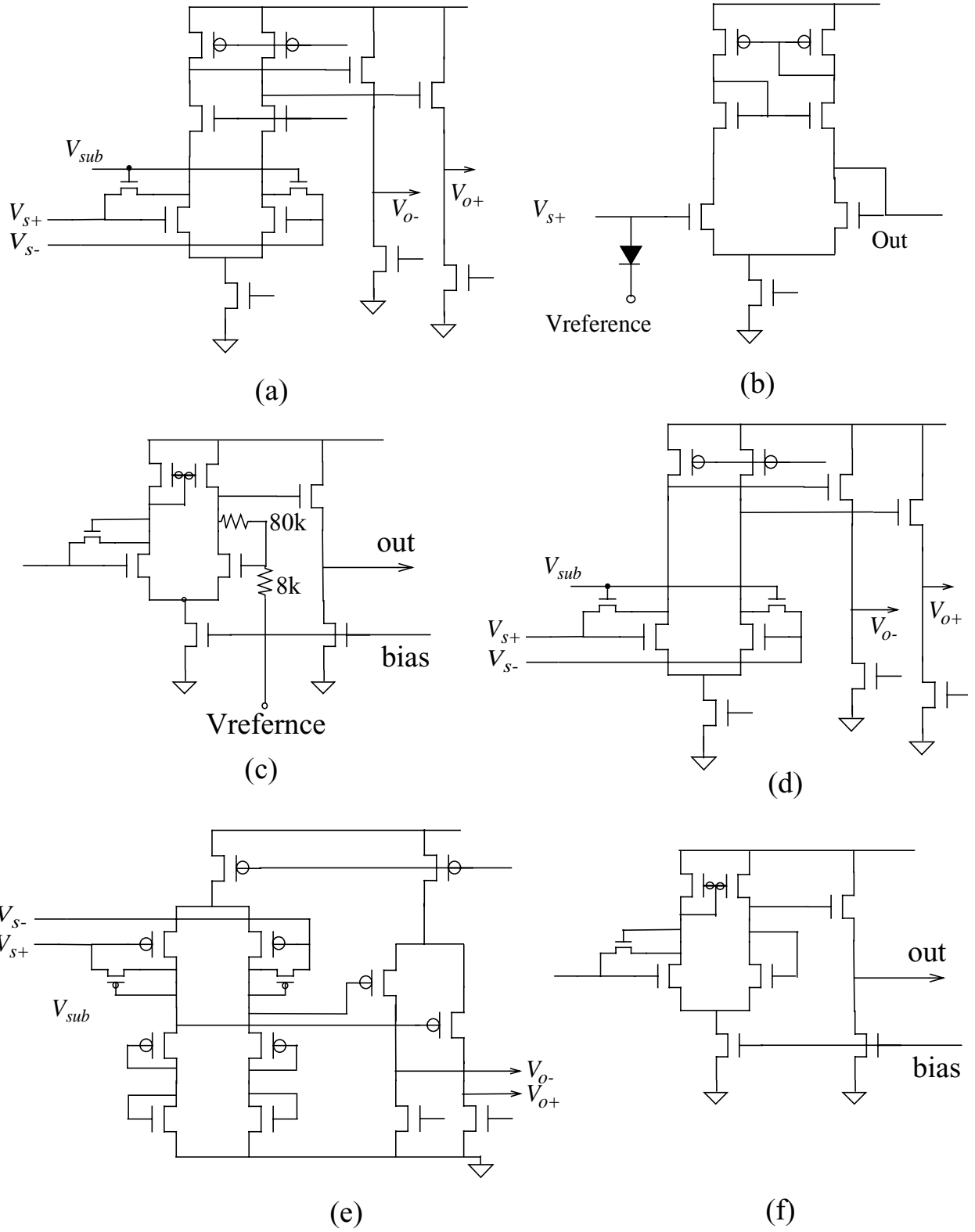
Different circuits used in capacitive sensing.

Hao Luo
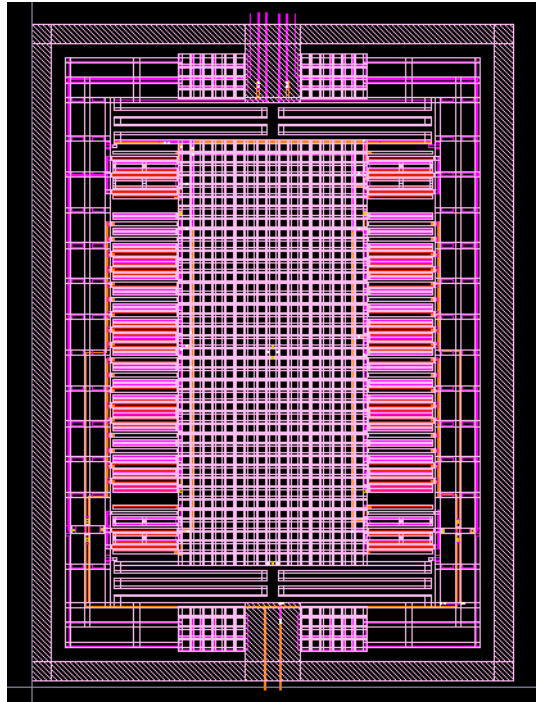
chip number: act52a
size: 510μm by 350μm
sensing finger number: 40
single metal layer (metal3)
spring: 2turn 110μm long, 2.1μm wide
circuit used (a)
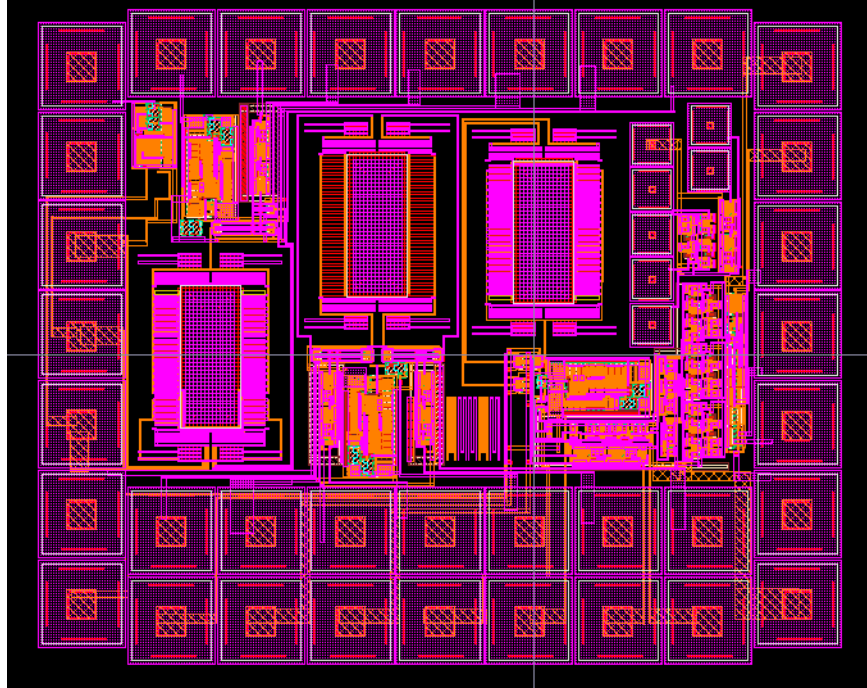
chip number: act53a
size: 510μm by 350μm
sensing finger number: 40
single metal layer (metal3), curling acceptable
spring: 2turn 110μm long, 2.1μm wide
circuit used (b)
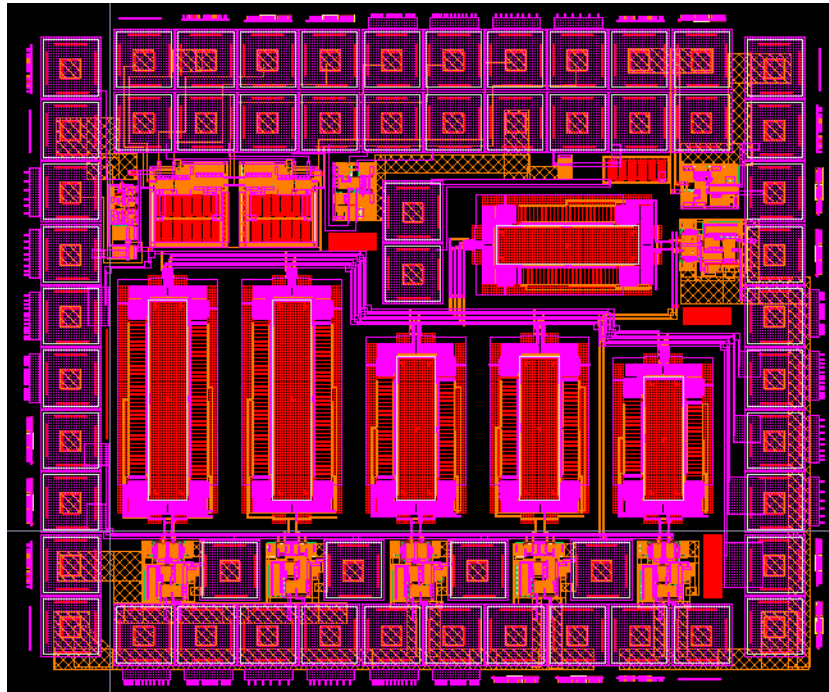
chip number: act52a
size: 800μm by 350μm
sensing finger number: 80
single metal layer (metal3), poor curling
spring: 2turn 110μm long, 2.1μm wide
circuit used (a)
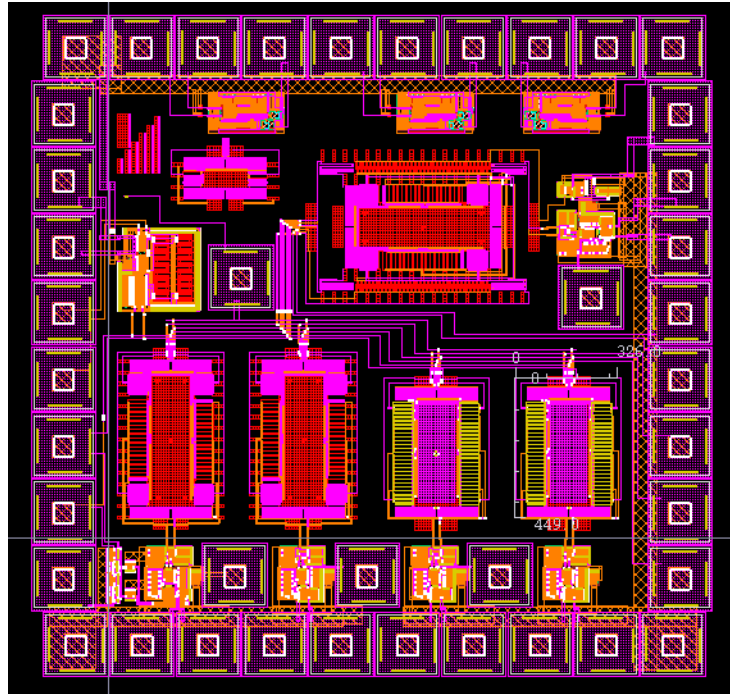
chip number: act56a
gyro size: 700μm by 450μm, act size 450μm by 320μm
sensing finger number: 40
single metal layer (metal3), poor curling
spring: 2turn 110μm long, 2.1μm wide
circuit used (a)

Hao Luo
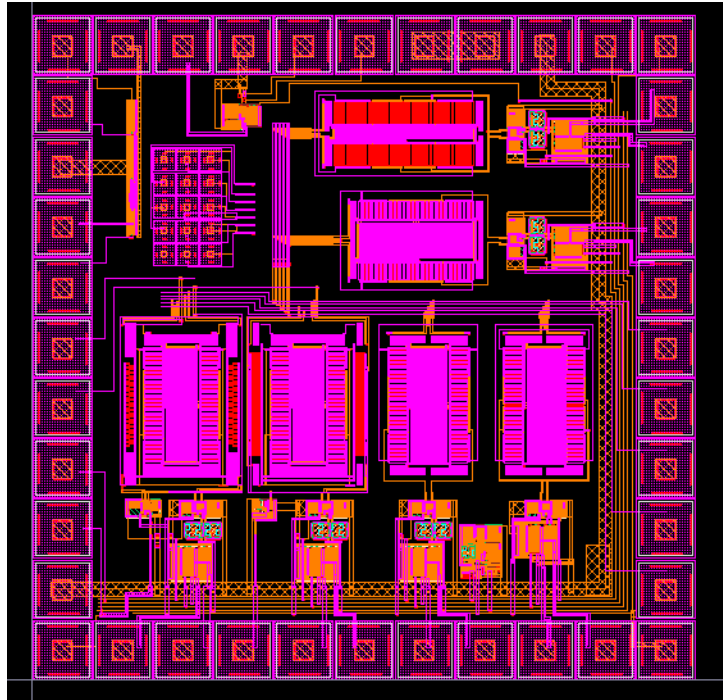
chip number: act59b
gyro size: 600μm by 420μm
sensing finger number: 40
single metal layer (metal3), poor curling
spring: 2turn 110μm long, 2.1μm wide
circuit used (d)
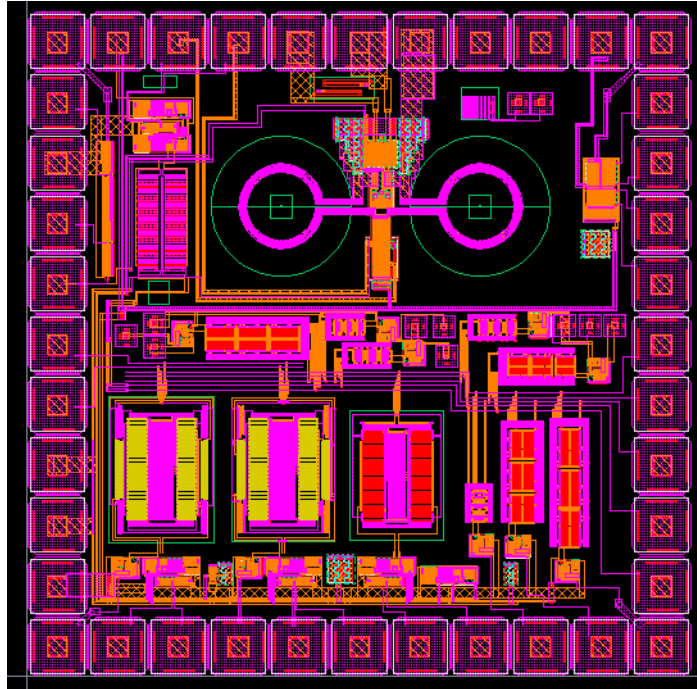
chip number: act61a
gyro size: 500μm by 350μm
sensing finger number: 40
single metal layer (metal3), curling acceptable
spring: 1turn 105μm long, 1.8μm wide
circuit used (a)

Hao Luo
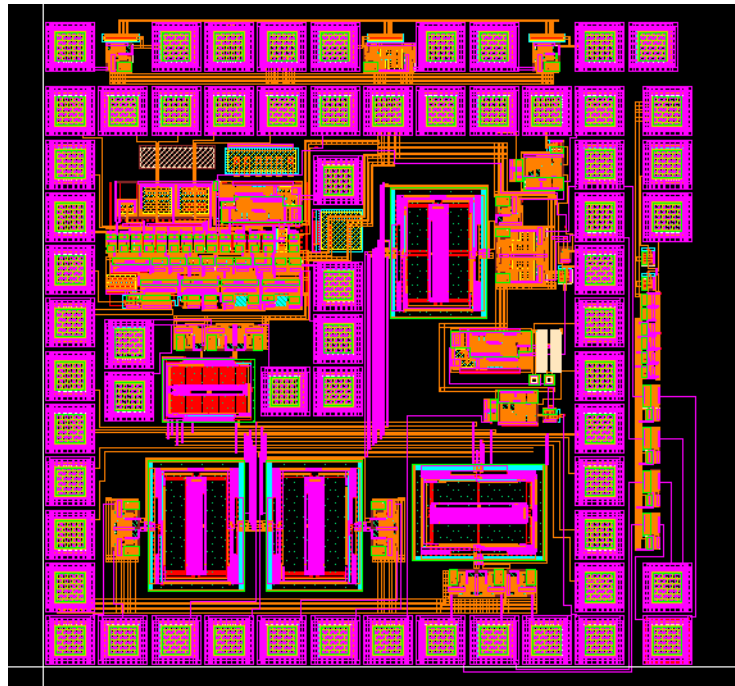
chip number: hh_AMS2_Sept_00
gyro size: 500μm by 350μm
sensing finger number: 40
single metal layer (metal3), poor curling
spring: 1turn 95μm long, 1.8μm wide
circuit used (f)
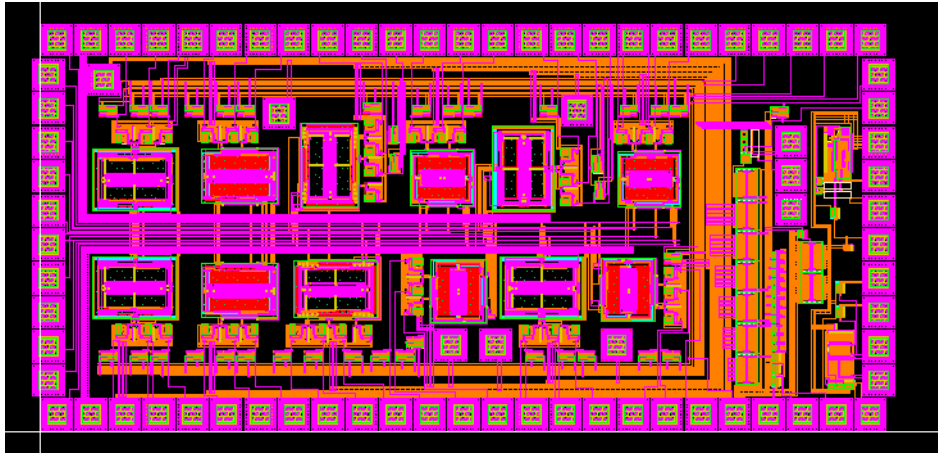
chip number: hao4
gyro size: 500μm by 350μm
sensing finger number: 40
single metal layer (metal3), poor curling
spring: 1turn 95μm long, 1.8μm wide
circuit used (f)
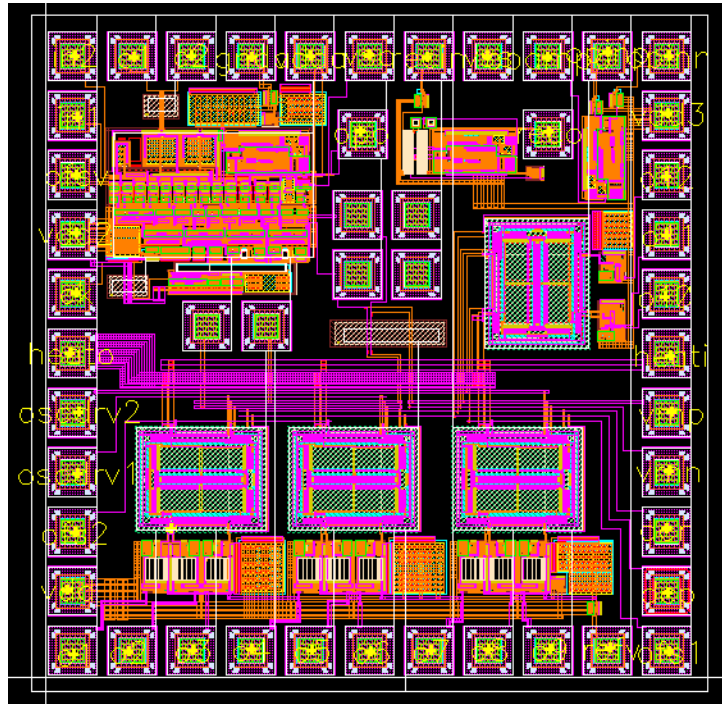
chip number: hh_AMS5
gyro size: 500μm by 350μm
sensing finger number: 40
single metal layer (metal3), N active, curling acceptable
spring: 2turn 65μm long, 1.8μm wide
circuit used (c)
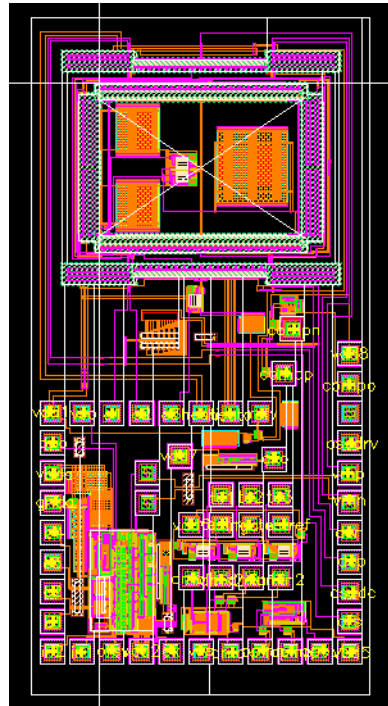
chip number: hh_AMS6
gyro size: 2000μm by 1800μm
sensing finger number: 200
bulk
spring: 2turn 450μm long, 6μm wide
circuit used (f)
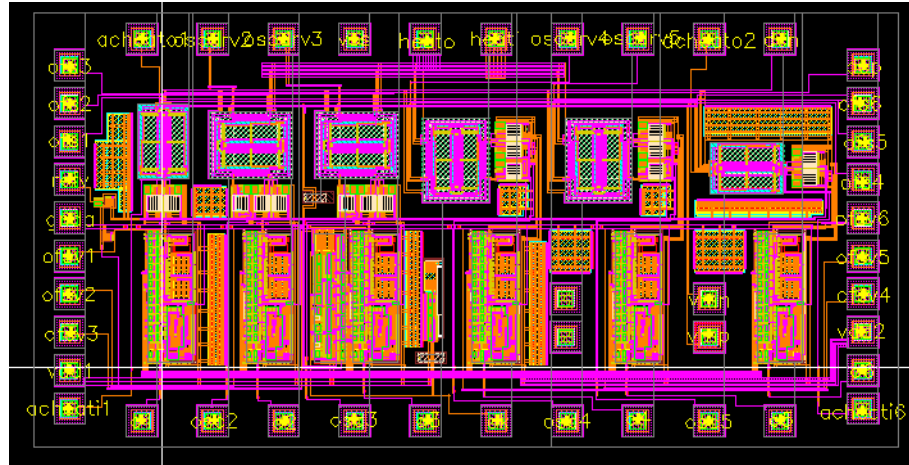
chip number: hh_AMS7
gyro size: 420µm by 350µm
sensing finger number: 40
single metal layer (metal3), N active, curling acceptable
spring: 2turn 65µm long, 1.8µm wide
circuit used (c)
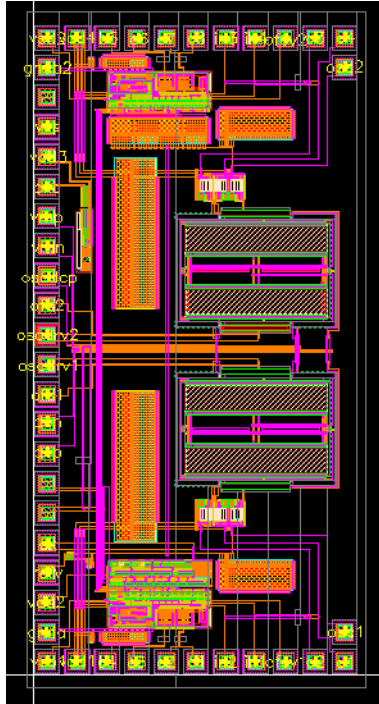
chip number: hh_AMS8
gyro size: 1200μm by 880μm
sensing finger number: 120
bulk
spring: 1turn 300μm long, 6μm wide
circuit used (f)
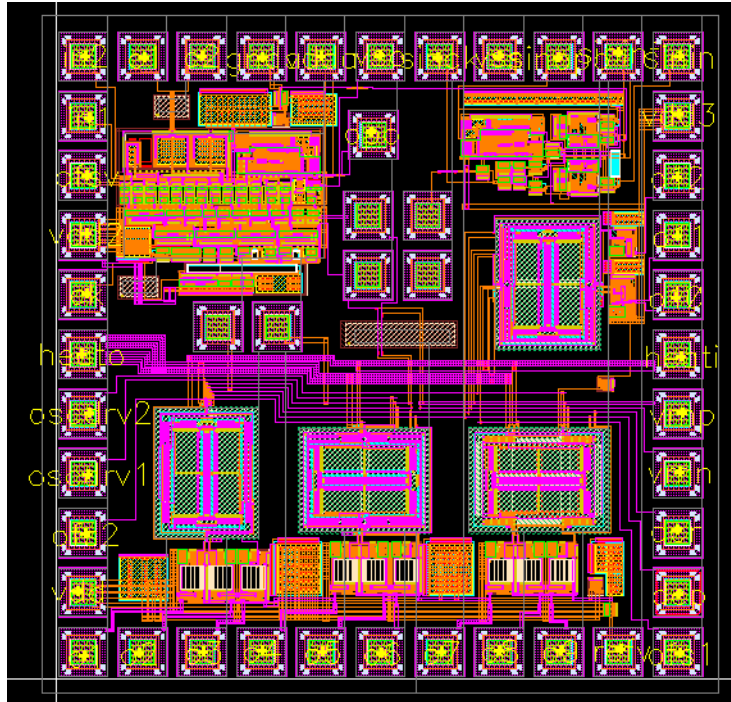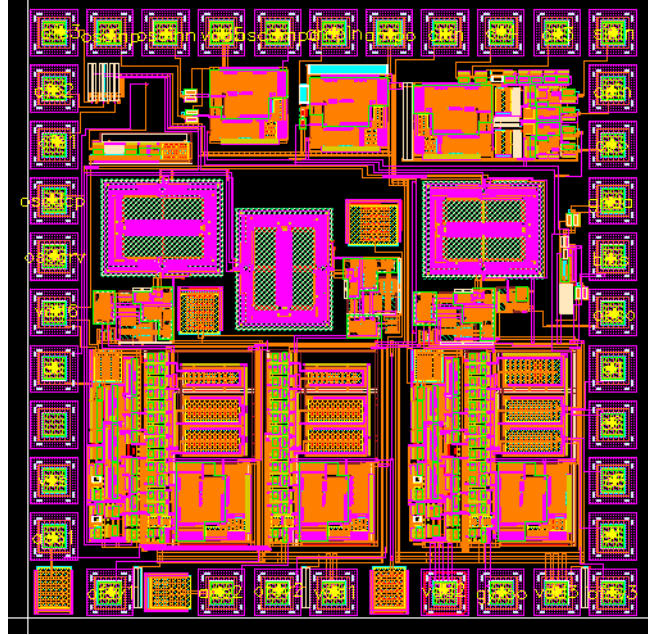
chip number: hh_AMS9
gyro size: 450μm by 350μm
sensing finger number: 40
single metal layer (metal3), N active, curling acceptable
spring: 2turn 75μm long, 1.8μm wide
circuit used (f)
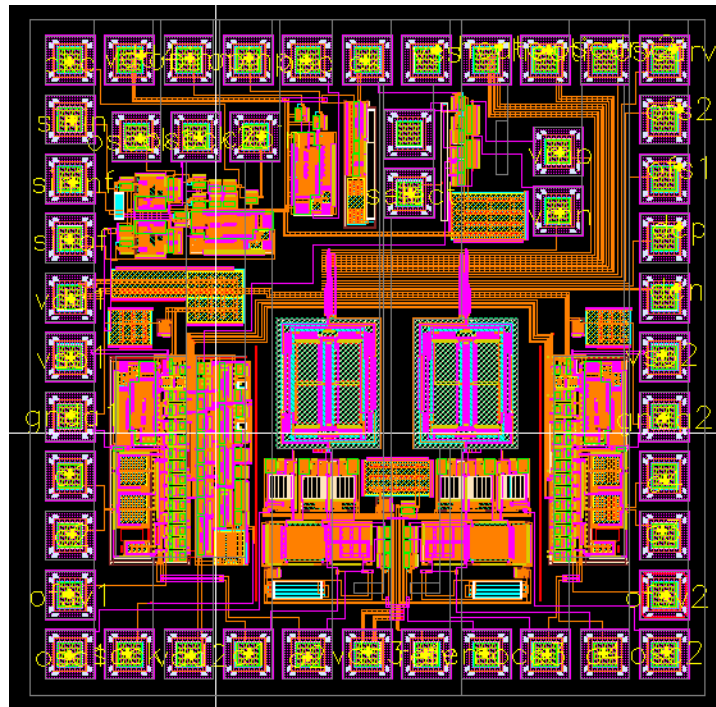
chip number: hh_AMS10
gyro size: 450μm by 350μm
sensing finger number: 40
single metal layer (metal3), N active, curling acceptable
spring: 1turn 75μm long, 1.8μm wide
circuit used (f)
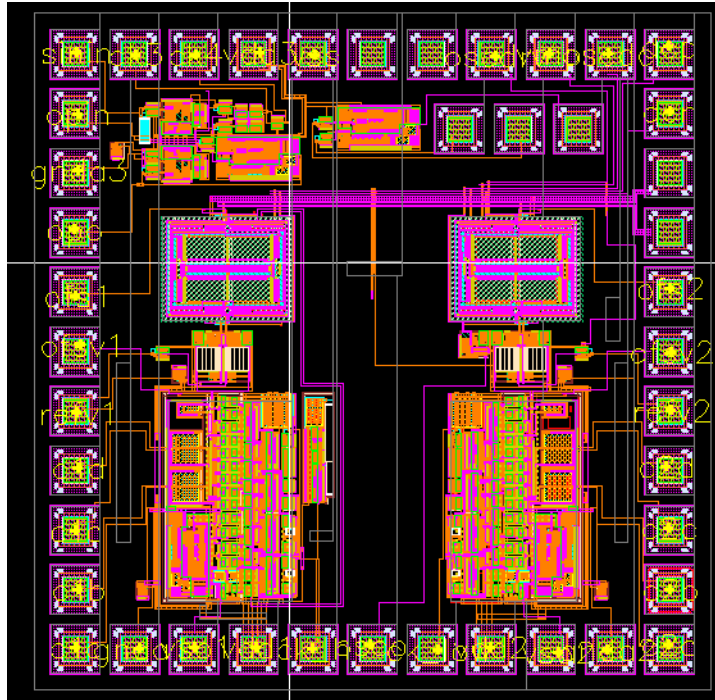
chip number: hh_AMS11
gyro size: 450μm by 350μm
sensing finger number: 40
single metal layer (metal3), N active, curling acceptable
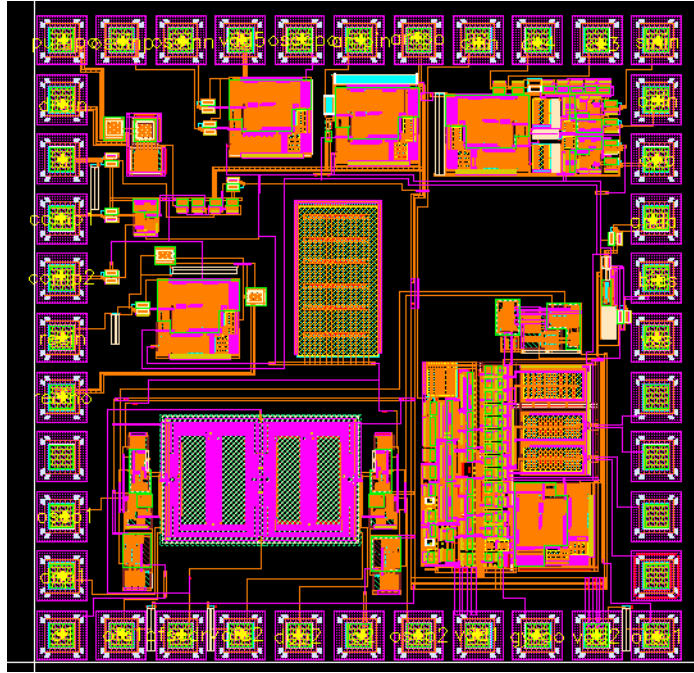spring: 1turn 95μm long, 1.8μm wide
circuit used (f)
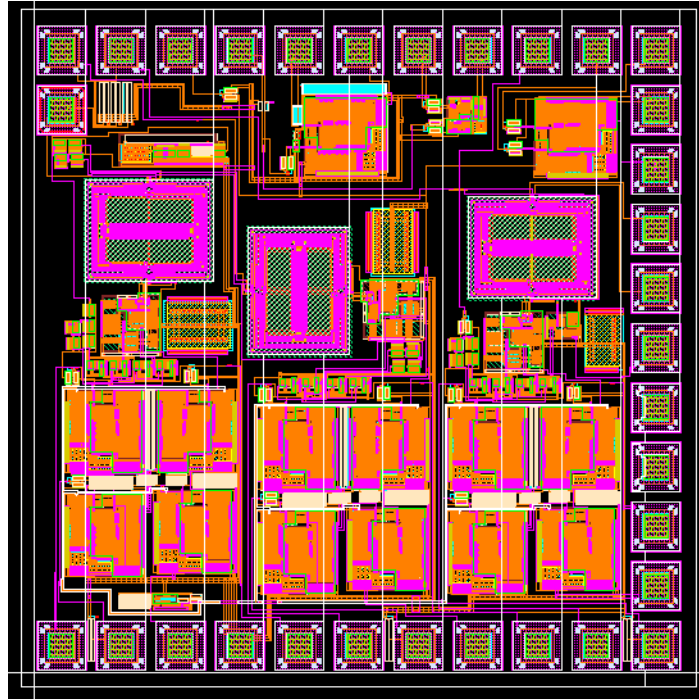
chip number: hh_AMS13
gyro size: 450μm by 350μm
sensing finger number: 40
three metal layer, N active, good flatness
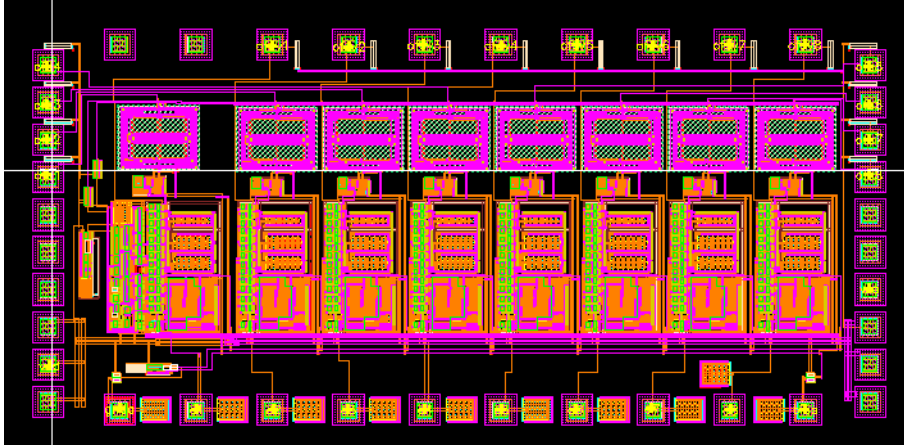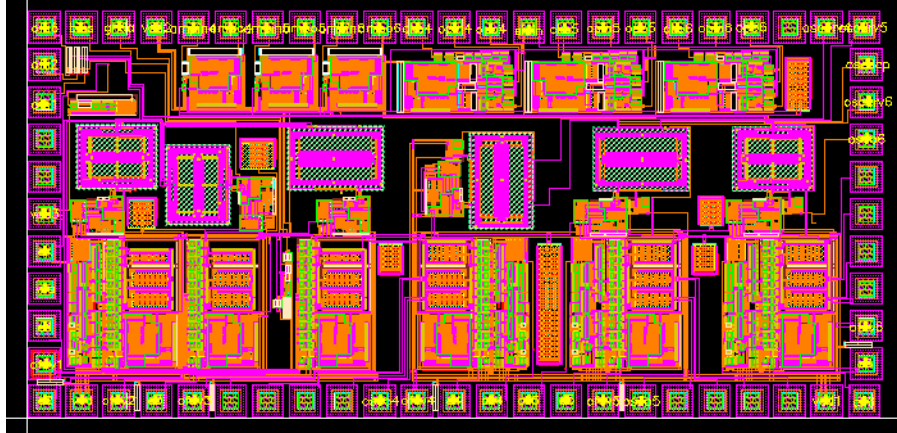spring: 2turn 75μm long, 1.8μm wide
circuit used (e)

Hao Luo

chip number: hh_AMS14
gyro size: 450μm by 350μm
sensing finger number: 40
three metal layer, N active, good flatness
spring: 2turn 75μm long, 1.8μm wide
circuit used (e)

chip number: hh_AMS15
gyro size: 450μm by 350μm
sensing finger number: 40
three metal layer, N active, good flatness
spring: 2turn 75μm long, 1.8μm wide
circuit used (f)

chip number: hh_AMS16
gyro size: 450μm by 350μm
sensing finger number: 40
three metal layer, N active, good flatness
spring: 2turn 75μm long, 1.8μm wide
circuit used (a)

chip number: hh_AMS18
gyro size: 450μm by 350μm
sensing finger number: 40
three metal layer, N active, good flatness
spring: 2turn 75μm long, 1.8μm wide
circuit used (e)